

学位論文

---

# Interplay between Magnetorotational Instability and Magnetic Reconnection in Collisionless Accretion Disks

(無衝突降着円盤に於ける磁気回転不安定性と磁気リコネクションの相互作用)

---

平成 26 年 10 月 博士(理学) 申請

東京大学大学院理学系研究科

地球惑星科学専攻

白川 慶介

© Copyright by  
Keisuke SHIRAKAWA  
October, 2014



THE UNIVERSITY OF TOKYO

*Abstract*

Faculty of Science

Department of Earth and Planetary Science

Doctor of Philosophy

**Interplay between Magnetorotational Instability and Magnetic  
Reconnection in Collisionless Accretion Disks**

by Keisuke SHIRAKAWA

---

Transport of angular momentum is one of the essential problems in accretion disk physics since rotating matters must lose angular momentum when they “accrete” into the central star. For the efficient transport of angular momentum, a strong viscosity provided by turbulence in the disk is considered to be important. Magnetorotational instability (MRI), which is a main topic of this dissertation, is believed to drive a strong turbulence in the disk and has been studied by numerical simulations for several decades. To estimate the efficiency of the angular momentum transport, evaluation of the saturated state of MRI-driven turbulence is required. Since MRI provides strong dynamo process and enhances magnetic field, dissipation process is also important for the saturation of MRI-driven turbulence. Magnetic reconnection, which is another topic of this dissertation is considered to be a promising agent for the dissipation in disk turbulence.

Until now studies of disk turbulence has been carried out under MHD approximation which mainly assumes that the disk is constituted with “collisional” plasma. However, recent observations of Sgr A\* which lies in the center of our galaxy, suggest that this assumption is not necessarily valid. This object is considered to be constituted with supermassive black hole with the mass of several  $10^6 M_{\odot}$  and has an accretion disk around the black hole. The estimated temperature of the ions in the disk is much higher than that of electrons which suggests that there are no efficient relaxation process between these two components and thus, this disk is considered to be “collisionless”. Since the relaxation process is very weak in the collisionless plasma, isotropy in the particle distribution is no longer valid. “Anisotropy” in the pressure which is one of the well known modification in collisionless plasma greatly modulates the feature of magnetic tension which act as a restoring force in MRI. Motivated by these facts, several attempts to include “collisionless” effects in the MRI simulation have been made by applying CGL (Chew-Goldberger-Low) approximation in MHD equations and assuming isotropization process via kinetic instabilities.

Since the early attempts were based on fluid framework, those kinetic effects are

---

not exactly taken into account. Recently by using 2.5 dimensional PIC simulations, kinetic process is included with self-consistent manner. However, since the time and spacial scale of the PIC simulation is restricted by electron dynamics it requires massive computational resources for the further long term 3 dimensional calculation. Considering the fact that in the actual disks ions are much hotter than electrons, hybrid framework, which treats only the ions as particles and assumes the electrons as charge neutralizing fluid, would provide a more robust approach for the collisionless accretion disk simulation.

In this study we developed a hybrid code to investigate the local evolution of collisionless differentially rotating system. By introducing the finite electron mass, we have overcome a numerical difficulties with which the hybrid code encounters in a problem which involves dynamical change of the plasma density and the magnetic field, such as MRI. By using this new hybrid code we have investigated a heavily non-linear stage of 2.5 dimensional MRI. In the non-linear stage, channel flows driven by MRI were corrupted due to the magnetic reconnection and formation of magnetic islands are observed. We have also evaluated the efficiency of the angular momentum transport in this non-linear stage from the stress components. These results are discussed in Chapter 2.

Motivated by the fact that the dissipation process is also important in the disk turbulence, we have investigated evolution of magnetic reconnection in differentially rotating system using the hybrid code as well. These are described in Chapters 3 and 4. In Chapter 3 we investigated the evolution of magnetic reconnection in the meridional plane of the disk. The initial magnetic field is aligned to the axis of rotation. Coupled with MRI, the magnetic reconnection showed a asymmetric structure during its evolution. At the same time, efficient reproduction of equatorial component of magnetic field is observed which is essential for Maxwell stress in the turbulence. We consider that the magnetic reconnection coupled with MRI contributes to efficient transportation of angular momentum.

In Chapter 4, we investigated evolution of magnetic reconnection in the equatorial plane of the disk. The initial magnetic field was aligned to the azimuthal direction of the disk in this simulation. Since we assume a local structure in the disk, we have adopted so-called “open shearing periodic boundary condition” which is commonly used in the MHD calculation of differentially rotating system. We have also observed asymmetric evolution of magnetic reconnection in this plane basically due to the coupling of the outflow with the Coriolis force. By assuming periodicity, the evolution of the reconnection was affected by another reconnection site which is assumed to exist outside the actual simulation domain. Together with the shear motion, this effect gave an enhancement on the reconnection rate with a certain rotational parameter. We consider that this can be one of the fundamental processes in the accretion disk turbulence.

The present results imply existence of an efficient angular momentum transport in a collisionless accretion disk. The method we have established in the present studies would be also an important step for the further 3 dimensional simulation of the collisionless accretion disks.

# *Acknowledgements*

The author wish to express his deepest appreciation to Prof. Masahiro Hoshino for delightful suggestions and encouragements during the course of this dissertation. This dissertation would not be completed without his supports. It was an honor to be in his laboratory and to have stimulating discussions.

The author wish to express special thanks to Dr. Takanobu Amano. His insightful advice in discussions always helped the author for the completion of this dissertation.

The author would also like to thank Prof. T.Yokoyama, Prof. T.Terasawa, Prof. M.Fujimoto, and Prof. Y.Saito who gave informative suggestions in the seminars. Their experienced advice encouraged author completing the dissertation.

The author wish to thank Mr. K.Higashimori, Mr. T.Saito, and Mr. K.Hirabayashi for fruitful discussions. Exchanging the ideas with them during the seminars and in the laboratory was always delightful.

Finally the author would like to express his gratitude to my family for emotional support and warm encouragements.

# Contents

<b>Abstract</b>	<b>ii</b>
<b>Acknowledgements</b>	<b>vi</b>
<b>Contents</b>	<b>vii</b>
<b>List of Figures</b>	<b>x</b>
<b>List of Tables</b>	<b>xiv</b>
<b>1 General Introduction</b>	<b>1</b>
1.1 Accretion Disk and $\alpha$ -Disk Model . . . . .	1
1.2 Magnetorotational Instability . . . . .	2
1.3 Collisionless Accretion Disk . . . . .	7
1.4 Collisionless MRI . . . . .	10
1.5 Magnetic Reconnection . . . . .	18
1.5.1 Overview . . . . .	18
1.5.2 Magnetic reconnection in Shear flow: Relations with MRI . .	19
1.6 Hybrid Simulation . . . . .	21
1.7 Goal of this Thesis . . . . .	23
1.7.1 Motivation . . . . .	23
1.7.2 Structure of this Thesis . . . . .	26
<b>2 Magnetorotational Instability in collisionless accretion disks</b>	<b>27</b>
2.1 Introduction . . . . .	28
2.2 Basic Equations and Setups . . . . .	32
2.2.1 Effect of the Keplerian rotation . . . . .	33
2.2.2 Finite electron mass . . . . .	35
2.2.3 Initial condition and Parameters . . . . .	39
2.3 Results . . . . .	42
2.3.1 Semi 1-Dimension: Linear test . . . . .	42
2.3.2 Overview of 2.5 Dimensional RUNS ( $\beta_i = 99$ Case) . . . . .	43
2.3.3 Generation of perpendicular pressure anisotropy . . . . .	46
2.3.4 Evolution of stress components and $\alpha$ . . . . .	47

---

2.3.5	Heating of the ions by magnetic reconnection . . . . .	49
2.3.6	$\beta_i=33$ Case (RUN B1) . . . . .	50
2.3.7	$\beta_i=333$ Case (RUN B3) . . . . .	53
2.4	Summary of this Chapter . . . . .	53
<b>3</b>	<b>Magnetic Reconnection in the Meridional Plane of the Disk</b>	<b>58</b>
3.1	Introduction . . . . .	59
3.2	Hybrid Simulation in a Differentially Rotating System . . . . .	61
3.2.1	Basic Equations . . . . .	61
3.2.2	Initial Conditions and Simulation method . . . . .	62
3.3	Results . . . . .	66
3.3.1	Overview . . . . .	66
3.3.2	Asymmetric evolution of out-of-plane magnetic field . . . . .	66
3.3.3	Migration of the X-points . . . . .	72
3.3.4	Magnetic reconnection as a trigger of the MRI . . . . .	75
3.4	Summary and Discussions . . . . .	81
<b>4</b>	<b>Magnetic Reconnection in the Equatorial Plane of the Disk</b>	<b>85</b>
4.1	Introduction . . . . .	86
4.2	Basic Equations and Setup . . . . .	89
4.2.1	Basic Equations . . . . .	89
4.2.2	Initial Condition . . . . .	90
4.2.3	Boundary Condition . . . . .	92
4.3	Results . . . . .	94
4.3.1	Asymmetric Evolution of Magnetic Reconnection . . . . .	94
4.3.2	Effect of the differential rotation on the reconnection rate . . . . .	101
4.4	Summary and Discussion . . . . .	105
<b>5</b>	<b>Summary and Future Inspections</b>	<b>108</b>
5.1	Summary of this Thesis . . . . .	108
5.2	Future inspections . . . . .	111
<b>A</b>	<b>Inclusion of Finite Electron Mass</b>	<b>114</b>
<b>B</b>	<b>Open Shearing Periodic Boundary condition</b>	<b>117</b>
<b>C</b>	<b>Methods for calculating differentially rotating system using hybrid code.</b>	<b>121</b>
<b>D</b>	<b>Resistivity Used in MRI Calculation</b>	<b>123</b>
<b>E</b>	<b>Harris solution in differentially rotating system</b>	<b>125</b>

**Bibliography**

**128**

# List of Figures

1.1	Schematic illustration of fundamental process of angular momentum transport in MRI. The angular momentum ( $\ell$ ) of the plasma particles (Red Oval) is transported by the magnetic field (Blue Line).	6
1.2	Chandra X-Ray view of Sgr A*. A supermassive black hole is believed to exist in the center of the image. Image Credit : NASA/CXC/MIT/F.K.Baganoff et al.	8
1.3	Estimated ion and electron temperature. In the inner region of the disk, the ions are estimated to be approximately $10^2$ times hotter than the electrons. Parameter $f$ corresponds to the fraction of the energy transfer. Here, fraction $1 - f$ of the dissipated energy is transferred to radiation. Reprinted by permission from Macmillan Publishers Ltd: <i>Nature</i> 374, 623-625 (Narayan et al. [1995]), © 1995.	9
1.4	Wavenumber ( $k$ ) versus growthrate ( $\gamma$ ) relation of MRI with varying pressure anisotropy parameter ( $\varepsilon$ ). Perpendicular pressure anisotropy modifies the unstable region to the larger scale, whereas the fastest growth rate is not changed.	13
1.5	Growth rate of MRI under given initial pressure anisotropy and wavenumber. The upper unstable region ( $p_{\perp 0}/p_{\parallel 0} - 1 \gtrsim 0$ ) corresponds to MRI, whereas the lower unstable region corresponds to firehose instability. In the case when perpendicular pressure dominates the unstable wavelength of MRI shifts to longer scale.	14
1.6	Growth rate of the parallel mode of “collisionless MRI”. Color contour corresponds to a normalized growth rate ( $\gamma/\Omega_0$ ). The initial $\beta_{\parallel}$ and $\beta_{\perp}$ were set to be 99 and 102, respectively. Initial $p_{\perp}/p_{\parallel}$ thus becomes 1.03.	15
1.7	Same as Figure 1.6. The initial $\beta_{\parallel}$ and $\beta_{\perp}$ were set to be 1500 and 1545.5. Initial $p_{\perp}/p_{\parallel}$ thus becomes 1.03, which is the same value used in Figure 1.6.	16
1.8	“Tilted” structure of the X-point due to the background shear flow. The top panel (a) has no flow whereas (b), (c), and (d) has a background shear flow aligned to anti-parallel magnetic field. Flows are streaming towards left in the top of the current sheet and towards right on the bottom. Reprinted with permission from Cassak [2011]. © 2011, AIP Publishing LLC.	20

2.1	Dispersion relation of transverse mode of linear waves. The dashed blue lines show a dispersion obtained from Hall MHD equations, whereas the red solid lines show the one obtained from the two fluid equations with mass ratio of $m_i/m_e = 25$ . Dashed black lines corresponds to ordinary shear Alfvén wave to which the Hall (Blue) and the two fluid (Red) results asymptotically reach in the MHD limit ( $k, \omega \rightarrow 0$ ). . . . .	37
2.2	Schematic illustration of initial condition used in this chapter. . . . .	40
2.3	Time evolution of “semi-1D” MRI. Color corresponds to ion density whereas the solid lines corresponds to magnetic field line. . . . .	43
2.4	Growth rate of MRI obtained from linear analysis of MHD equations (Solid line) and from semi 1D run of hybrid simulations (Open circles). . . . .	44
2.5	Time evolution of ion density (color) and magnetic field line (solid line). Initial plasma $\beta_i$ was set to be 99. . . . .	45
2.6	History of the magnetic energy averaged on the entire domain of the simulation. . . . .	46
2.7	Averaged pressure anisotropy (solid line) at $\Omega_0 t / 2\pi = 5.12$ . The initial $\beta_i$ was set to be 99. . . . .	48
2.8	Time evolution of stress components. . . . .	49
2.9	Time evolution of ion energy spectra in the non-linear stage of the MRI. Significant heating is observed after the onset of magnetic reconnection ( $\Omega_0 t / 2\pi = 5.32$ ). . . . .	50
2.10	Same as Figure 2.5. Initial $\beta_i$ was set to be 33. . . . .	51
2.11	Averaged pressure anisotropy from RUN B1 during the magnetic reconnection (black line) and after the reconnection (red line). Initial $\beta_i$ was set to be 33. . . . .	52
2.12	Same as Figure 2.6. Initial $\beta_i$ was set to be 33. . . . .	52
2.13	Same as Figure 2.5. Initial $\beta_i$ was set to be 333. . . . .	54
2.14	Same as Figure 2.6. Initial $\beta_i$ was set to be 333. . . . .	55
2.15	Averaged pressure anisotropy (solid line) at $\Omega_0 t / 2\pi = 8.86$ . The initial $\beta_i$ was set to be 333. . . . .	55
3.1	Schematic illustration of initial condition used in this chapter. . . . .	63
3.2	Time evolution of all runs. The color contour corresponds to ion density whereas the solid line corresponds to the magnetic field line. The figures are focused on the left half of the simulation domain. . . . .	67
3.2	Continued. . . . .	68
3.3	(Color) Out-of-plane magnetic field ( $B_y$ ) in the final stage of the simulation. $B_y$ in RUN E is remarkably enhanced due to the dynamo effect of the MRI. The figures are focused on the left half of the simulation domain. (Solid line) Magnetic field. . . . .	69
3.4	Focused view of out-of-plane magnetic field in RUN D. . . . .	70
3.5	Schematic plot of the Hall Field and the sheared Field. . . . .	71
3.6	Focused view of the X-point in RUN D. . . . .	73

3.7	Growth rate of MRI with varying Hall parameter ( $\Omega_0/\Omega_{ci}$ ). The sign (+) corresponds to the case that the ambient magnetic field is parallel to the Keplerian rotational vector and vice versa. For the the case $\Omega_0/\Omega_{ci} = -0.5$ , the entire region is unstable to MRI. . . . .	75
3.8	Time evolution of the density (color) and the magnetic field line (solid line) with reduced Hall effect. . . . .	76
3.9	The density (color) and the magnetic field line (solid line) at the middle stage of RUN E and RUN E2 (top), and at the final stage (bottom). . . . .	77
3.10	Time evolution of Magnetic Field Power from comparative runs (RUN E, RUN E2). . . . .	78
3.11	Long term evolution of RUN C2. The plots are focused on the left half of the simulation domain. . . . .	80
3.12	Time evolution of Magnetic field power calculated from RUN C2. . . . .	81
4.1	Schematic illustration of the simulation setup calculated in this chapter. . . . .	91
4.2	Time evolution of runs on the equatorial plane. Color contour corresponds to ion density whereas the solid line corresponds to the magnetic field line. The figures are focused on the central current sheet in which the localized resistivity and the initial perturbation are imposed. . . . .	95
4.2	Continued. . . . .	96
4.3	(Color) Radial ( $x$ -direction) component of the ion bulk velocity in the unit of Alfvén velocity defined in the initial parameter in the out of the current sheet region. . . . .	97
4.4	Schematic plot of RUN A including the “inner” and “outer” side of the actual simulation domain. The red box with solid line indicates the actual simulation domain we are calculating, whereas the white box with dashed line indicates the region we are showing in Figure 4.2 . . . . .	99
4.5	Schematic plot of RUN C taking the “shearing of the simulation domain” effect into account. The ghost domain in the inner boundary is sheared forward, whereas the ghost domain in the outer boundary is sheared backward. The red solid line indicates the actual simulation domain which we have calculated, and the white dashed line indicates the region shown in Figure 4.2. . . . .	100
4.6	Time evolution of reconnected magnetic flux of five runs. The maximum reconnected flux is observed around $\Omega_0/\Omega_{ci} \simeq 1.25 \times 10^{-3}$ . The dashed navy line corresponds to a fitting line obtained with least square method using flux data of RUN E from $\Omega_{ci}t = 200 - 413$ . . . . .	102
4.7	Ion density profile (color) at $\Omega_{ci}t \simeq 413$ in comparative simulations. Solid line corresponds to magnetic field line. . . . .	104
4.8	Time evolution of reconnected magnetic flux of comparative runs. The case with no Coriolis and tidal force has the maximum growth rate. . . . .	105

---

B.1	Schematic illustration of open shearing periodic boundary condition. The simulation domain is described with black grids whereas the ghost domain is described with gray grids. As the simulation goes on the ghost domain in the inner and outer side is convected due to the background shear motion. . . . .	118
B.2	Schematic illustration of a staggered mesh and open shearing boundary condition in the left side of the simulation domain. . . . .	119
E.1	The oscillation of the neutral point. The deviation from the initial neutral point ( $\delta x$ ) in the unit of inertia length is plotted in the vertical direction. . . . .	126

# List of Tables

2.1	Simulation Parameters for Test Runs. . . . .	41
2.2	Simulation Parameters for varying beta runs. . . . .	42
3.1	Simulation Parameters. . . . .	65
4.1	Simulation Parameters for magnetic reconnection in the equatorial plane of the disk. . . . .	93

# Chapter 1

## General Introduction

### 1.1 Accretion Disk and $\alpha$ -Disk Model

Accretion disks are commonly found in our universe. They form around a massive astrophysical object such as black holes, protostars, and binaries. They consist of gases, which rotate around a central massive objects. The rotating gas gradually accretes toward the central star releasing its gravitational potential energy (e.g., Frank et al. [2002]).

Since the rotation of the gas is supported by the gravity from the central star, the rotation of disks mainly have a Keplerian profile. In a Keplerian rotation, the gas must lose their angular momentum when they “accrete” into the central star, since the Keplerian rotation has an angular momentum profile which increases with the radius (Lynden-Bell and Pringle [1974]). In the actual disk, shear viscosity transports the angular momentum in outward direction, and as a result, the matters are transported inward. However, considering the source of the viscosity, simple molecular viscosity provided by the collisions between the particles constituting the gas is extremely small (e.g., Pringle [1981]).

To explain the efficient transportation of the angular momentum, enhancement

of the viscosity provided by the turbulence was introduced by Shakura and Sunyaev [1973]. In their modeling, the disk is in a turbulent state, and the strong turbulent viscosity is expected. The turbulent viscosity which contributes to the transportation of the angular momentum is related with the  $(r, \varphi)$  component of the stress assuming that the stress is proportional to the gas pressure,

$$W_{r\varphi} = \alpha P. \quad (1.1)$$

Here,  $r$  and  $\varphi$  correspond to the radial and azimuthal direction of the disk, respectively. In their model thermal equilibrium between the heat produced by the  $\alpha$  viscosity and the energy loss due to the black-body radiation was assumed. This model which has been widely accepted as a standard accretion disk model is called “ $\alpha$ -disk model”. Yet the model arose another question, how the turbulence is driven in the accretion disk. Balbus and Hawley [1991] have pointed out the importance of the magnetic field for the transportation of the angular momentum and proposed a hydromagnetic mechanism to drive turbulence in the disk which will be introduced in the next section.

## 1.2 Magnetorotational Instability

As we introduced in the previous section strong turbulence is required to explain an efficient transportation of angular momentum in an accretion disk. A plasma instability called Magnetorotational Instability (MRI) is believed to be a promising process to generate turbulence in the disk. The basic theory of the process is reported in late 1950’s-1960’s (Velikhov [1959], Chandrasekhar [1960]) in the context of stability of a differentially rotating conductive fluid. The importance of the instability in accretion disks as a driving process of turbulence is first pointed out by Balbus and Hawley [1991]. With a linear analysis of MHD equations in the

differential rotation, they gave an intuitive interpretation to this plasma instability. With their numerical simulation reported in the following papers (Hawley and Balbus [1991]; Hawley and Balbus [1992]) they have shown that this instability is indeed contributing to a transportation of angular momentum.

Here, in this section we will revisit basic feature of MRI introduced in Balbus and Hawley [1991]. We start from a set of MHD equations described in the differentially rotating system.

$$\frac{\partial \rho}{\partial t} = -\nabla \cdot (\rho \mathbf{v}) \quad (1.2)$$

$$\rho \left( \frac{\partial}{\partial t} + \mathbf{v} \cdot \nabla \right) \mathbf{v} = -\nabla p + \frac{1}{c} \mathbf{J} \times \mathbf{B} - \rho \nabla \Phi \quad (1.3)$$

$$\mathbf{J} = \frac{c}{4\pi} \nabla \times \mathbf{B} \quad (1.4)$$

$$\frac{\partial \mathbf{B}}{\partial t} = \nabla \times (\mathbf{v} \times \mathbf{B}) \quad (1.5)$$

$$\frac{p}{\rho^\gamma} = \text{const.} \quad (1.6)$$

Here  $\rho$  is the density of the plasma,  $\mathbf{v}$  is the velocity,  $\mathbf{B}$  is the magnetic field,  $p$  is the plasma pressure, and  $\Phi$  is the gravitational potential from the central massive object. Here since the MRI gives fastest growth rate in the parallel mode, and for simplicity, we restrict our analysis to the case  $\mathbf{k} \parallel \hat{\mathbf{e}}_z$ , where  $\mathbf{k}$  is the wavenumber vector and  $\hat{\mathbf{e}}_z$  is the unit vector of  $z$ -component. In Balbus and Hawley [1991], Boussinesq limit was assumed, but the basic feature of MRI is not affected by the choice of the equation of state since the acoustic mode decouples with MRI in the parallel limit of MRI. Therefore, we adopt adiabatic relation as an equation of state ( $\gamma = 5/3$ ) in this analysis. The above equations are expressed in cylindrical coordinate  $(r, \varphi, z)$ . At the initial equilibrium state Keplerian shear flow,

$$\mathbf{v}_0 = r\Omega \hat{\mathbf{e}}_\varphi \quad (1.7)$$

and magnetic field aligned to the rotation of the axis

$$\mathbf{B}_0 = B\hat{\mathbf{e}}_z \quad (1.8)$$

is assumed. Here  $\Omega$  is the Keplerian angular frequency and  $\hat{\mathbf{e}}_\varphi$  is the unit vector of  $\varphi$ . The stability of the system is investigated by searching the non-trivial solution of linearized and Fourier transformed set of equations (1.2)-(1.5). In this calculation, we focus on the perturbation whose scale is sufficiently smaller than the distance from the central star ( $R$ ),

$$|kR| \gg 1 \quad (1.9)$$

where  $k$  is the wavenumber of the given perturbation. By assuming so-called ‘‘local approximation’’ the set of equations expressed in the cylindrical representation reduces to the Cartesian form. Assuming all the perturbations to have the dependence of  $\propto \exp(-i\omega t + ikz)$ , the linearized set of equations (1.2)-(1.5) become,

$$\omega\delta\rho = \rho_0 k\delta v_z \quad (1.10)$$

$$-i\omega\rho_0\delta v_r - 2\rho_0\Omega\delta v_\varphi = ik\frac{B_z}{4\pi}\delta B_r \quad (1.11)$$

$$-i\omega\rho_0\delta v_\varphi + \rho_0\delta v_r\frac{\kappa^2}{2\Omega} = ik\frac{B_z}{4\pi}\delta B_\varphi \quad (1.12)$$

$$-i\omega\rho_0\delta v_z = -ik\delta p \quad (1.13)$$

$$\omega\delta B_r = -kB_z\delta v_r \quad (1.14)$$

$$\omega\delta B_\varphi = -kB_z\delta v_\varphi - \frac{ikB_z}{\omega}\frac{d\Omega}{d\log r}\delta v_r \quad (1.15)$$

After some algebra we obtain a following dispersion relation,

$$(\omega^2 - k^2V_A^2)^2 = 4\Omega^2\omega^2 + (\omega^2 - k^2V_A^2)\frac{d\Omega^2}{d\log r}, \quad (1.16)$$

where  $V_A = B/\sqrt{4\pi\rho}$  is Alfvén velocity. Here, we have restricted the analysis to a parallel mode of MRI for simplicity. The dispersion (1.16) allows unstable solution

( $\omega^2 < 0$ ) when the angular frequency of the disk rotation is outwardly decreasing,

$$\frac{d\Omega}{d\log r} < 0. \quad (1.17)$$

This is also satisfied in the Keplerian rotation ( $\Omega \propto r^{-3/2}$ ), and the critical condition of the instability is given by

$$\frac{\Omega^2}{k^2 V_A^2} > \frac{1}{3}. \quad (1.18)$$

So, MRI is unstable to the longer wavelength modes.

The equation of motion described with Lagrangian displacement introduced in Balbus and Hawley [1998] gives an intuitive understanding of angular momentum transport by MRI. Replacing  $-i\omega \rightarrow \partial/\partial t$ ,  $ik \rightarrow \partial/\partial z$ ,  $\delta\mathbf{v} \rightarrow \partial\boldsymbol{\xi}/\partial t$ , in (1.10)-(1.15) we obtain

$$\frac{\partial^2 \xi_r}{\partial t^2} - 2\Omega \frac{\partial \xi_\varphi}{\partial t} = - \left[ \frac{d\Omega^2}{d\log r} + (kV_A)^2 \right] \xi_r \quad (1.19)$$

$$\frac{\partial^2 \xi_\varphi}{\partial t^2} + 2\Omega \frac{\partial \xi_r}{\partial t} = - (kV_A)^2 \xi_\varphi. \quad (1.20)$$

Since Equations (1.19) and (1.20) has the form of oscillatory equation, the process of MRI is often compared with 2 dimensional behavior of particles banded with spring. Here spring constant for  $r$ -direction motion is ( $d\Omega^2/d\log r + k^2 V_A^2$ ) and the constant becomes negative when Equation (1.18) is satisfied. Figure 1.1 shows a schematic illustrations of the basic feature of MRI. In the top panel two fluid particles threaded with magnetic field is described on the meridional plane ( $r, z$ ) of the disk. In the bottom panel, the view on the equatorial plane ( $r, \varphi$ ) is described. When two fluid particles banded with a spring is perturbed, the transportation of the angular momentum between these two particles takes place due to the restoring force provided by the spring. Physically, the magnetic tension plays a role of the spring. Observed from the corotating frame the particle went inside obtains ( $+\varphi$ ) displacement due to the shear motion, whereas the particle went outside obtains

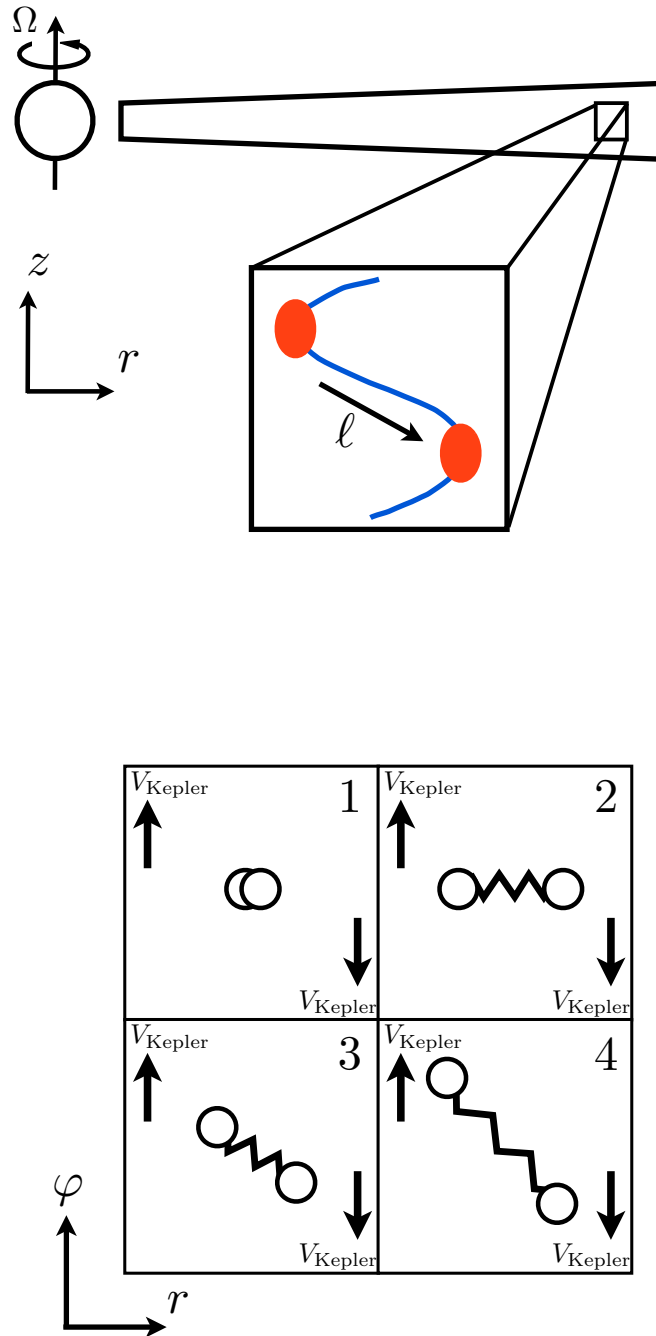


FIGURE 1.1: Schematic illustration of fundamental process of angular momentum transport in MRI. The angular momentum ( $\ell$ ) of the plasma particles (Red Oval) is transported by the magnetic field (Blue Line).

$(-\varphi)$  displacement. Since the particles are banded by a spring, the inner particle is pulled by the tension and loses angular momentum, and at the same time, the outer particle gains angular momentum. The process takes place continuously and as a result, the system would be unstable. When the spring constant is too strong, (i.e., the magnetic field is strong) the particles just keep on oscillating. Driven by this fundamental process MRI enhances equatorial component of magnetic field  $(B_r, B_\varphi)$ . The enhanced magnetic field however is dissipated by the magnetic reconnection, and as a result, turbulence is driven.

### 1.3 Collisionless Accretion Disk

As we revisited in the previous section, the conventional theory of MRI has been focused on the “collisional plasma” whose average collision time scale of the plasma particles is sufficiently short compared to that of the Keplerian rotation. Studies of MRI with collisional plasma has been based on the isotropic MHD equations. However, several observational results indicate that some class of the accretion disks are constituted of collisionless plasma.

Figure 1.2 shows a Chandra X-Ray view of the Sgr A\* which is in our galactic center. A supermassive black hole with the mass of several times of  $10^6 M_\odot$  is considered to be located in the center of this object (Schödel et al. [2002]; Ghez et al. [2003]).

The accretion feature of the disk around this supermassive black hole is rather confusing. The contradiction between the observations of disk is reviewed by Quataert [2003]. Assuming that the disk is modeled by the standard  $\alpha$ -disk model (Shakura and Sunyaev [1973]) we obtain mass accretion rate from the observed luminosity of the disk. However, the mass accretion rate estimated with the  $\alpha$  disk model, is several orders smaller compared to the Bondi accretion rate (Bondi [1952]) which is estimated with the disk density ( $\sim 100 \text{ cm}^{-3}$ ) given by another observation (Krabbe et al. [1991]).



FIGURE 1.2: Chandra X-Ray view of Sgr A\*. A supermassive black hole is believed to exist in the center of the image. Image Credit : NASA/CX-C/MIT/F.K.Baganoff et al.

The accretion model which explains this contradiction was proposed by Narayan and Yi [1994] and Narayan and Yi [1995]. They introduced a new parameter  $f$  which characterizes the rate of energy exchange. In their model, the fraction  $1-f$  of the energy dissipated by shear viscosity is transformed to radiation. Thus  $f \rightarrow 0$  corresponds to a standard  $\alpha$ -disk model. They further extended their model based on Advection Dominated Accretion Flow (ADAF) permitting a two temperature plasma. The model included a cooling process by bremsstrahlung, synchrotron and Comptonization (Narayan et al. [1995]). Obtained model spectrum showed a good agreement with the observation implying the validity of two temperature assumption. Figure 1.3 shows a radial dependence of the ion/electron temperature obtained from their modeling. While ions keep virial temperature in the inner radius, electrons are cooled by the radiation process which are taken into account.

This result implies there are no effective relaxation process between the ions and electrons and thus, the plasma constituting the accretion disk around Sgr A\* is collisionless. As it will be introduced in the next section, magnetic tension

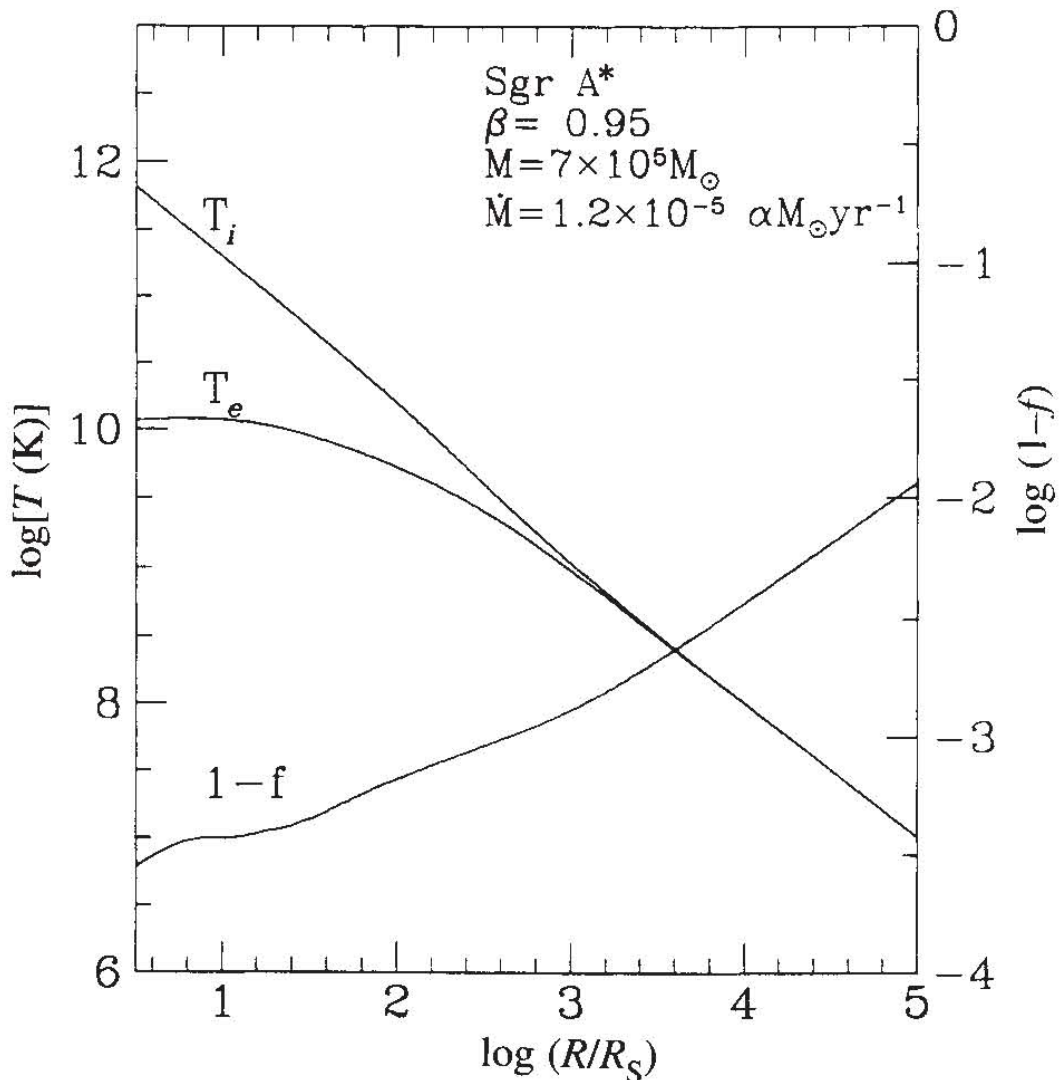


FIGURE 1.3: Estimated ion and electron temperature. In the inner region of the disk, the ions are estimated to be approximately  $10^2$  times hotter than the electrons. Parameter  $f$  corresponds to the fraction of the energy transfer. Here, fraction  $1 - f$  of the dissipated energy is transferred to radiation. Reprinted by permission from Macmillan Publishers Ltd: *Nature* 374, 623-625 (Narayan et al. [1995]), © 1995.

which plays a crucial role in the linear process of MRI is greatly modified in the collisionless plasma. Therefore, the conventional treatment based on MHD analysis may not be valid in these types of accretion disk. In the next section, we

will introduce the previous attempts to take the effect of low collisionality in the theory of MRI.

## 1.4 Collisionless MRI

### Theoretical approach

Motivated by the observational facts both theoretical and numerical attempts has been proposed to include the effect of low collisionality in the theory of MRI. One of the major characteristics of the collisionless plasma is generation of pressure anisotropy with respect to the local magnetic field (Chew et al. [1956]; Kulsrud [1983]). This pressure anisotropy was included to conventional MHD equations by considering equation of motions obtained from the conservation of adiabatic constants,

$$\frac{d}{dt} \left( \frac{p_{\perp}}{\rho B} \right) = 0 \quad (1.21)$$

$$\frac{d}{dt} \left( \frac{p_{\parallel} B^2}{\rho^3} \right) = 0 \quad (1.22)$$

Here  $p_{\parallel}$  and  $p_{\perp}$  are the parallel and perpendicular pressure with respect to the local magnetic field. In this section we will look at a basic modification on the linear feature of MRI given by the pressure anisotropy, following the analysis reported in Quataert et al. [2002].

The qualitative modification on MRI can be evaluated by the linear analysis of MRI with the initial pressure anisotropy.

$$\frac{\partial \rho}{\partial t} = -\nabla \cdot (\rho \mathbf{v}) \quad (1.23)$$

$$\rho \left( \frac{\partial}{\partial t} + \mathbf{v} \cdot \nabla \right) \mathbf{v} = -\nabla \cdot \mathbf{P} + \frac{1}{c} \mathbf{J} \times \mathbf{B} - \rho \nabla \Phi \quad (1.24)$$

$$\mathbf{J} = \frac{c}{4\pi} \nabla \times \mathbf{B} \quad (1.25)$$

$$\frac{\partial \mathbf{B}}{\partial t} = \nabla \times (\mathbf{v} \times \mathbf{B}) \quad (1.26)$$

$$\mathbf{P} = p_{\perp} \mathbf{I} + (p_{\parallel} - p_{\perp}) \hat{\mathbf{b}} \otimes \hat{\mathbf{b}} \quad (1.27)$$

$$\frac{p_{\perp}}{\rho B} = \text{const.} \quad (1.28)$$

$$\frac{p_{\parallel} B^2}{\rho^3} = \text{const.} \quad (1.29)$$

Here  $\hat{\mathbf{b}}$  is the unit vector parallel to the local magnetic field. As we have assumed in Section 1.2, we also assume a parallel mode of MRI in this analysis. Note that the only difference is the pressure term in the equation of motion (1.24), which is replaced to a 2nd order pressure tensor. Here as we consider parallel mode of MRI for simplicity, the longitudinal and transverse mode wave decouples. As we will introduce in the next section, a heat flux model is discussed in the CGL equations of state. Since the heat flux modifies the longitudinal mode which completely decouples in the parallel limit, we simply adopt the ideal CGL equations of state. The linearized, and Fourier transformed set of the equations (1.23)-(1.26) yields,

$$\omega \delta \rho = \rho_0 k \delta v_z \quad (1.30)$$

$$-i\omega \rho_0 \delta v_r - 2\rho_0 \Omega \delta v_{\varphi} = ik \left[ \frac{B_z}{4\pi} - \frac{(p_{\parallel 0} - p_{\perp 0})}{B_z} \right] \delta B_r \quad (1.31)$$

$$-i\omega \rho_0 \delta v_{\varphi} + \rho_0 \delta v_r \frac{\kappa^2}{2\Omega} = ik \left[ \frac{B_z}{4\pi} - \frac{(p_{\parallel 0} - p_{\perp 0})}{B_z} \right] \delta B_{\varphi} \quad (1.32)$$

$$-i\omega \rho_0 \delta v_z = -ik \delta p_{\parallel} \quad (1.33)$$

$$\omega \delta B_r = -k B_z \delta v_r \quad (1.34)$$

$$\omega \delta B_{\varphi} = -k B_z \delta v_{\varphi} - \frac{ik B_z}{\omega} \frac{d\Omega}{d \log r} \delta v_r. \quad (1.35)$$

Comparing the linearized equations (1.10)-(1.15) and equations (1.30)-(1.35), the additional term only appears in the right hand side of the  $(r, \varphi)$  component of the equation of motion. This term corresponds to the magnetic tension, and when we permit initial pressure anisotropy, the magnetic tension is weakened when the parallel pressure is initially higher than the perpendicular pressure. This modification on the magnetic tension arises from the centrifugal force which the particle

streaming along the perturbed magnetic field feels. Since there are more particles carrying the parallel velocity in the  $p_{\parallel 0} > p_{\perp 0}$  case, the enhanced centrifugal force effectively weakens the restoring force of magnetic tension.

Again, applying straight forward algebra on equations (1.30)-(1.35), we get

$$\left[\omega^2 - k^2 (\sqrt{\varepsilon} V_A)^2\right]^2 = 4\Omega^2 \omega^2 + \left[\omega^2 - k^2 (\sqrt{\varepsilon} V_A)^2\right] \frac{d\Omega^2}{d\log r}, \quad (1.36)$$

where  $\varepsilon$  is defined as,

$$\varepsilon \equiv 1 - \frac{\beta_{\parallel 0} - \beta_{\perp 0}}{2}, \quad (1.37)$$

and the  $\beta_{\parallel 0}$  and  $\beta_{\perp 0}$  are the plasma beta defined with the initial parallel and perpendicular pressure, respectively. Note that the only difference appears in the Alfvén velocity which is replaced to  $\sqrt{\varepsilon} V_A$ . In the non-rotating limit ( $\Omega \rightarrow 0$ ) the dispersion reduces to that of shear Alfvén wave under the existence of initial pressure anisotropy, and  $\varepsilon = 0$  gives a critical condition of firehose instability. The dispersion physically describes the fact that only the magnetic tension which acts as a restoring force in MRI, is modified by the initial pressure anisotropy, whereas the basic mechanism of MRI remains unchanged. In Figure 1.4 we plot the growth rate with varying anisotropy parameter ( $\varepsilon$ ). The unstable region of MRI is extended due to the reduced magnetic tension due to the parallel pressure anisotropy. Since the basic mechanism of MRI remains unchanged, the unstable region and the fastest growing wavelength is modified to the larger scale, whereas the fastest growth rate is unchanged.

However, parallel pressure anisotropy does not necessarily extends the unstable region of MRI. In Figure 1.5, we plot growth rate of MRI and firehose instability with given initial anisotropy  $p_{\perp 0}/p_{\parallel 0} - 1$  (vertical axis) and normalized wavenumber  $kV_A/\Omega_0$  (horizontal axis). Here we consider parallel mode, and the plasma beta defined with perpendicular pressure ( $\beta_{\perp}$ ) is set to be 1000. As we can see from the plot MRI is severely restricted when the parallel pressure dominates. and

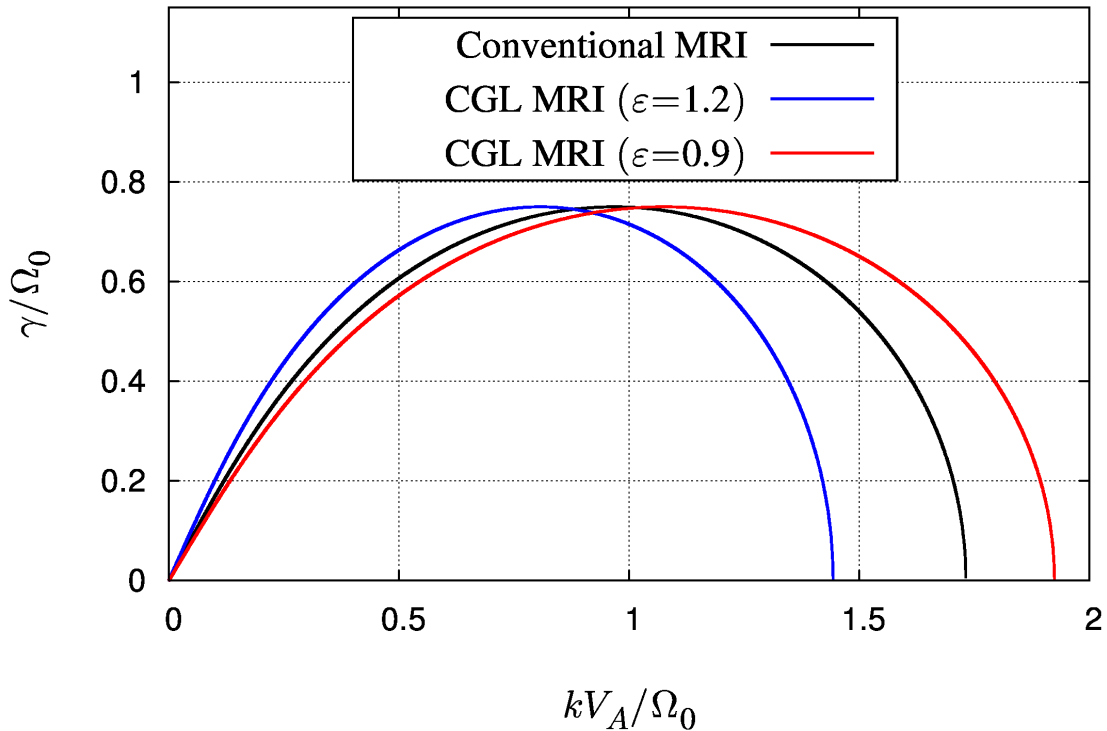


FIGURE 1.4: Wavenumber ( $k$ ) versus growthrate ( $\gamma$ ) relation of MRI with varying pressure anisotropy parameter ( $\varepsilon$ ). Perpendicular pressure anisotropy modifies the unstable region to the larger scale, whereas the fastest growth rate is not changed.

the firehose instability will be the unstable mode. This is due to the fact that in the high  $\beta_{\parallel}$  plasma, criteria for the firehose instability  $\varepsilon = 0$  is easily attained. In the case when  $p_{\perp 0} > p_{\parallel 0}$ , the fastest growing wavelength shifts to a longer scale because in this case, the magnetic tension is effectively enhanced.

Having revisited a basic feature of “collisionless MRI” with the parallel mode of linear analysis, let us now look on to the oblique mode of the instability. Here we assume  $\partial/\partial r \neq 0$ , and all the perturbed quantities are proportional to  $\exp(-i\omega t + ik_r r + ik_z z)$ . In the oblique analysis, acoustic mode and transverse mode (MRI) no longer decouple and the choice of the equation of state would modify the linear evolution of the system. Here we adopt CGL equations with parallel heat flux due to the Landau damping introduced in Snyder et al. [1997].

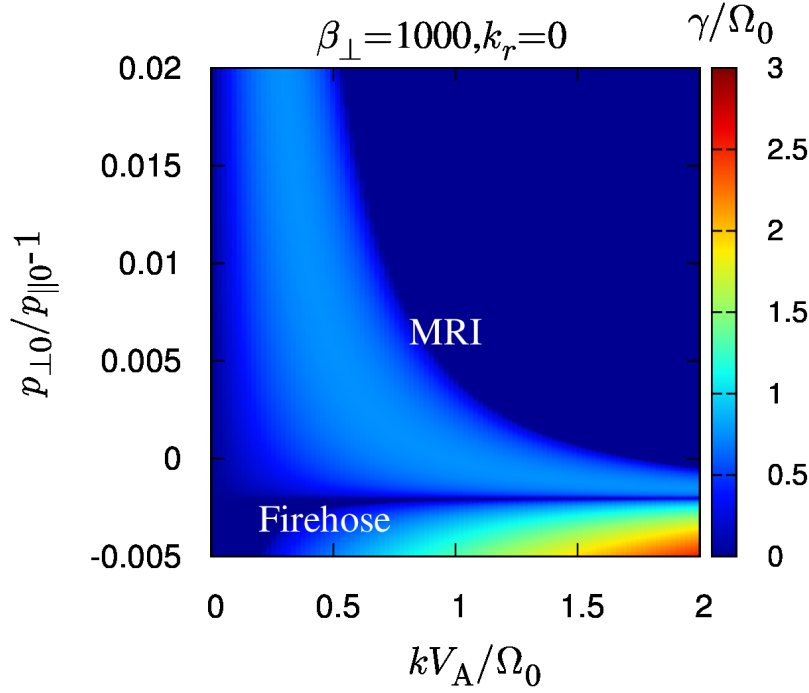


FIGURE 1.5: Growth rate of MRI under given initial pressure anisotropy and wavenumber. The upper unstable region ( $p_{\perp 0}/p_{\parallel 0} - 1 \gtrsim 0$ ) corresponds to MRI, whereas the lower unstable region corresponds to firehose instability. In the case when perpendicular pressure dominates the unstable wavelength of MRI shifts to longer scale.

The corresponding equations take the form as follows.

$$\rho B \frac{d}{dt} \left( \frac{p_{\perp}}{\rho B} \right) = -\nabla \cdot (\hat{\mathbf{b}} q_{\perp}) - q_{\perp} \nabla \cdot \hat{\mathbf{b}} \quad (1.38)$$

$$\frac{\rho^3}{B^2} \frac{d}{dt} \left( \frac{p_{\parallel} B^2}{\rho^3} \right) = -\nabla \cdot (\hat{\mathbf{b}} q_{\parallel}) - 2q_{\perp} \nabla \cdot \hat{\mathbf{b}}. \quad (1.39)$$

Here,  $q_{\parallel}$  and  $q_{\perp}$  are the parallel heat flux and take the form as follows,

$$q_{\parallel} = -\sqrt{\frac{8}{\pi}} \rho_0 c_{\parallel 0} \frac{ik_{\parallel} p_{\parallel}}{|k_{\parallel}| \rho} \quad (1.40)$$

$$q_{\perp} = -\sqrt{\frac{2}{\pi}} \rho_0 c_{\parallel 0} \frac{ik_{\parallel} p_{\parallel}}{|k_{\parallel}| \rho} + \sqrt{\frac{2}{\pi}} c_{\parallel 0} \frac{p_{\perp 0}}{B_0} \left( 1 - \frac{p_{\perp 0}}{p_{\parallel 0}} \right) \frac{ik_{\parallel} B}{|k_{\parallel}|}. \quad (1.41)$$

Again, following to the analysis introduced in Sharma et al. [2006] and after cumbersome but straight forward calculation, we obtain a dispersion relation. The

resulting dispersion is rather complicated to express, so we just show some plots with varying initial plasma  $\beta$ .

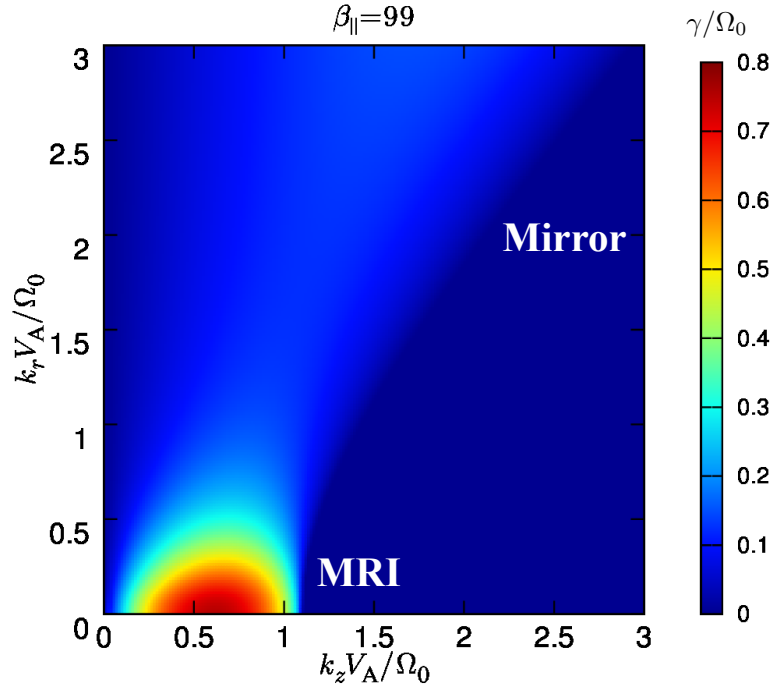


FIGURE 1.6: Growth rate of the parallel mode of “collisionless MRI”. Color contour corresponds to a normalized growth rate ( $\gamma/\Omega_0$ ). The initial  $\beta_{\parallel}$  and  $\beta_{\perp}$  were set to be 99 and 102, respectively. Initial  $p_{\perp}/p_{\parallel}$  thus becomes 1.03.

Figures 1.6 and 1.7 show a growth rate plot of the dispersion. As we focus on the oblique mode, we take normalized wavenumber along  $z$ -direction on the horizontal axis and  $x$ -direction on the vertical axis. In both plots, the initial perpendicular pressure was set to be slightly higher than the parallel pressure ( $p_{\perp 0}/p_{\parallel 0} = 1.03$ ). In both plot, the MRI active region is restricted in the vicinity of the origin. As we can see from the plot, the fastest growing mode of MRI is the parallel mode. Another unstable region found in large  $k$  is the mirror mode. This instability grows when the perpendicular pressure is sufficiently larger than the parallel pressure. As we can see from these two figures the MRI active region is extremely sensitive to the initial plasma  $\beta$ , and  $\beta \gtrsim 1000$  gives extremely severe restriction on the linear growth of MRI. Since the accretion disk is constituted with a high

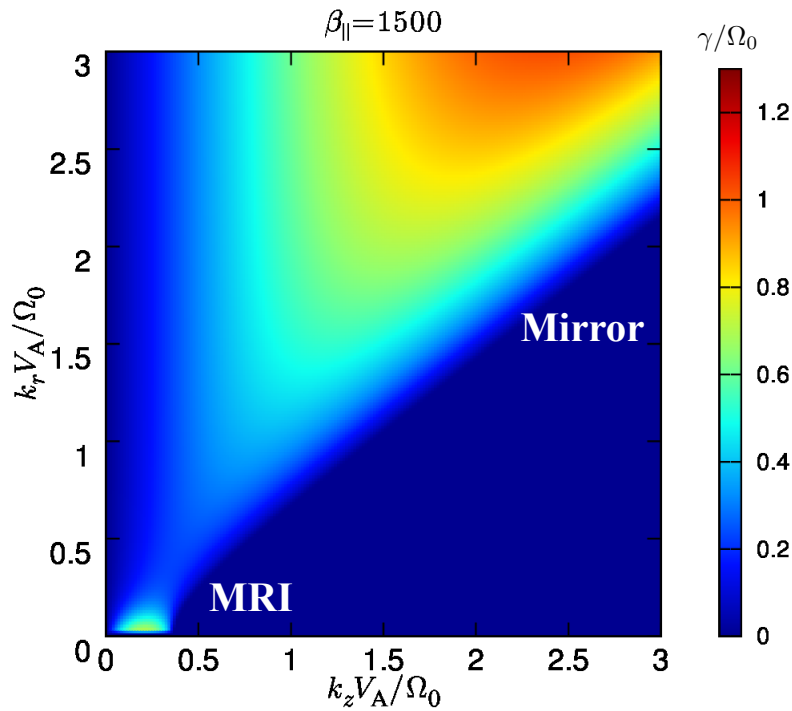


FIGURE 1.7: Same as Figure 1.6. The initial  $\beta_{\parallel}$  and  $\beta_{\perp}$  were set to be 1500 and 1545.5. Initial  $p_{\perp}/p_{\parallel}$  thus becomes 1.03, which is the same value used in Figure 1.6.

$\beta$  plasma, this feature of MRI can be a severe problem. Even one starts from an isotropic plasma, magnetic field enhanced by MRI produces perpendicular pressure anisotropy obeying to the CGL equation (1.28) and MRI dies out.

Though the above simple linear consideration implies the stabilization of MRI, there are some relaxation processes to isotropize the plasma. This is attained by considering a pitch angle scattering of the ions by several kinetic plasma instabilities associated with pressure anisotropy. These processes are heavily non-linear and taken into account with a numerical simulation.

### Numerical approach

As pointed out from the theoretical consideration, the growth of MRI is disturbed due to the perpendicular pressure anisotropy which MRI itself generates. However, there are possible competing processes which isotropize the plasma via several

kinetic instabilities. Motivated by these facts, Sharma et al. [2006] carried so-called “collisionless MHD” simulation of local 3D evolution of MRI. They took the effect of low collisionality by using CGL equations as an equation of state. In addition, they took the effect of parallel heat flux into account with the form introduced in equations (1.38)-(1.41). They have also taken an isotropization process into account. Since the MHD code cannot resolve spacial and temporal scale of the ion kinetics, they have taken this kinetic process into account by setting upper and lower limit to the local pressure anisotropy at each time step of the calculation. The upper and lower limit of pressure anisotropy they set were based on the kinetic firehose (Kennel and Sagdeev [1967]), mirror (Hasegawa [1969]) and ion-cyclotron instabilities (Gary et al. [1997]). They have confirmed that without an effective pitch angle scattering model (i.e., only with CGL approximation), perpendicular pressure anisotropy generated by the linear growth of MRI prevents the further growth of MRI. However with appropriate pitch angle scattering model, they have reported the non-linear growth of MRI and resulting turbulence.

To take the process of pitch angle scattering with a self-consistent manner, particle based simulation of MRI has been reported recently. Riquelme et al. [2012] have reported a 2.5D full particle (PIC) calculation of MRI and they have also confirmed that the pressure anisotropy generated by MRI is indeed relaxed and non-linear growth of MRI was observed. Hoshino [2013] has extended the study to high  $\beta$  plasma using 2.5D full particle code as well. In the final state of their calculation, the system reached to a quasi steady state and the  $\alpha$ -parameter which is the rate of the angular momentum transport (Shakura and Sunyaev [1973]) was evaluated. The obtained  $\alpha$  lied in 0.1-1 which is an order of magnitude larger than the typical results from the fluid based code.

Despite the success in the “collisionless MHD” code and full particle code, there are no reports of the non-linear evolution of MRI using hybrid code. Hybrid code which assumes ions as particles and electrons as a massless charge neutralizing fluid is expected to be a robust approach to investigate the 3D, non-linear evolution of MRI. Compared to PIC code, hybrid code has an advantage considering the

numerical resource. However, until now, the only MRI simulation reported using hybrid code remains in the linear to quasi-linear evolution (Kunz et al. [2014b]), possibly due to the numerical difficulties associated to the hybrid code, which will be introduced in this thesis.

## 1.5 Magnetic Reconnection

### 1.5.1 Overview

Magnetic reconnection is a plasma process which transforms magnetic energy to kinetic and thermal energy of the plasma. The rapid transformation of energy is attained involving the change in the magnetic field topology (Sweet [1958]; Parker [1957]), or together with dissipation via slow shocks (Petschek [1964]) permitting even more rapid energy transformation. This process has been widely discussed to explain various phenomena in the space physics such as a mixing of the interplanetary plasma and the magnetospheric plasma (Dungey [1961]) and rapid energy release in the solar flare (e.g., Tsuneta [1996]).

Numerically, magnetic reconnection has been studied in various scales ranging from PIC (e.g., Pritchett [2001]), hybrid (e.g., Kuznetsova et al. [1998]; Hesse and Winske [1994]), to MHD (e.g., Sato and Hayashi [1979]). Those simulation results using these different codes are compared in Birn et al. [2001]. Of the four simulations (PIC, hybrid, Hall MHD, MHD), high reconnection rate was observed in the code which includes the Hall term. Together with the result that the reconnection rate was insensitive to the ion to electron mass ratio (Pritchett [2001]), they have concluded that the Hall term is crucial to a fast reconnection.

Theoretically, importance of the Hall term in thin current sheet was pointed out by Terasawa [1983] who carried linear analysis of the tearing mode incompressible Hall MHD. They have shown that the Hall current due to the different magnetization degree between ions and electrons (Sonnerup [1979]), accelerates the growth

of tearing mode. This feature was remarkable when the initial width of the current sheet is comparable to the ion inertia length.

Observationally Asano et al. [2003] showed the existence of the thin current sheet whose current sheet width reaches to ion inertia length from the GEOTAIL data. The result shows an importance of the Hall term in the magnetic reconnection which takes place in the actual space environment.

### **1.5.2 Magnetic reconnection in Shear flow: Relations with MRI**

Considering the interplay with MRI, magnetic reconnection also plays an important role in the accretion disk turbulence by releasing the magnetic energy enhanced by MRI (Hawley and Balbus [1992]). As we have introduced in Section 1.1, the efficiency of the angular momentum transport is determined by saturated state of MRI induced turbulence. As reviewed in Balbus and Hawley [1998] the saturated quasi steady state of MRI-induced turbulence is reached by the balance between dynamo effect of MRI and dissipation by magnetic reconnection.

To our knowledge, studies focusing on the evolution of the magnetic reconnection under the effect of differential rotation has never been reported. However regarding that the differential rotation is well approximated by the shear flow in the localized frame, several studies are found, pointing out the importance of the shear flow on the evolution of magnetic reconnection.

Those studies are motivated by magnetopause reconnection, which involves a strong shear flow (Gosling et al. [1986]) aligned to the anti-parallel magnetic field. Various studies pointed out that the structure of the X-point is modulated by the background shear flow and the reconnection site is tilted with respect to the initial current sheet (e.g., La Belle-Hamer et al. [1994]; Cassak [2011]). Figure 1.8 shows a tilted X-point from the simulation carried by Cassak [2011]. The origin of the tilt is also discussed in Cassak [2011] as a twisting of the outflow due to the dynamic

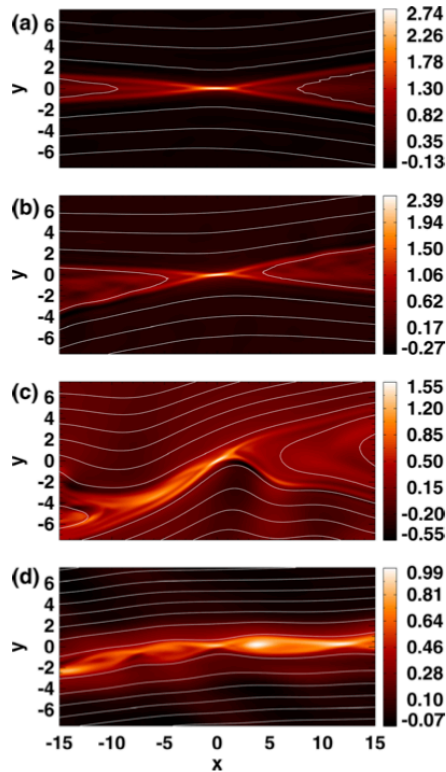


FIGURE 1.8: “Tilted” structure of the X-point due to the background shear flow. The top panel (a) has no flow whereas (b), (c), and (d) has a background shear flow aligned to anti-parallel magnetic field. Flows are streaming towards left in the top of the current sheet and towards right on the bottom. Reprinted with permission from Cassak [2011]. © 2011, AIP Publishing LLC.

pressure given by the shear flow. In their interpretation, the outflow is tilted to the region where the direction of the shear flow is opposite to the outflow. In addition to the tilted structure, reduction of the reconnection rate is observed. Applying the Sweet-Parker analysis with the existence of the shear flow, they proposed a scaling law of reconnection rate  $E$  which decreases as the rate of shear increases,

$$E = E_0 \left( 1 - \frac{v_s^2}{V_A^2} \right). \quad (1.42)$$

where  $E_0$  is the reconnection rate in the absence of shear flow,  $V_A$  is the Alfvén velocity defined outside the current sheet region, and  $v_s$  is the magnitude of shear across the current sheet width.

In the non-linear state of MRI, the azimuthal component of the magnetic field

is dominant due to the dynamo effect of the Keplerian shear. Therefore, the dissipation process of the magnetic field enhanced by MRI is similar to the setup introduced above and the modification on the reconnection rate by the background shear might be an important factor since the dissipation by the magnetic reconnection determines the saturation stage.

## 1.6 Hybrid Simulation

In this thesis, we will investigate local behavior of collisionless accretion disks including the kinetic effect of the plasma. As introduced in the section 1.3, the temperature of the ions are estimated to be much higher than that of the electrons. This means, in the “first order approximation”, the kinetic effect of the ions are important compared to that of the electrons. In this class of plasmas, hybrid simulation (e.g., Lipatov [2002]) will provide us a reasonable approximation. In this section, let us first introduce the conventional sets of the hybrid equations. In the following chapters, we will introduce additional modifications which are newly included in our study, such as effect of the Coriolis and tidal forces, and effect of finite electron mass. hybrid simulation is used to investigate evolution of plasmas when one aims to focus on the kinetic effect of the ions and that of the electrons is relatively minor. The ions are treated as superparticles and their positions and velocities are updated with the Lorentz equations,

$$\frac{d\mathbf{x}_i}{dt} = \mathbf{v}_i \quad (1.43)$$

$$m_i \frac{d\mathbf{v}_i}{dt} = q_i \mathbf{E} + q_i \frac{\mathbf{v}_i}{c} \times \mathbf{B} \quad (1.44)$$

Subscript “i” means that the corresponding physical values are those of the ions. Here  $\mathbf{x}_i$  is the position,  $\mathbf{v}_i$  is the velocity,  $m_i$  is the mass,  $q_i$  is the electric charge.  $\mathbf{E}$  and  $\mathbf{B}$  are the electric and magnetic fields, respectively and  $c$  is the speed of light. Since in the hybrid framework, one would focus on the scale of ion inertia

length, and the ions are not frozen-in to the magnetic field. Electrons on the other hand, are assumed to be magnetized and massless fluid and the Ohm's law is given by,

$$\mathbf{E} = -\frac{1}{c}\mathbf{V}_e \times \mathbf{B} + \frac{\nabla P_e}{n_e q_e}. \quad (1.45)$$

Again, subscript “e” means that the corresponding physical values are those of the electrons. Here,  $\mathbf{V}_e$  is the bulk velocity of the electrons and  $P_e$  is the pressure,  $n_e$  is the number density and  $q_e$  is the electron charge. As we assume electrons are massless charge neutralizing fluid, any static field is relaxed within the shorter time scale compared to the simulation time step and as a result, quasi-neutral condition

$$n_e \simeq n_i \quad (1.46)$$

holds. In practice we use  $n_e = n_i$  to obtain electron number density, and  $n_i$  which is the ion number density is calculated through appropriate moment calculations for ion particles. Electron bulk velocity is obtained from Ampère's law

$$\mathbf{J} = \mathbf{J}_e + \mathbf{J}_i = \frac{c}{4\pi} \nabla \times \mathbf{B} \quad (1.47)$$

where  $\mathbf{J}$  is the total current density, and  $\mathbf{J}_e$  and  $\mathbf{J}_i$  are the current density of the electrons and ions, respectively. Here, magnetic field must satisfy the solenoidal condition,

$$\nabla \cdot \mathbf{B} = 0. \quad (1.48)$$

By applying moment calculation on the ion velocity, we first obtain ion bulk velocity ( $\mathbf{V}_i$ ). Then from Equation (1.47), we obtain the electron bulk velocity,

$$\mathbf{V}_e = -\frac{\mathbf{J}_i}{n_e q_e} + \frac{c}{4\pi n_e q_e} \nabla \times \mathbf{B}. \quad (1.49)$$

Electron pressure is calculated through an appropriate equation of state. In this thesis, we focus both on the Keplerian time scale and the time scale which is related to the pitch angle scattering of the ions. These time scales are in general, much longer compared to that of electron kinetics. Therefore in the present calculation we obtain  $P_e$  from the adiabatic relation

$$P_e \propto n_e^\gamma \quad (1.50)$$

and anisotropy for electrons is not assumed. Here,  $\gamma$  is the adiabatic constant and in this thesis, we use 5/3. Finally, with Faraday's law, we obtain a closed set of the equations

$$\frac{\partial \mathbf{B}}{\partial t} = -c \nabla \times \mathbf{E}. \quad (1.51)$$

These are the conventional equation set of the hybrid simulation. To investigate the behavior of the differentially rotating system, we have to include the effect of the gravity. Inclusion and expression of these effects under the so-called ‘‘local approximation’’ is introduced in Chapter 2.

## 1.7 Goal of this Thesis

### 1.7.1 Motivation

As we have introduced in the previous sections, collisionless effect of the plasma would modify the feature of MRI not only in the linear growth state but also in the non-linear, turbulent state. In the collisionless accretion disk, generation of pressure anisotropy driven by the strong dynamo effect of the differential rotation and isotropization of the pressure through pitch angle scattering by the kinetic instabilities take place at the same time. Theoretically, generation of pressure anisotropy can be investigated with the CGL equations of state. A set of MHD

equations with CGL equations has no typical spacial and temporal scale. However, since the pressure anisotropy is generated by enhancement of magnetic field, one can assume that the generation of pressure anisotropy takes place in a Keplerian time scale. At the same time, isotropization of the plasma takes place within the space/time scale of ion kinetics, such as ion cyclotron frequency, and ion inertia length. As far as we know, there are no reliable estimation of the magnetic field strength in the accretion disk in Sgr A\*. Comparing the Keplerian time scale, and the cyclotron frequency calculated, for example with the parameter of interstellar field, the Keplerian time scale is longer than the cyclotron time scale with at least four orders of magnitude. In realistic disks, these two competing process, generation of pressure anisotropy due to the MRI, and relaxation of anisotropy via kinetic instabilities of ions take place at the same time. If some fraction of the pressure anisotropy remains in the saturated state of the disk turbulence, it would modify the feature of the disk turbulence, such as the efficiency of the angular momentum transport  $\alpha$ . It is reported from the collisionless MHD simulation that the pressure anisotropy remained in the disk turbulence provides additional stress component which contributes to a transport of angular momentum (Sharma et al. [2006]). The fraction of this “Anisotropic Stress” depends on the rate of pitch angle scattering provided by the kinetic plasma instability. Since these results were obtained from the collisionless MHD simulation, the rate of the pitch angle scattering cannot be evaluated with a self-consistent manner. In addition, generation of non-thermal particles which is expected in the collisionless turbulence cannot be treated in the hydrodynamical framework. To evaluate  $\alpha$  in the collisionless system and to evaluate the generation rate of non-thermal particles, long term simulation of the disk with particle based method would provide a self-consistent picture. In this sense hybrid code would be a realistic choice, since this code is free from the electron scale physics and can treat ion kinetics self-consistently. Up to date, there are no numerical studies calculating the non-linear evolution of MRI using a hybrid code. This is probably due to the unstable feature of the hybrid code. Therefore, we first aim to establish a robust approach to carry out a

simulation of MRI keeping the advantage of hybrid code. As a first step, we start from investigating an evolution of 2.5D MRI. Under the limitation due to the 2.5 dimension, we aim to evaluate the accretion properties in collisionless MRI.

Though hybrid code would provide a more robust approach compared to PIC simulation, we still have a limitation in attainable space/time scale compared to a realistic disk. In our MRI simulation, cyclotron frequency to Kepler frequency ratio is of the order of 10. The attainable spacial scale of the calculation is several hundreds times of the ion inertia length. Using  $\sim 100 \text{ cm}^{-3}$  for ion number density, the actual ion inertia scale is estimated as  $\sim 10^6 \text{ cm}$ . On the other hand Schwarzschild radius ( $2GM/c^2$ ) which gives the lower limit of the thickness of the disk is approximately  $10^{11} \text{ cm}$  for  $M \sim 10^6 M_\odot$ . Accepting these limitation, we aim to study the basic process of collisionless MRI.

Our next purpose is to investigate the evolution of magnetic reconnection in the differentially rotating system. The dissipation process by the magnetic reconnection is important for the determination of the saturation stage. With the hybrid simulation under the several magnetic field configuration, we aim to investigate the modification by the differential rotation on the evolution of magnetic reconnection. We also aim here to establish the boundary condition which appropriately treats the background shear motion. There are few applications of this boundary condition on the particle based simulation code, however, there are no reports applied in the hybrid code calculating the gravitationally supported differential rotation.

Finally we aim to discuss the implication how the modification of the magnetic reconnection due to the differential rotation acts on the macroscopic evolution of turbulence.

## 1.7.2 Structure of this Thesis

This thesis has 5 chapters. Here in the first chapter, we gave a general introduction of this thesis, introducing the accretion disks and plasma activities which are expected to exist in the disks.

In Chapter 2, we introduce a basis of hybrid code in the local corotating frame of a differentially rotating disk. The calculations in this chapter are carried on the meridional plane of the disk. As introduced in this chapter, there are some essential difficulties for the numerical simulation of MRI with a hybrid code. We introduce a new stabilizing technique in this chapter and discuss a non-linear state of 2.5D collisionless MRI.

In Chapter 3 and 4 we introduce evolution of magnetic reconnection in the accretion disk. Both chapters focus on the specific configuration of magnetic reconnection which would exist in the turbulence driven by MRI and discuss the effect of differential rotation on the evolution of magnetic reconnection. In Chapter 3 the evolution of the magnetic reconnection is investigated on the meridional plane of the disk, where the initial direction of the magnetic field is aligned to the axis of rotation. Main results introduced in this chapter are reported in Shirakawa and Hoshino [2014]. In Chapter 4 we introduce the evolution of magnetic reconnection on the equatorial plane of the disk where the initial magnetic field is aligned to the direction of the Keplerian shear flow. As we consider the local behaviour of a differentially rotating disk, we must take care of the boundary condition when we carry the calculation in the equatorial plane. We also introduce an implementation of this boundary condition in this chapter.

Finally in Chapter 5 we summarize the thesis and discuss about the future extension of our study.

## Chapter 2

# Magnetorotational Instability in collisionless accretion disks

In this chapter we introduce a non-linear evolution of 2.5 dimensional magnetorotational instability in collisionless accretion disks. To take the generation and relaxation processes of pressure anisotropy into account with a self-consistent manner, the calculation is based on hybrid equations. In addition, to carry out the calculation in the Keplerian rotational system Coriolis and tidal forces are taken into account. Fundamental equations and numerical codes are basically the same with those used in Shirakawa and Hoshino [2014], except for the correction due to the finite electron mass technique proposed by Amano et al. [2014]. Here a finite electron mass was included to deal with numerical difficulties with which the hybrid code often encounters.

With this new hybrid code, we first carried out a test calculation of “semi-1D” evolution of MRI by setting a thin simulation domain along the axial direction. As introduced in Section 2.2.2, our code takes the electron mass into account for the stable calculation. We have carried out test runs with varying mass ratio  $m_i/m_e$  where  $m_i$  and  $m_e$  are the ion and electron mass, respectively. Our new code gave a good agreement with the linear analysis as long as the ratio  $m_i/m_e$  was kept

sufficiently large. Confirming the validity of our new code we have carried out the calculation of MRI evolution on the meridional plane of the disk. From the 2.5D runs we obtained a growth of channel flows as reported in the MHD and PIC simulations. Unlike the MHD result, we obtained the corruption of the channel flow due to the magnetic reconnection.

This corruption of the channel flow is understood as the enhanced growth of magnetic reconnection due to the perpendicular pressure anisotropy generated by the non-linear growth of MRI. The result showed a good agreement with the previous study carried out with PIC calculation with pair-plasma (Hoshino [2013]). We consider our result is the first one to calculate non-linear evolution of MRI with hybrid code and will be an important step for the further investigation of long-term evolution of collisionless accretion disks in 3D systems.

## 2.1 Introduction

Magnetorotational instability (MRI) has been studied by numerous researchers for decades as an effective generator of turbulence in accretion disks. One of the fundamental problems in the accretion disk studies is about the effective process of transporting angular momentum of the gas constituting the disk. As proposed in Shakura and Sunyaev [1973], turbulence driven in the disk provides a strong turbulent viscosity and contributes to an effective transport of the angular momentum. It was shown that MRI (Velikhov [1959]; Chandrasekhar [1960]) which is driven by a strong dynamo effect by a shear flow provided by the differential rotation of the disk, can effectively generate turbulence in the disk (Balbus and Hawley [1991]; Hawley and Balbus [1991]). Since the turbulence in the disk determines the efficiency of the angular momentum transport, saturation of the MRI has been one of the most important problems. In the saturated, quasi steady state, the dynamo effect of the MRI and some sort of magnetic dissipation must be balanced (Balbus and Hawley [1998]). Numerous simulation studies have been

reported by many researchers to study the behavior of a quasi steady state of the MRI induced turbulence (Hawley and Balbus [1991]; Hawley and Balbus [1992]; Matsumoto and Tajima [1995]; Sano and Stone [2002b]). During the turbulent state of those calculations, rapid amplification and dissipation of magnetic energy have been observed implying magnetic reconnection is playing an important role on the dissipation of magnetic energy.

Until now, behavior of the plasma in accretion disks is mainly studied based on a conventional MHD approximation. However, in some classes of accretion disks a mean free path of the plasma is estimated to be comparable to or larger than the scale of the disk thickness. For example, several observations suggest that in the accretion disk around Sgr A\* at the center of our galaxy ions and electrons are not in the thermal equilibrium and ions are estimated to be much hotter than the electrons (Narayan et al. [1995]). This implies that there is no relaxation process between ions and electrons through collisions and thus the disk is considered to be collisionless. In such a disk, kinetic effect of the plasma will be important since pressure anisotropy generated by stretching the magnetic field modifies a feature of magnetic tension.

Motivated by these considerations, several attempts to understand both linear and non-linear evolution of collisionless MRI have been made. Quataert et al. [2002] have studied a linear behavior of MRI under CGL approximation (Chew et al. [1956]; Kulsrud [1983]) together with parallel heat flux due to the Landau damping incorporated via the so-called Landau closure (Snyder et al. [1997]). They have shown that the pressure anisotropy modifies the linear behavior of the MRI and have suggested that the kinetic plasma effect would also be important in the non-linear evolution of MRI. Sharma et al. [2006] have extended this study to a non-linear regime by using a so-called collisionless MHD code. Based on the linear analysis, they have applied the CGL approximation together with the Landau closure for calculating the temporal evolution of the parallel and perpendicular pressure with respect to the local magnetic field. In addition, they have assumed

that the upper and lower limits of the pressure anisotropy are determined by the criteria estimated from the kinetic instabilities which are driven by the pressure anisotropy, such as firehose, mirror and ion cyclotron instabilities. These instabilities would cause pitch angle scattering of the ions and lead to a relaxation of the generated pressure anisotropy. They have found that with the equation of state based only on the standard CGL approximation, enhancement of the magnetic field generates the perpendicular pressure anisotropy and have obtained a remarkably low saturation level of the MRI. The result was well understood as a suppression of the MRI by the generated perpendicular pressure anisotropy, because the perpendicular pressure anisotropy effectively enhances the magnetic tension which acts as the restoring force in the evolution of the MRI. With the parallel heat flux and the appropriate pitch angle scattering model, they confirmed the non-linear evolution of the MRI and pointed out that the rate of the angular momentum transport is enhanced moderately.

Numerical simulations of MRI capturing full kinetic effects in a self-consistent manner have been performed by Riquelme et al. [2012] and Hoshino [2013] by using a 2.5D PIC code which treats both the ions (the positrons, in Hoshino [2013]) and the electrons as superparticles. Riquelme et al. [2012] have shown that during the evolution of the kinetic MRI, the pressure anisotropy has been indeed, relaxed by the mirror mode and have confirmed basic features in the non-linear stage of the MRI reported in Sharma et al. [2006]. They have also found that the channel flow and the current sheet which are usually found in the final state of the 2.5D MHD simulations were corrupted due to a magnetic reconnection. Hoshino [2013] has extended the study to a relatively high beta ( $\beta \simeq 90-6000$ ) pair plasma and found the corruption of channel flow as well. Moreover they found that during the “active” phase when the magnetic reconnection takes place repeatedly and the channel flow is corrupted, the Maxwell stress is greatly enhanced. In both simulations particle acceleration associated with the magnetic reconnection has also been observed.

For an investigation of kinetic effect of the plasma, PIC simulation gives a self-consistent picture. However the attainable scale of the method is roughly limited in a several hundred times of the Debye length which is far smaller than that of the actual disk. In addition, as full particle codes must resolve a time scale related to the electron physics they require a massive integration time if one tries to focus both on the Keplerian time scale and on the electron time scale. Moreover, under a “first order” approximation kinetic effect of the ions should be more important than that of the electrons since it is often found in a collisionless accretion disk, the thermal energy of the ions dominates that of the electrons. In this point of view, hybrid code which treats the ions as particles and the electrons as massless fluid would provide a more robust approach rather than a full particle method since in this code the attainable scale of space and time is limited with ion inertia length and ion cyclotron frequency, respectively.

However, despite the successes in the PIC simulations, heavily non-linear simulation of MRI using a hybrid code has not been reported until now probably due to the numerically unstable feature of a hybrid code. Inclusion of differential rotation in the hybrid code was recently reported by Kunz et al. [2014b], and the evolution of MRI was also introduced. In their work, the linear regime of the instability was introduced, and accompanied generation of the pressure anisotropy was pointed out. However, further evolution of MRI, such as expected corruption of channel flow, has not been studied. The main purpose of this chapter is to investigate the non-linear stage of MRI using the hybrid code. Especially we aim to calculate the non-linear evolution of 2.5D MRI, and discuss which stress component would be the most effective on the angular momentum transportation. We also investigate whether the acceleration of the ions and generation of the non-thermal component would take place.

In this chapter we introduce a basic set of hybrid code equations in the differential rotating system. To deal with numerical difficulties of the hybrid code, we have implemented the finite electron inertia technique reported recently in Amano et al.

[2014]. We first introduce this method and extend to a differentially rotating system. Using this new method we confirmed a linear growth of MRI before going on to the 2.5D simulations and obtained the results consistent with those from the linear analysis. We also investigated non-linear evolution of MRI in the meridional plane of the disk. In the non-linear regime, we observed a corruption of the channel flow which is in good agreement with the results reported in the PIC studies.

## 2.2 Basic Equations and Setups

Our new code is based on a standard hybrid code, whose basics are introduced in Chapter 1,

$$\frac{d\mathbf{x}_i}{dt} = \mathbf{v}_i \quad (2.1)$$

$$m_i \frac{d\mathbf{v}_i}{dt} = q_i \mathbf{E} + q_i \frac{\mathbf{v}_i}{c} \times \mathbf{B} \quad (2.2)$$

$$\frac{\partial \mathbf{B}}{\partial t} = -c \nabla \times \mathbf{E}. \quad (2.3)$$

$$\mathbf{E} = -\frac{1}{c} \mathbf{V}_e \times \mathbf{B} + \frac{\nabla P_e}{n_e q_e} + \eta \mathbf{J} \quad (2.4)$$

$$\mathbf{J} = \mathbf{J}_e + \mathbf{J}_i = \frac{c}{4\pi} \nabla \times \mathbf{B} \quad (2.5)$$

$$\nabla \cdot \mathbf{B} = 0 \quad (2.6)$$

$$P_e \propto n_e^\gamma, \quad (2.7)$$

where  $\eta$  is the resistivity, and other characters have the same meaning introduced in Chapter 1. The model of  $\eta$  depends on the particular problems and will be discussed in each setup of the problem. In this chapter, we first introduce a set of hybrid equations in the local corotating frame of the disk. Here we focus on the localized region of the disk which is sufficiently far from the central star. Like in the linear analysis we introduced in Chapter 1, we would expect that any scale of spacial gradient of the perturbations are much smaller than the distance from the

central star in this localized region, namely,

$$|kR| \gg 1, \quad (2.8)$$

where  $k$  is the wavenumber of the perturbation and  $R$  is the distance from the central star. By adopting so-called “local approximation” (Balbus and Hawley [1991]), we can neglect the curvature of the cylindrical coordinate and can set a local Cartesian coordinate. In this Cartesian coordinate  $(x, y, z)$ ,  $x$  corresponds to the radial direction,  $y$  corresponds to the azimuthal direction and  $z$  corresponds to the axial direction. In the following we will express all the equations in the Cartesian representation without notice.

### 2.2.1 Effect of the Keplerian rotation

In this section, we introduce a method to include the effect of differential rotation in the hybrid code. In the corotating frame, one observes Coriolis force, centrifugal force, and gravity. The equation of motion of the ions (2.2) is then modified as

$$m_i \frac{d\mathbf{v}_i}{dt} = q_i \left( \mathbf{E} + \frac{1}{c} \mathbf{v}_i \times \mathbf{B} \right) - 2m_i \boldsymbol{\Omega}_0 \times \mathbf{v}_i + m_i r_i \Omega_0^2 \mathbf{e}_x - m_i g(r_i) \mathbf{e}_x, \quad (2.9)$$

where  $\Omega_0$  is the Keplerian frequency at the center of the simulation domain, and  $g(r_i)$  is the gravity from the central star with the distance of  $r_i$  and  $\mathbf{e}_x$  is the  $x$ -component unit vector. The third, fourth, and the fifth term in the right hand side of Equation (2.9) corresponds to Coriolis force, centrifugal force, and the gravity from the central star, respectively. Throughout this thesis the vertical component ( $z$ -direction) of the gravity is ignored, and in the background rotation, balance between the gravity and the centrifugal force,  $m_i g(r_i) = m_i r_i \Omega_0^2$  is satisfied. Note that the Ohm’s law, which is derived from the equation of motion of the electron would not be modified by the Coriolis force and gravity, since these forces are proportional to mass and in the hybrid framework,  $m_e \rightarrow 0$  is assumed. In this

chapter we investigate evolution of the system in the meridional plane  $(x, z)$ , of the accretion disk. Since we focus on the localized region of the accretion disk, we can approximate the background differential rotation with a linear profile. Introducing the following transformation,

$$x = r_i - r_0, \quad (2.10)$$

$$z = z, \quad (2.11)$$

and applying the tidal expansion on the Hill coordinate (Hill [1878]), the equation of motion (2.9) becomes,

$$m_i \frac{d\mathbf{v}_i}{dt} = q_i \left( \mathbf{E} + \frac{1}{c} \mathbf{v}_i \times \mathbf{B} \right) - 2m_i \Omega_0 \times \mathbf{v}_i - 2m_i q \Omega_0^2 x \mathbf{e}_x. \quad (2.12)$$

Here  $r_0$  is the center of the simulation domain. The rate of the shear is defined with  $q = \partial \log \Omega / \partial \log r|_{r=r_0}$ , and for a Keplerian rotation ( $\Omega \propto r^{-3/2}$ )  $q$  is equal to  $-3/2$ . Under this approximation, we can write the background Keplerian velocity with a linear profile in the corotating frame;

$$\mathbf{v}_K = q \Omega_0 x \mathbf{e}_y, \quad (2.13)$$

where  $\mathbf{e}_y$  is the unit vector of  $y$ -component. Because of this background flow, non-zero electric field  $\mathbf{E}_K = -\mathbf{v}_K \times \mathbf{B} / c$  is always observed in the corotating frame. Since this electric field is a function of  $x$ , charge neutrality is not exactly satisfied in this system. The magnitude of the charge inequality is estimated as,

$$\begin{aligned} \frac{\nabla \cdot \mathbf{E}_K}{4\pi n_{i0} q_i} &= -\frac{1}{4\pi n_{i0} q_i c} q \Omega_0 B - \frac{1}{4\pi n_{i0} q_i c} q \Omega_0 B \left. \frac{\partial \log B}{\partial \log x} \right|_{x=0} \\ &= -\frac{V_A^2}{c^2} \frac{\Omega_0}{\Omega_{ci}} \left( 1 + \left. \frac{\partial \log B}{\partial \log x} \right|_{x=0} \right), \end{aligned} \quad (2.14)$$

where  $\Omega_{ci} = q_i B / m_i c$  is the cyclotron frequency of the ions. In an usual accretion disk,  $\Omega_0 / \Omega_{ci} \ll 1$  holds and also under the hybrid framework  $V_A / c \rightarrow 0$  is

assumed. Therefore the inequality of the charge due to the differential rotation can be neglected in the hybrid framework. For the integration of Equation (2.12) we use the ordinary Buneman-Boris method with transformed electric/magnetic field,

$$\mathbf{E}^* = \mathbf{E} - 2 \frac{m_i}{q_i} q \Omega_0^2 x \mathbf{e}_x, \quad (2.15)$$

$$\mathbf{B}^* = \mathbf{B} + 2 \frac{m_i c}{q_i} \Omega_0. \quad (2.16)$$

For update of  $\mathbf{E}$  and  $\mathbf{B}$  we adopt the iterative method proposed by Horowitz et al. [1989].

## 2.2.2 Finite electron mass

In this section we introduce a stabilization method of hybrid code by introducing a finite electron mass, based on Amano et al. [2014]. We first explain fundamental difficulties which we encounter in the hybrid simulation of MRI. Let us start from the consideration of Hall MHD equations.

In the hybrid framework, ions are no longer frozen-in to the magnetic field in the small scale, and the dispersion relation of linear waves calculated with this framework is well approximated with those obtained from the linear analysis of Hall MHD equations.

$$\frac{\partial n_i}{\partial t} + \nabla \cdot (n_i \mathbf{V}_i) = 0 \quad (2.17)$$

$$n_e \simeq n_i \quad (2.18)$$

$$q_i = -q_e \quad (2.19)$$

$$m_i n_i \left( \frac{\partial \mathbf{V}_i}{\partial t} + \mathbf{V}_i \cdot \nabla \mathbf{V}_i \right) = \frac{1}{c} \mathbf{J} \times \mathbf{B} \quad (2.20)$$

$$\mathbf{J} = n_e q_e \mathbf{V}_e + n_i q_i \mathbf{V}_i = \frac{c}{4\pi} \nabla \times \mathbf{B} \quad (2.21)$$

$$\frac{\partial \mathbf{B}}{\partial t} = -c \nabla \times \mathbf{E} \quad (2.22)$$

$$\mathbf{E} = -\frac{1}{c} \mathbf{V}_e \times \mathbf{B} \quad (2.23)$$

$$\mathbf{V}_e = \mathbf{V}_i + \frac{c}{4\pi n_e q_e} \nabla \times \mathbf{B} \quad (2.24)$$

where  $\mathbf{V}_i$  is the ion bulk velocity, and we have assumed cold plasma for simplicity. Applying Fourier transformation to the linearized set of Equations (2.17)-(2.24), we obtain the following dispersion relation,

$$\frac{\omega^2}{k^2 V_A^2} = 1 \pm \frac{\omega}{\Omega_{ci}}, \quad (2.25)$$

where  $\omega$  is the frequency. In Figure 2.1, we show the  $k$ - $\omega$  diagram of the given dispersion. Blue dashed lines corresponds to the wave mode obtained from the Hall MHD equations. As seen from the plot, the phase velocity of the R-Mode (Whistler) wave significantly increases in the shorter wavelength though it asymptotically reaches to that of shear Alfvén wave (black dashed line) in the larger (MHD) scale. For the mode  $\omega \gg \Omega_{ci}$ , R-Mode wave has the  $k^2$  dependency without an upper limit of phase velocity and gives a severe CFL (Courant-Friedrichs-Lewy) condition.

Another problem is related to the extremely low density region which is created in the non-linear stage of the MRI evolution (see Figure 2.3.). During the growth of MRI, total pressure balance is satisfied and in the region where magnetic field is amplified, the density of the ions becomes very low, giving even high phase velocity of shear Alfvén wave compared to the initial condition. In this region, phase velocity of the R-Mode is even higher in the ion inertia scale, and if one tries to keep  $\Delta t$  in the realistic value for the integration, the CFL condition given by the R-mode is disturbed and the calculation encounters an unexpected termination. One solution for this problem is to give upper limit to the R-mode phase velocity with appropriate manner. This can be done by introducing a finite electron mass, modifying the dispersion relation (2.25) to those obtained from the 2-fluid equations (Kuznetsova et al. [1998]). The red solid lines in Figure 2.1 shows a dispersion relation obtained from the two-fluid equation with the mass ratio of  $m_i/m_e = 25$ . As expected, the phase velocity of the R-Mode wave is reduced

in the small scale, and reaches to electron cyclotron frequency. Note that in the calculation of MRI, we are interested in the larger scale ( $k\lambda_i \lesssim 1$ ) and in this scale there are no significant difference between the Hall MHD results and two fluid results.

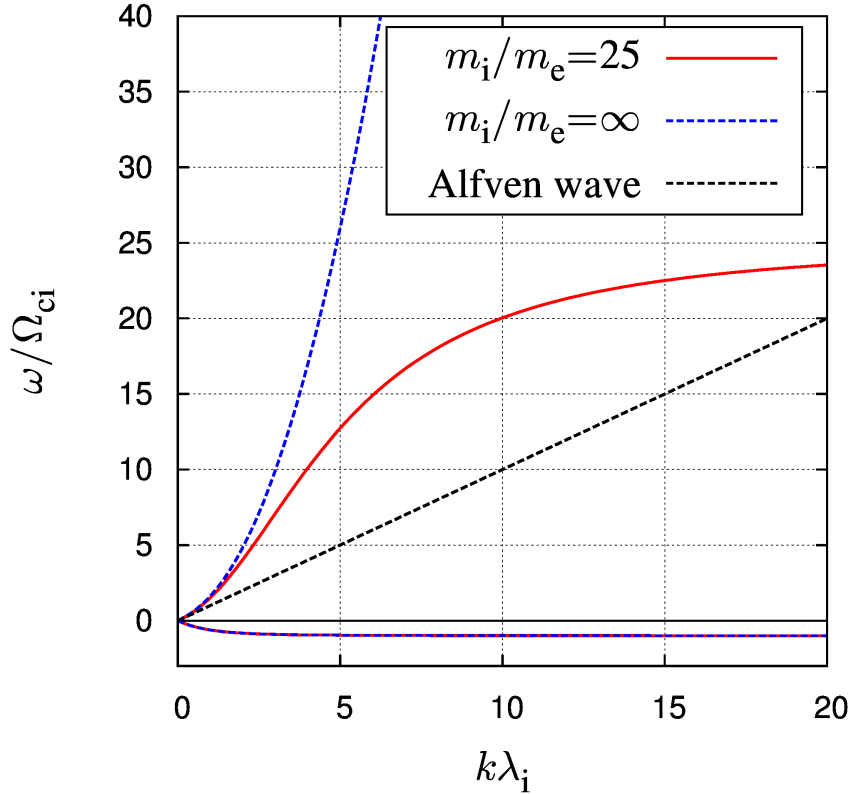


FIGURE 2.1: Dispersion relation of transverse mode of linear waves. The dashed blue lines show a dispersion obtained from Hall MHD equations, whereas the red solid lines show the one obtained from the two fluid equations with mass ratio of  $m_i/m_e = 25$ . Dashed black lines corresponds to ordinary shear Alfvén wave to which the Hall (Blue) and the two fluid (Red) results asymptotically reach in the MHD limit ( $k, \omega \rightarrow 0$ ).

The second difficulty comes from the “division-by-density” operation which is always required in the conventional hybrid simulation when one calculates electric field via Ohm’s law (2.24). Here the low density region generated by MRI gives another numerical problem since one must divide finite value with nearly zero density.

To include the finite electron inertia effect, and to deal with division-by-density problem, Amano et al. [2014] proposed a new approach for the calculation of the

electric field solving the following elliptic equations,

$$\begin{aligned} \frac{1}{4\pi} (\omega_{\text{pe}}^2 - c^2 \nabla^2) \mathbf{E} &= -\frac{q_e}{m_e} \frac{\mathbf{J}_e}{c} \times \mathbf{B} + q_e n_e \nabla \cdot (\mathbf{V}_e \otimes \mathbf{V}_e) \\ &= \frac{\omega_{\text{pe}}^2}{4\pi} \hat{\mathbf{E}}. \end{aligned} \quad (2.26)$$

Here,  $\hat{\mathbf{E}}$  is the electric field derived from the conventional method of hybrid simulation. The details about the derivation is introduced in Appendix A. Note that the density is multiplied in the right hand side of Equation (2.26). One must yet apply density division for the advection term ( $\propto \mathbf{V}_e \otimes \mathbf{V}_e$ ), but this term is important only in the case when the electron bulk velocity reaches the electron Alfvén velocity, and thus this term in general gives a minor correction. Therefore in this new approach, the set of the equations are “almost” free from the division-by-density operation.

The method showed robustness in the 1 dimensional test problems which are reported in Amano et al. [2014]. In this thesis, we extended the method to 2.5 dimensional code, and added the effect of Kepler rotation.

To summarize, the set of the equation we solve in the calculation is described as follows,

$$\frac{d\mathbf{x}_i}{dt} = \mathbf{v}_i \quad (2.27)$$

$$q_i = -q_e \quad (2.28)$$

$$n_i = \sum_{\text{particle}} S(\mathbf{x}_i). \quad (2.29)$$

$$n_e \simeq n_i \quad (2.30)$$

$$\mathbf{J}_i = q_i \sum_{\text{particle}} \mathbf{v}_i S(\mathbf{x}_i). \quad (2.31)$$

$$m_i \frac{d\mathbf{v}_i}{dt} = q_i \left( \mathbf{E} + \frac{1}{c} \mathbf{v}_i \times \mathbf{B} \right) - 2m_i \boldsymbol{\Omega}_0 \times \mathbf{v}_i - 2m_i q \Omega_0^2 x e_x \quad (2.32)$$

$$\frac{\partial \mathbf{B}}{\partial t} = -c \nabla \times \mathbf{E}. \quad (2.33)$$

$$\hat{\mathbf{E}} = -\frac{1}{c} \mathbf{V}_e \times \mathbf{B} + \frac{\nabla P_e}{n_e q_e} + \frac{m_e}{q_e} \nabla \cdot (\mathbf{V}_e \otimes \mathbf{V}_e) + \eta \mathbf{J} \quad (2.34)$$

$$\frac{\omega_{\text{pe}}^2}{4\pi} \hat{\mathbf{E}} = \frac{1}{4\pi} (\omega_{\text{pe}}^2 - c^2 \nabla^2) \mathbf{E} \quad (2.35)$$

$$\mathbf{J} = q_e n_e \mathbf{V}_e + \mathbf{J}_i = \frac{c}{4\pi} \nabla \times \mathbf{B} \quad (2.36)$$

$$\nabla \cdot \mathbf{B} = 0 \quad (2.37)$$

$$P_e \propto n_e^\gamma, \quad (2.38)$$

where  $S(\mathbf{x}_i)$  is an appropriate shape function used for moment calculation. Throughout this thesis, we adopt 2nd order shape function.  $\gamma$  is the adiabatic constant and throughout this thesis, we assume that electrons' equation of state is given by isotropic adiabatic equation ( $\gamma = 5/3$ ). In the integration of the above system with the difference scheme, we set staggered mesh and the Constrained-Transport (CT) method (Hawley and Stone [1995]) was applied to guarantee the solenoidal condition of the magnetic field.

### 2.2.3 Initial condition and Parameters

In this section we introduce parameters used in the initial conditions. As we investigate the 2.5 dimensional evolution in the meridional plane of the disk, the particles' position is described with 2 components ( $x, z$ ) whereas the particles' velocity is described with 3 components ( $v_x, v_y, v_z$ ).

As an initial state we assume a uniform distribution for plasma density. We impose ions as superparticles with a Maxwellian distribution with linearized Keplerian shear,

$$f_i(\mathbf{x}_i, \mathbf{v}_i) = n_i \left( \frac{m_i}{2\pi T_i} \right)^{3/2} \exp \left[ -\frac{m_i}{2T_i} (v_x^2 + (v_y - v_{\text{Ky}}(x))^2 + v_z^2) \right]. \quad (2.39)$$

Throughout this thesis, to avoid confusion with wavenumber  $k$ , and to avoid complexity, we include the Boltzmann constant ( $k_B$ ) in the definition of temperature.

The initial magnetic field is assumed to be parallel to the rotation axis,

$$\mathbf{B}_0 = B_0 \hat{\mathbf{e}}_z. \quad (2.40)$$

Figure 2.2 shows a schematic illustration of the runs calculated in this section. Using this conditions, we carry out two types of runs. Runs with symbol “T” correspond to the test runs to check the validity of our new code. In this series of

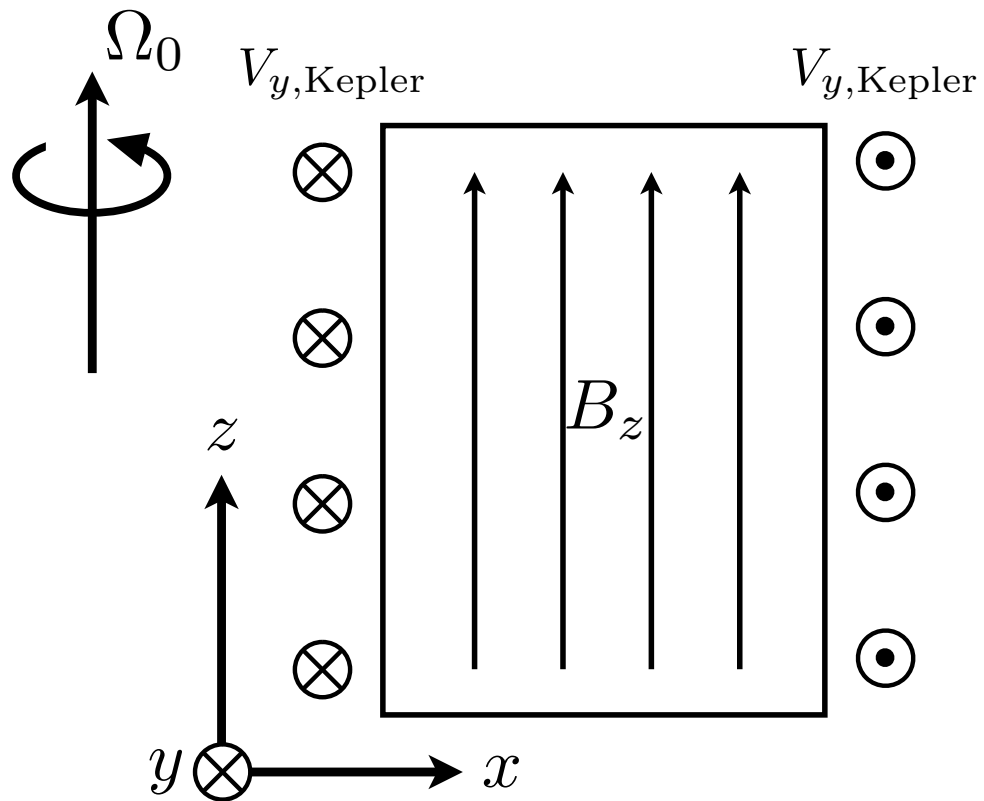


FIGURE 2.2: Schematic illustration of initial condition used in this chapter.

runs, we prepare thin simulation box with the size of  $L_x \times L_z = 33.33\lambda_i \times 270.8\lambda_i$  with the grid interval of  $\Delta x = \lambda_i/1.2$ , where  $\lambda_i$  is the ion inertia length. By setting “semi-1D” box, we compare our result to that of conventional MRI. In Table 2.1, we show several important parameters. In the table,  $N_x$  and  $N_z$  are the number of the  $x$  and  $z$  grid respectively, and  $N_{\text{ppc}}$  is the number of the particles we impose in each cell. In this thesis, we describe  $\Omega_0/\Omega_{\text{ci}}$  as “rotational parameter”. Note that

TABLE 2.1: Simulation Parameters for Test Runs.

	RUN T09	RUN T16	RUN T25
$N_x \times N_z$	$41 \times 326$	$41 \times 326$	$41 \times 326$
$N_{\text{ppc}}$	500	500	500
$\lambda_i$	$1.2\Delta x$	$1.2\Delta x$	$1.2\Delta x$
$\beta_i$	1.0	1.0	1.0
$P_e/P_i$	$5 \times 10^{-3}$	$5 \times 10^{-3}$	$5 \times 10^{-3}$
$\Omega_0/\Omega_{\text{ci}}$	0.1	0.1	0.1
$m_i/m_e$	9	16	25

this parameter is essentially the same with so-called ‘‘Hall parameter’’ introduced in Balbus and Terquem [2001] and our definition is by factor 2 smaller than the original one. Although actual accretion disks are considered to be constituted with high beta plasma ( $\beta_i \gg 1$ ) we choose  $\beta_i = 1.0$  in this test run. It is well known that the rich kinetic effects such as generation of the pressure anisotropy (Riquelme et al. [2012]; Hoshino [2013]) or finite Larmor radius effect (Ferraro [2007]) would modify linear growth of MRI. By imposing low  $\beta_i$  plasma, we have avoided these effects and set the condition close to the conventional MRI. In all runs vertical size of the box is set to the length so that the maximum growing wavelength would be  $0.5L_z$  and thus Mode 2 of the MRI would be the most unstable in the simulation domain.

In runs with symbol ‘‘B’’, we set a larger size of the simulation box ( $L_x \times L_z = 192\lambda_i \times 256\lambda_i$ ) with the same grid interval as the test runs. In this series of runs we aim to investigate the non-linear evolution of 2.5D MRI with varying initial  $\beta_i$ . Again, several important parameters are shown in Table 2.2.

TABLE 2.2: Simulation Parameters for varying beta runs.

	RUN B1	RUN B2	RUN B3
$N_x \times N_z$	$193 \times 257$	$193 \times 257$	$193 \times 257$
$N_{\text{ppc}}$	480	900	1200
$\lambda_i$	$1.2\Delta x$	$1.2\Delta x$	$1.2\Delta x$
$\beta_i$	33	99	333
$P_e/P_i$	$5 \times 10^{-3}$	$5 \times 10^{-3}$	$5 \times 10^{-3}$
$\Omega_0/\Omega_{\text{ci}}$	0.0667	0.0667	0.0667
$m_i/m_e$	16	16	16

## 2.3 Results

### 2.3.1 Semi 1-Dimension: Linear test

We first look at the result of semi-1D MRI test of our code. Figure 2.3 shows time evolution of RUN T16. As expected, Mode 2 of MRI grows and eventually two sets of channel flows are generated. We find extremely strong magnetic field outside the channel flow ( $B^2 \sim 10^4 B_0^2$ ). Since in the 1D configuration there is no effective process to dissipate the magnetic field energy, the exponential growth takes place continuously. As a result CFL condition obtained with the R-Mode wave in the outside of the channel flow region gets severer and severer, and as a consequence, the evolution of the system could no longer be calculated within reasonable time. Nevertheless the evolution during  $\Omega_0 t / 2\pi \simeq 1-2$  is well fitted with an exponential growth and we obtain growth rate of MRI from each run.

Figure 2.4 shows growth rates obtained from MRI simulation. The color of the circle corresponds to different runs. The solid line shows the linear growth rate of MRI obtained from linear analysis of MHD equations. Strictly speaking, as our code is based on hybrid framework, it is better to compare our results with those obtained from Hall MHD analysis (e.g., Balbus and Terquem [2001]; Sano and Stone [2002a]) but with the Hall parameter used in our code ( $|\Omega_0/\Omega_{\text{ci}}| \leq 0.1$ ) makes no significant difference between the linear MHD analysis. As we can see from the figure, the simulation result shows a good agreement with linear theory.

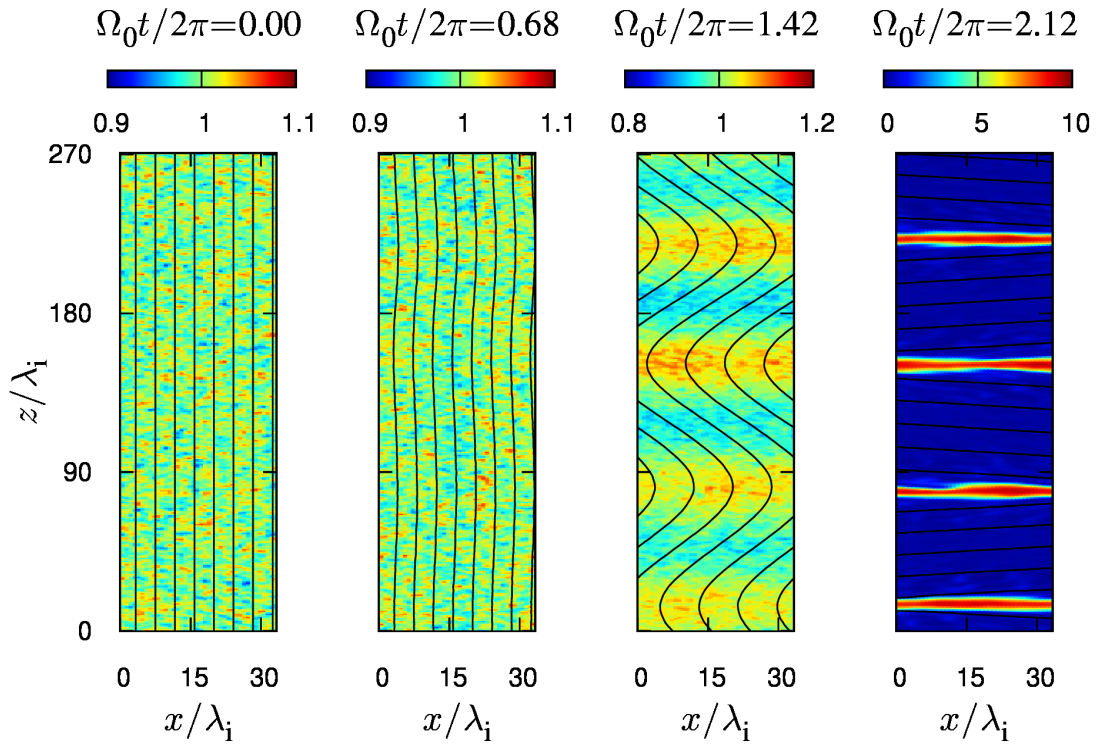


FIGURE 2.3: Time evolution of “semi-1D” MRI. Color corresponds to ion density whereas the solid lines corresponds to magnetic field line.

In addition, a different value of finite electron mass gives basically the same growth rate. We consider that these results guarantee validity of our new code.

### 2.3.2 Overview of 2.5 Dimensional RUNS ( $\beta_i = 99$ Case)

Now let us go on to the results of the 2.5D simulations. We first overview our results. Figure 2.5 shows the time evolution of RUN B2. The color contour corresponds to the ion density normalized by its initial value. The initial magnetic field imposed parallel to the rotational axis eventually grows to a set of channel flow and forms a set of current sheet. This result is often reported in 2.5D MHD simulations (e.g., Sano and Inutsuka [2001]). Figure 2.6 shows a time evolution of magnetic energy of each component. Due to the channel flow,  $B_x$  is first enhanced. However as time goes on,  $B_y$  is enhanced due to the Keplerian shear flow. Note that at the

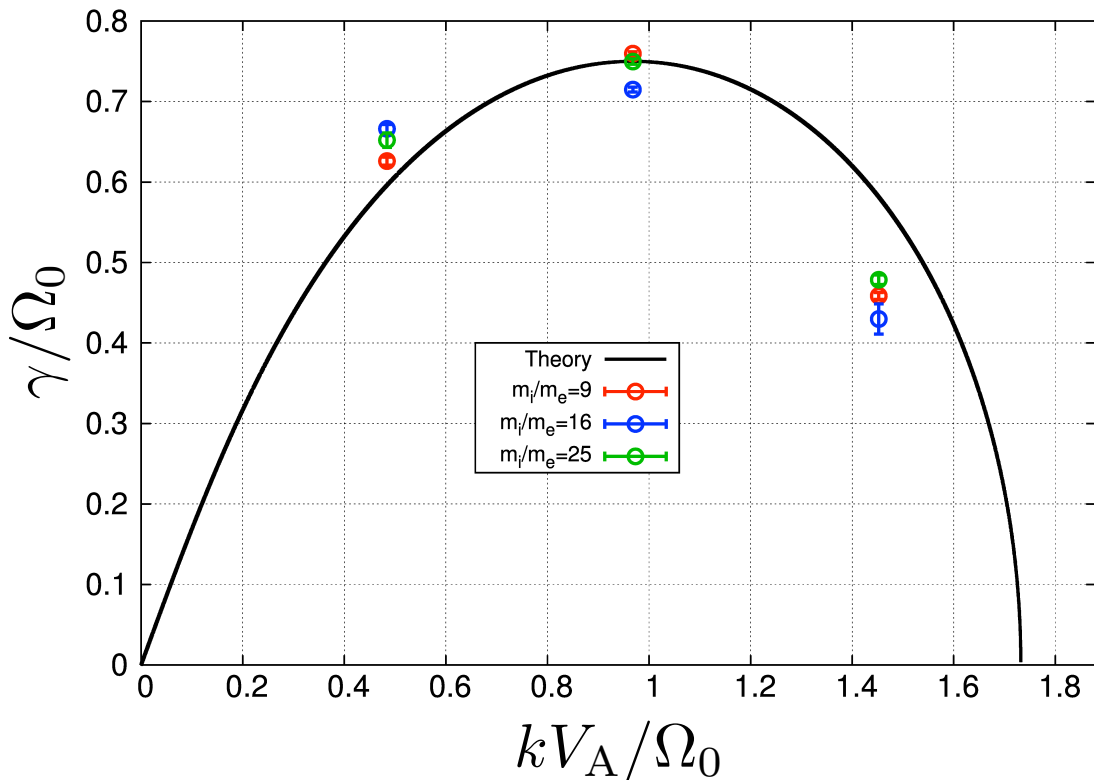


FIGURE 2.4: Growth rate of MRI obtained from linear analysis of MHD equations (Solid line) and from semi 1D run of hybrid simulations (Open circles).

non-linear regime of the simulation ( $\Omega_0 t/2\pi \gtrsim 5$ ), the total magnetic energy is enhanced by  $\sim 10^4$  times compared to its initial value. At this moment, the density outside the channel flow becomes remarkably low ( $\sim 0.2n_{\text{initial}}$ ). This condition yields phase velocity of the Alfvén wave 200 times faster than its initial value, and for the R-Mode wave at this moment, the phase velocity is even faster, giving extremely severe CFL condition. With a conventional hybrid simulation, such a system could not be calculated. By reducing the phase velocity of R-Mode wave with the finite electron mass, we have attained a further evolution of non-linear MRI. It should be noted that the shift of the most unstable wavelength to a longer scale which we introduced in Figure 1.5 is also found in our simulation. With the initial parameter we have adopted, the most unstable wavelength is approximately half the length of the vertical size of the simulation domain. Therefore, Mode 2 of MRI is expected if we assume an ideal growth of MRI. However during the linear

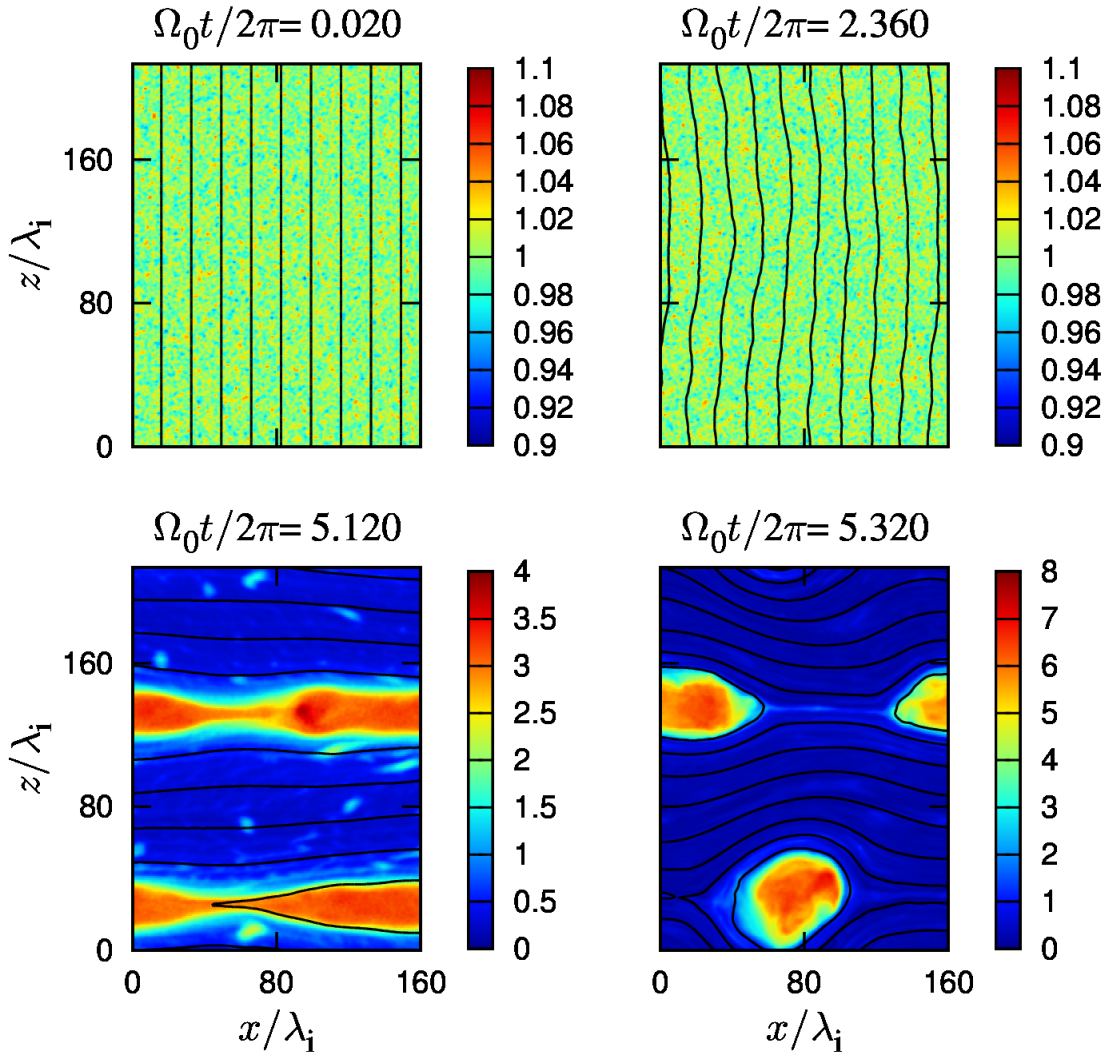


FIGURE 2.5: Time evolution of ion density (color) and magnetic field line (solid line). Initial plasma  $\beta_i$  was set to be 99.

growth of MRI, the perpendicular pressure dominates the parallel pressure as the magnetic field is enhanced, and as a result, the most unstable wavelength is shifted to larger scale. As a result, in the non-linear stage, we get Mode 1 of MRI growth and a set of channel flow.

In the non-linear state of MRI ( $\Omega_0 t / 2\pi \simeq 5.2$ ), magnetic reconnection takes place and magnetic islands are generated. However the magnetic energy was not sufficiently dissipated in our simulation and the saturation of the system was not observed. As a final state of the calculation, severe numerical noise was generated at the density depletion region near the separatrix of reconnection site and the calculation was terminated.

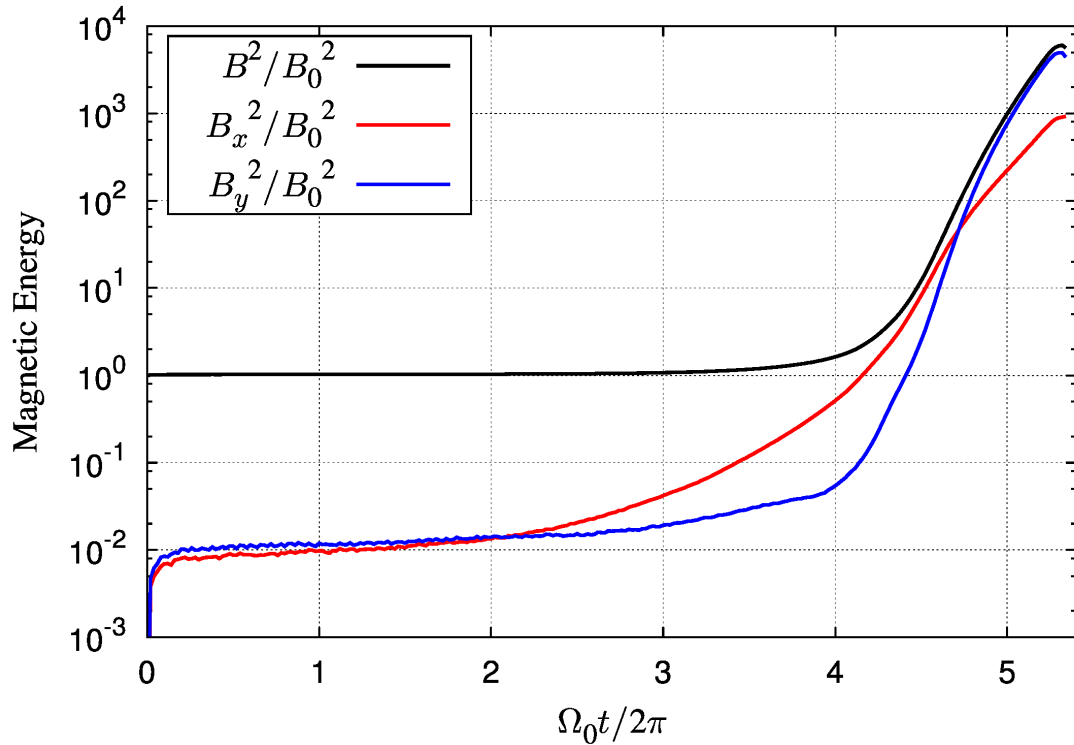


FIGURE 2.6: History of the magnetic energy averaged on the entire domain of the simulation.

### 2.3.3 Generation of perpendicular pressure anisotropy

To investigate the onset mechanism of the reconnection, we analyzed a pressure anisotropy profile at the onset of the reconnection. Figure 2.7 shows a profile of the pressure anisotropy along the  $z$ -direction at  $\Omega_0 t / 2\pi \simeq 5.12$ . The calculated parameter was well below the isotropic criteria “1”, in the entire region of the simulation domain, implying that at this moment, perpendicular pressure is dominant. This is consistent with the primary understanding that the conservation of 1st adiabatic invariant leads to the enhancement of the perpendicular pressure as the magnetic field is enhanced.

Note that the perpendicular pressure is also dominant in the channel flow region (=current sheet region). It is reported when perpendicular pressure dominates, collisionless tearing mode couples with mirror mode instability, and the growth rate of the tearing mode is enhanced (Chen et al. [1984]; Chen and Palmadesso [1984]). Resulting growth rate of tearing mode given by Chen and Palmadesso

[1984] is expressed as,

$$\begin{aligned}
\frac{\gamma}{kv_{\text{th},i}} &\simeq \frac{v_{\text{th},e}}{v_{\text{th},i}} \left(\frac{r_{\text{ge}}}{l}\right)^{3/2} \left(1 + \frac{p_{\perp,i}}{p_{\perp,e}}\right) \left(\frac{1 - k^2 l^2}{kl}\right) \\
&+ \left(\frac{p_{\perp,i}}{p_{\parallel,i}} - 1\right) \left(\frac{r_{\text{ge}}}{r_{\text{gi}}}\right)^{3/2} \sqrt{\frac{m_e T_e}{m_i T_i}} \\
&\simeq \left(\frac{r_{\text{ge}}}{l}\right)^{3/2} \left(\frac{1 - k^2 l^2}{kl}\right) \sqrt{\frac{m_i T_e}{m_e T_i}} \\
&+ \left(\frac{p_{\perp,i}}{p_{\parallel,i}} - 1\right) \left(\frac{r_{\text{ge}}}{r_{\text{gi}}}\right)^{3/2} \sqrt{\frac{m_e T_e}{m_i T_i}}, \tag{2.41}
\end{aligned}$$

where we have neglected some of the coefficients with the order of unity for simplicity. In Equation (2.41),  $v_{\text{th},j}$  stands for thermal velocity,  $r_{g,j}$  stands for gyro radius of component  $j$ , and  $l$  stands for the current sheet thickness. The estimation in first to second row holds since we assume  $T_i \gg T_e$ . The second term corresponds to the modification given by coupling with the mirror mode. In the isotropic limit ( $p_{\perp} = p_{\parallel}$ ), Equation (2.41) degenerates to the ordinary dispersion relation of collisionless tearing mode. Note that even we assume isotropic electron pressure, we have expressed as  $p_{\perp,e}$  to follow the original article. Comparing the magnitude of the first and second term in the right hand side, when the perpendicular pressure dominates the parallel pressure with the order of  $O((m_e/m_i)(l/r_{\text{gi}})^{3/2})$  the second term becomes dominant and the growth rate of the tearing mode is dramatically enhanced. This condition was also satisfied in our calculation and as a result magnetic reconnection in the channel flow was observed and magnetic islands are generated.

### 2.3.4 Evolution of stress components and $\alpha$

Though the system did not reach the saturation, the stress parameter ( $\alpha$ ) reached its temporal maximum, and we could evaluate  $\alpha$  in the hybrid framework. Here

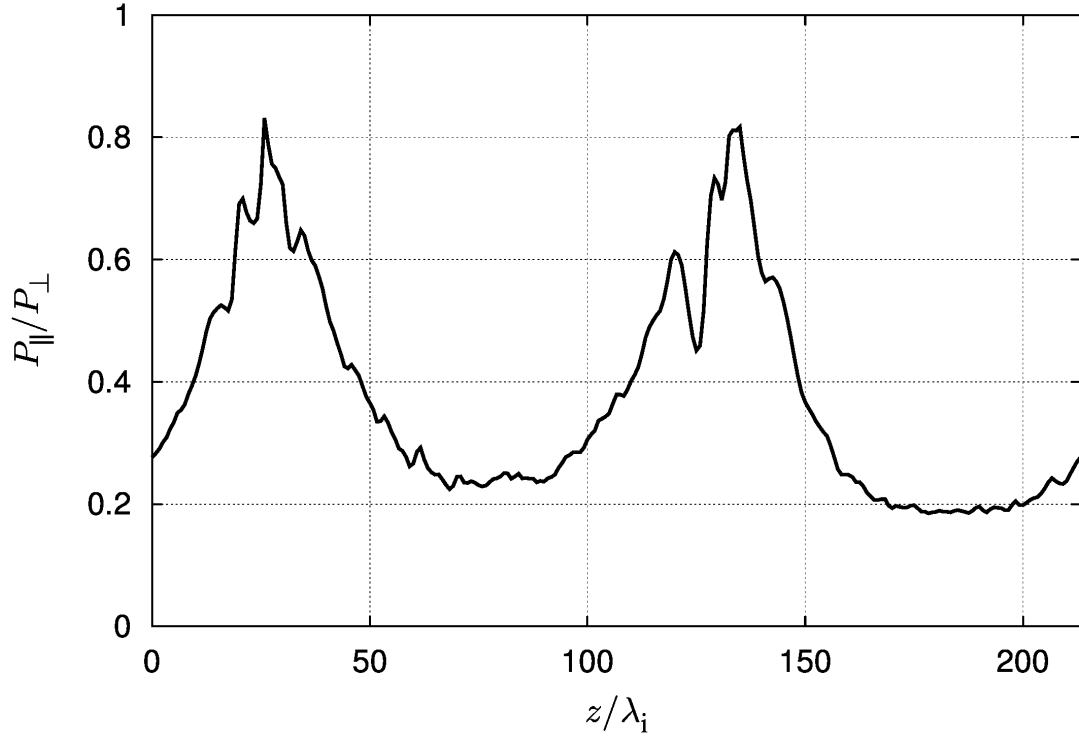


FIGURE 2.7: Averaged pressure anisotropy (solid line) at  $\Omega_0 t / 2\pi = 5.12$ . The initial  $\beta_i$  was set to be 99.

we defined  $\alpha$  by

$$\alpha = \frac{W_R + W_M + W_A}{\langle P \rangle} \quad (2.42)$$

where  $\langle P \rangle$  is the pressure averaged over the entire domain at each time step. Since the system did not reach to the saturation and the quasi steady state was not attained, we applied only spacial averaging rather to apply ensemble averaging.  $W_R, W_M, W_A$  are the Reynolds, Maxwell, and Anisotropic stress, respectively and defined as

$$W_R = \langle \rho V_{i,x} (V_{i,y} + q\Omega_0 x) \rangle \quad (2.43)$$

$$W_M = \left\langle \frac{B_x B_y}{4\pi} \right\rangle \quad (2.44)$$

$$W_A = \left\langle \frac{p_{\parallel,i} - p_{\perp,i}}{B^2} B_x B_y \right\rangle. \quad (2.45)$$

Figure 2.8 shows an evolution of each stress components and their sum. As shown in Figure 2.8, value of  $\alpha$  lies on  $\sim 0.1-1$  during the non-linear growth of MRI. Though our system is limited to 2.5D and one must care while comparing the results with those of the MRI simulations, value of  $\alpha$  is larger than the MHD results by magnitudes of 1-2. This evaluated value of  $\alpha$  is roughly consistent with the PIC results implying the efficient angular momentum transport in the collisionless system.

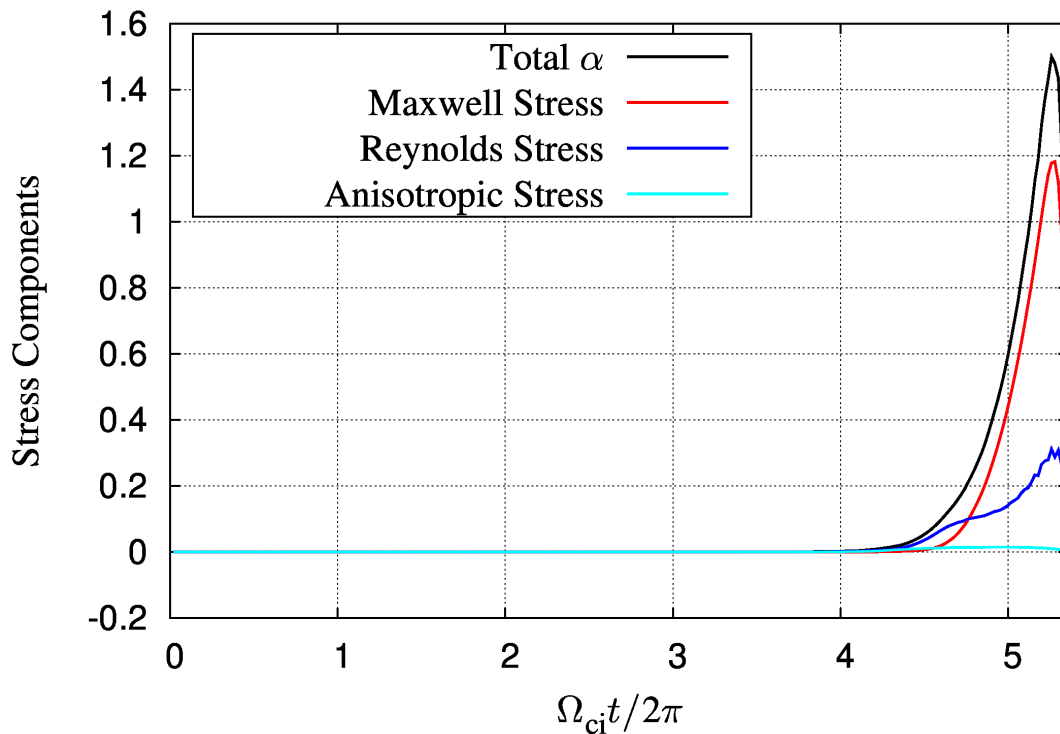


FIGURE 2.8: Time evolution of stress components.

### 2.3.5 Heating of the ions by magnetic reconnection

Accompanied with the growth of MRI and magnetic reconnection in the non-linear stage of the MRI, significant heating of the ions was observed. Figure 2.9 shows a time evolution of ions' energy spectra. The horizontal axis corresponds to particle energy in the unit of kinetic energy defined with the Alfvén speed in the initial condition ( $\varepsilon \equiv V^2/V_{A0}^2$ ), whereas the vertical axis corresponds to the number

density  $N(\varepsilon)d\varepsilon$ . It is clearly observed that the ions are heated after the onset of the magnetic reconnection  $\Omega_0 t/2\pi = 5.32$ . Moreover, non-thermal components of the ions starts to generate just after the onset of magnetic reconnection. This feature is basically the same with Hoshino [2013]. However, our simulation terminates at this point due to the generation of the density depletion region near the separatrix and therefore, the total flux of the non-thermal component and the power index could not be evaluated from the present calculation.

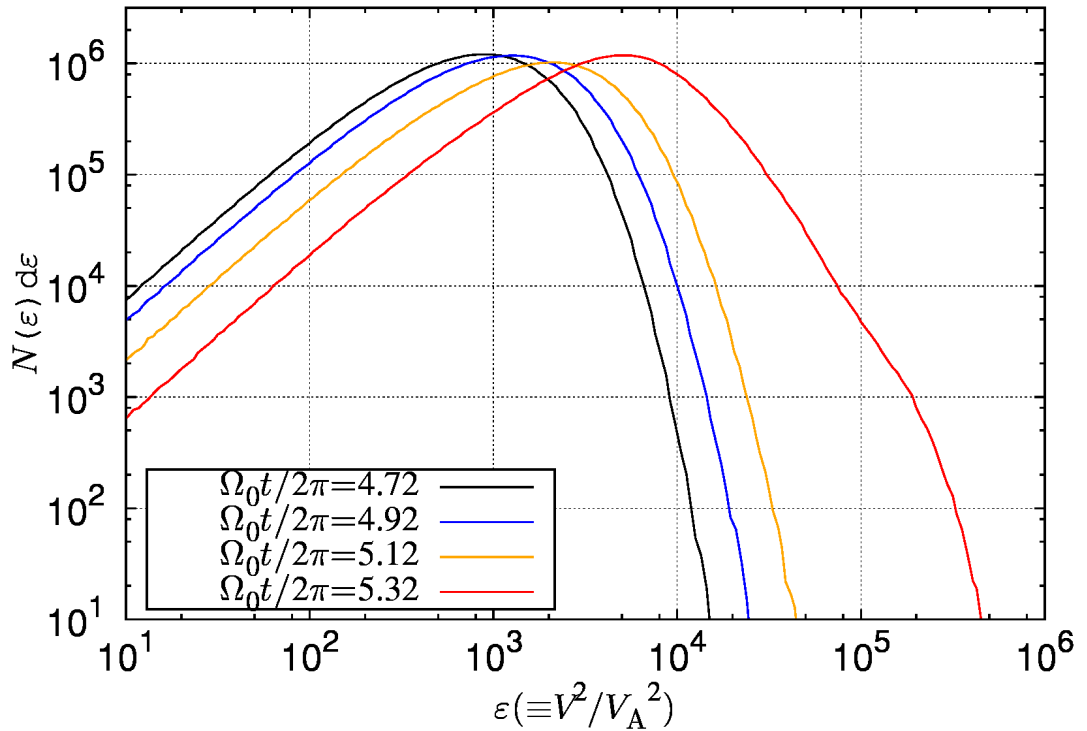
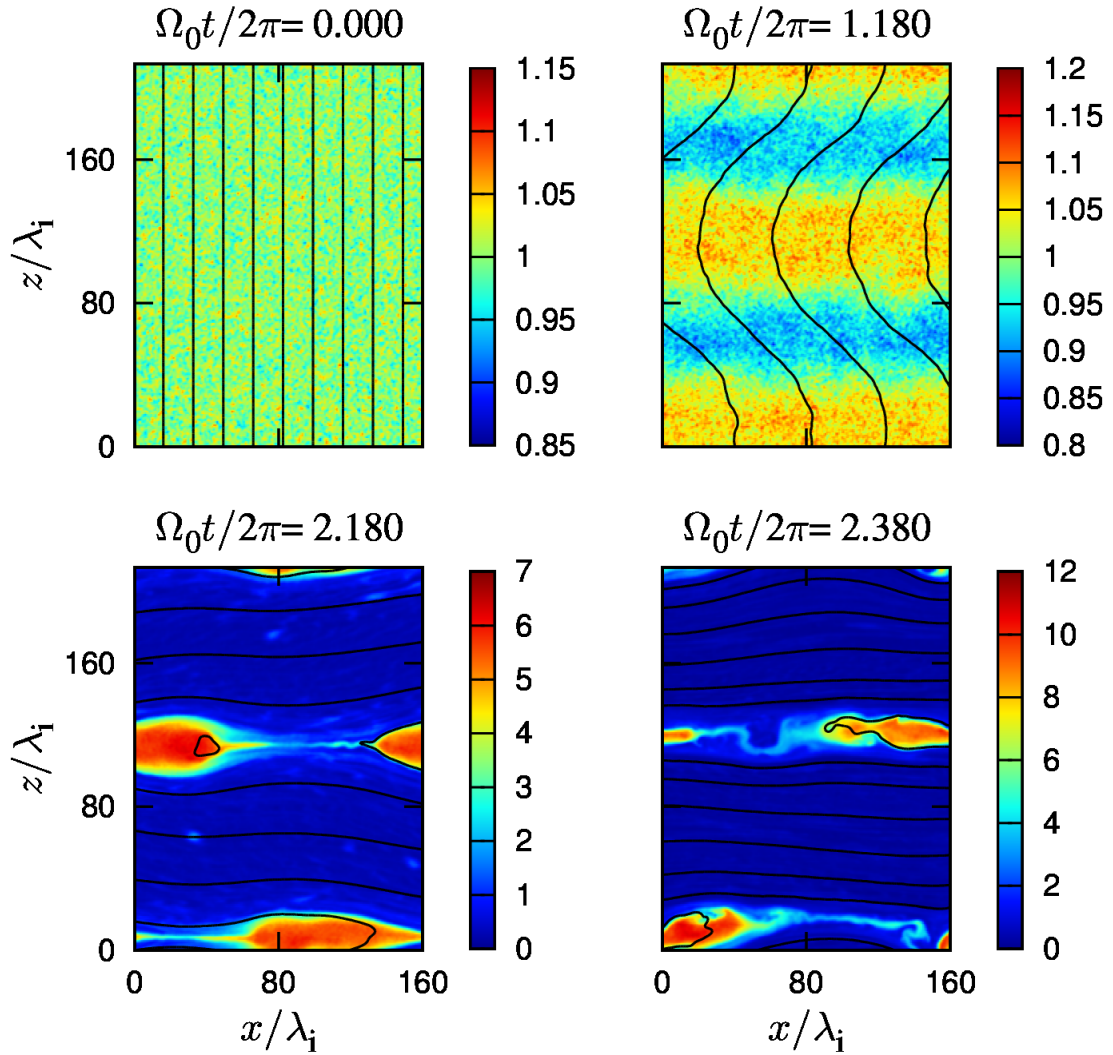


FIGURE 2.9: Time evolution of ion energy spectra in the non-linear stage of the MRI. Significant heating is observed after the onset of magnetic reconnection ( $\Omega_0 t/2\pi = 5.32$ ).

### 2.3.6 $\beta_i=33$ Case (RUN B1)

Now let us look on to the low  $\beta_i$  case. Figure 2.10 shows a time evolution of the system. As it was the case in RUN B2, the channel flow was also created. In the non-linear regime, magnetic reconnection takes place as well and magnetic islands

FIGURE 2.10: Same as Figure 2.5. Initial  $\beta_i$  was set to be 33.

start to be generated. Figure 2.11 shows averaged cut of pressure anisotropy in this run. As it was seen in RUN B2, perpendicular pressure anisotropy is dominant in the entire domain and the growth rate of the tearing mode is enhanced at  $\Omega_0 t / 2\pi \simeq 2.18$  (Black Line). However, at  $\Omega_0 t / 2\pi = 2.40$ , parallel pressure anisotropy is dominant in the channel flow (current sheet) region, and the tearing mode is suppressed (Red Line). Generation of parallel pressure anisotropy is primarily understood from the CGL equation which represents the conservation of 2nd adiabatic invariant ( $p_{\parallel} B^2 / \rho^3 = \text{const.}$ ). In the low  $\beta_i$  case, dissipation of magnetic energy gives significant change in the pressure anisotropy, since the magnetic field has relatively high energy with respect to the thermal energy compared to the higher  $\beta_i$  case. Since the dissipation due to the magnetic reconnection is

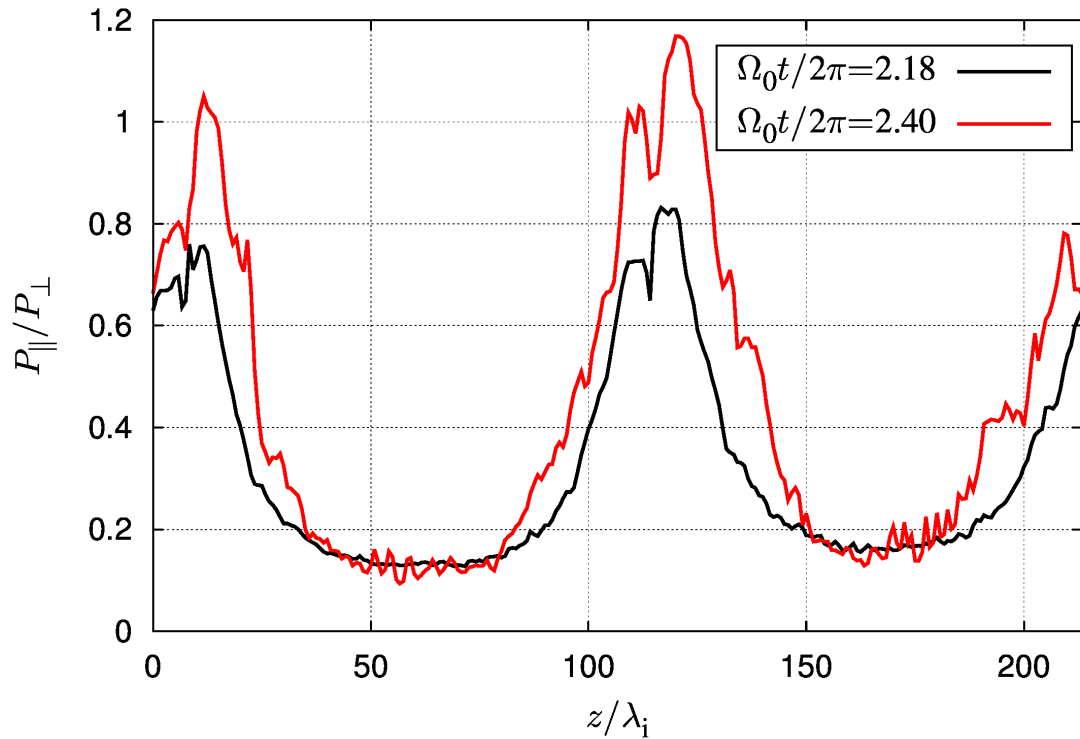


FIGURE 2.11: Averaged pressure anisotropy from RUN B1 during the magnetic reconnection (black line) and after the reconnection (red line). Initial  $\beta_i$  was set to be 33.

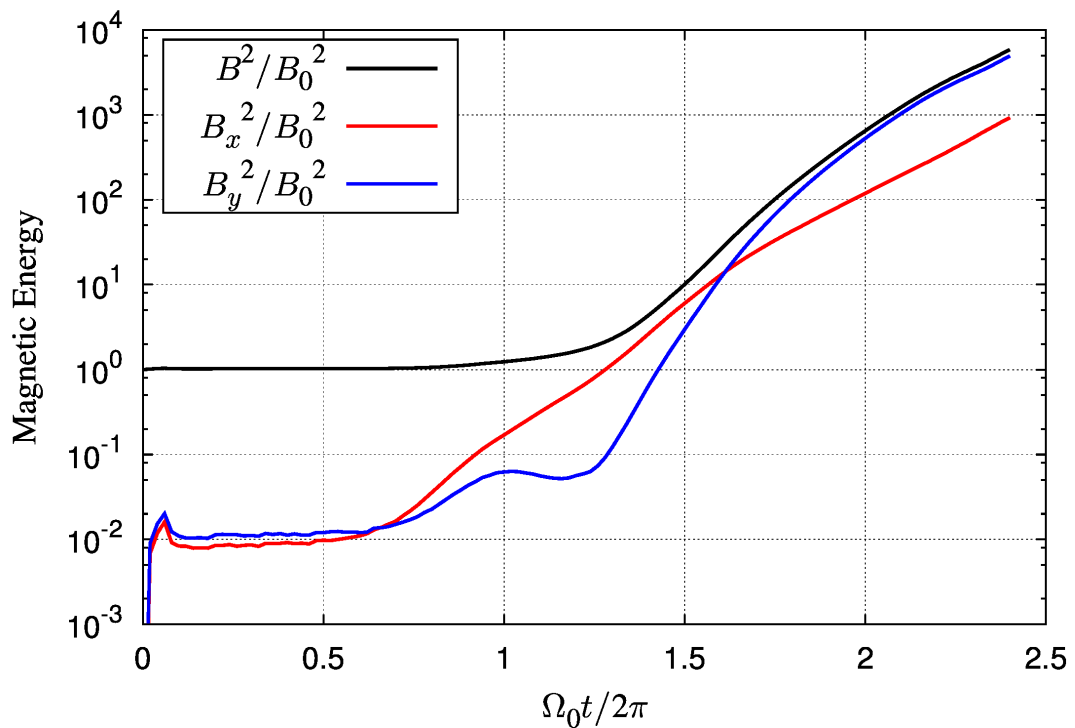


FIGURE 2.12: Same as Figure 2.6. Initial  $\beta_i$  was set to be 33.

suppressed, the magnetic energy keeps increasing (Figure 2.12) and the saturation of the system was not attained. The stress components did not reach its temporal maximum as well, and at the final state, the value of  $\alpha$  in this run was approximately 1.5.

### 2.3.7 $\beta_i=333$ Case (RUN B3)

For the high  $\beta_i$  case, the basic evolution of the system was the same as RUN B2. As shown in Figure 2.13, in the non-linear regime, a set of channel flow was generated. Figure 2.15 shows an averaged cut of the pressure anisotropy at  $\Omega_0 t / 2\pi = 8.86$ . As it was the case in RUN B2, perpendicular pressure anisotropy was dominant in the entire domain, and the onset of magnetic reconnection took place. This feature took place until the termination of calculation.

However in this run, the numerical noise generated in the density depletion region near the separatrix was even more severe compared to RUN B2. As it was seen in RUN B2, the magnetic energy did not reach the saturation (Figure 2.14). In contrast to RUN B2, the stress components did not reach its temporal maximum (not shown here.). The  $\alpha$  also seemed to be increasing at the final state, and the value of  $\alpha$  was approximately 0.6.

## 2.4 Summary of this Chapter

In this chapter, we have investigated the non-linear evolution of MRI using hybrid code. As pointed out in the introduction, linear to quasi-linear evolution of MRI and resulting generation of pressure anisotropy has been reported by Kunz et al. [2014b]. However heavily non-linear calculation of the MRI has not been reported with hybrid code even for the 2.5D problem. We consider this is because conventional hybrid code requires extremely severe CFL condition which is determined

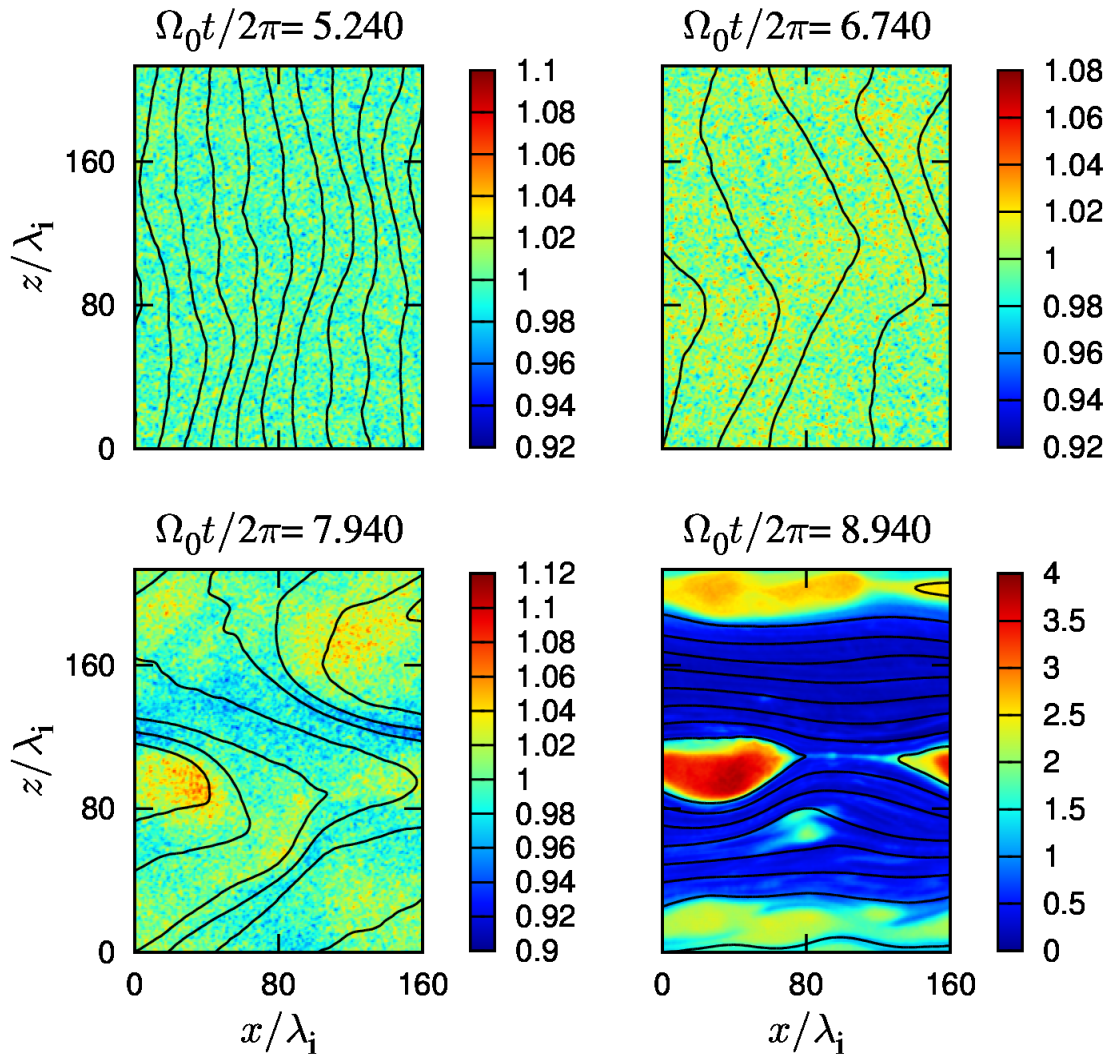


FIGURE 2.13: Same as Figure 2.5. Initial  $\beta_i$  was set to be 333.

by R-Mode wave. We have overcome this severe condition by introducing the finite electron mass and reducing the phase velocity of the R-Mode wave based on Amano et al. [2014].

From the results we have obtained a corruption of the generated channel flow due to the magnetic reconnection. In the past studies of the 2.5D MRI simulation, codes based on the MHD approximation gave a set of channel flows as a final state of the evolution. Theoretically this is consistent with the result that the channel flow solution is the exact analytic solution of MHD equations (Goodman and Xu [1994]) in the differentially rotating system. In addition since 2.5D simulation is restricted in the meridional plane, the reconnection and resulting corruption of the

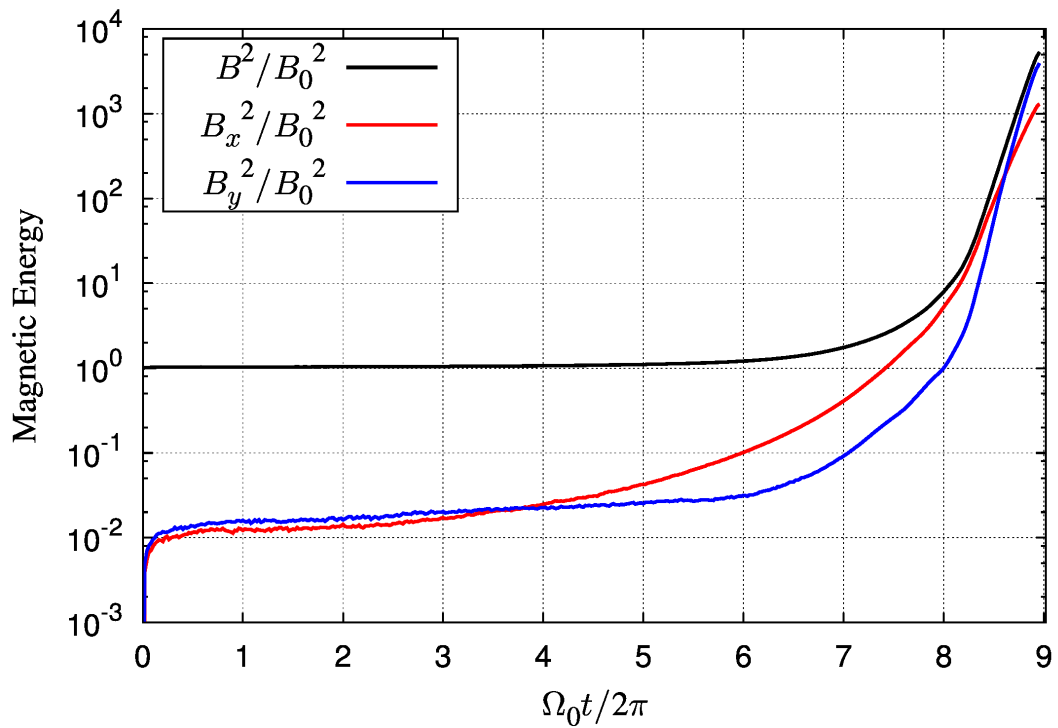


FIGURE 2.14: Same as Figure 2.6. Initial  $\beta_i$  was set to be 333.

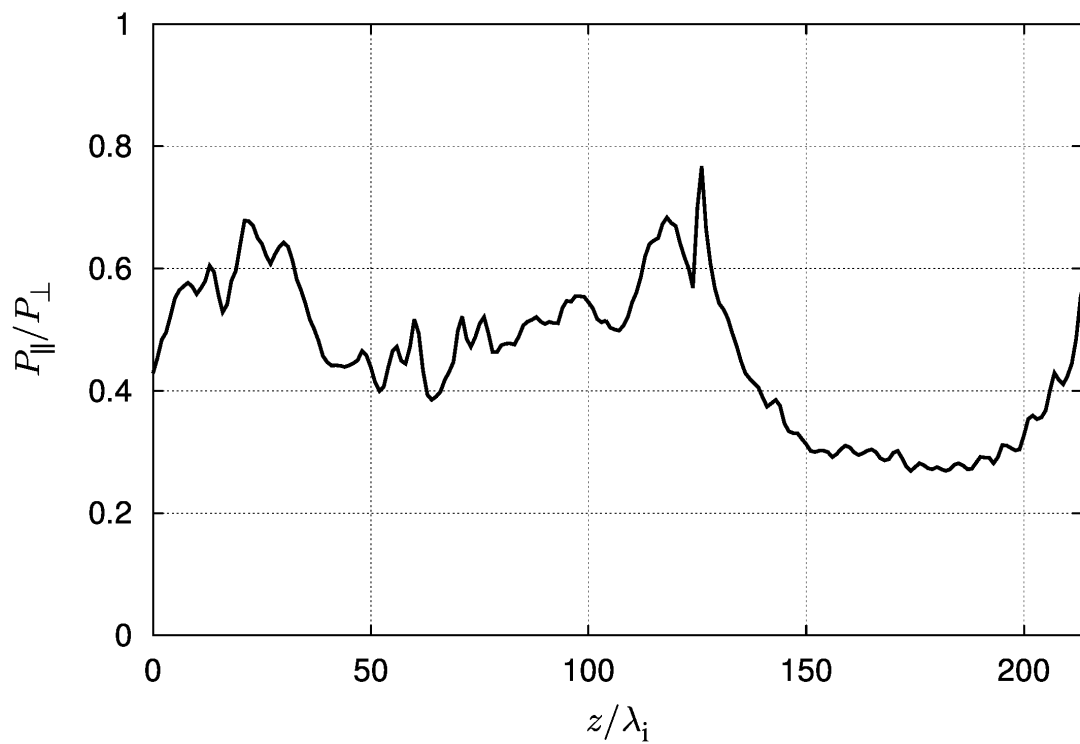


FIGURE 2.15: Averaged pressure anisotropy (solid line) at  $\Omega_0 t / 2\pi = 8.86$ . The initial  $\beta_i$  was set to be 333.

channel flow is well approximated by the oblique mode of tearing instability. Since the oblique tearing mode has lower growth rate compared to the parallel mode (Furth et al. [1963]; Cao and Kan [1991]), in the 2.5D configuration, corruption of the channel flow was not observed.

In our calculation, perpendicular pressure anisotropy associated with growth of the magnetic field enhanced the growth of magnetic reconnection, and the formation of magnetic islands is observed. In the non-linear state of the MRI, the perpendicular pressure anisotropy dominated in the entire domain, and as a result growth of magnetic reconnection is enhanced. These features are basically consistent with the results using full particle codes (Hoshino [2013]) and we consider the corruption of the channel flow and formation of magnetic islands are a general features in the collisionless 2.5D differentially rotating system. Accompanied with the magnetic reconnection, onset of the generation of non-thermal ions were observed in our simulation. However, our simulation terminated at that moment and further evaluation could not be attained. In contrast to the PIC results our calculation did not reach saturation of magnetic field energy. This is mainly because density depletion layer is formed in the vicinity of the separatrix (Shay et al. [1998]). Though our method is “almost” free from the division-by-density operation, the continuous generation of the density depletion region disturbs a stable calculation. Considering an application to a 3D MRI simulation, we expect that this will not be a serious problem, since in the 3D system, growth of the parallel mode of tearing instability can be taken into account and the rapid release of the magnetic energy is expected.

Our simulation did not reach saturation however, the stress parameter  $\alpha$  reached temporal maximum in RUN B2. Evaluated value of  $\alpha$  was 0.1-1, which was also consistent with the PIC result. This result may imply that in the collisionless system, relatively high  $\alpha$  parameter is attained compared to the MHD case. Comparing each stress component, Maxwell stress was the most effective, and anisotropic stress had relatively minor modification on  $\alpha$ .

---

Though there is still limitation in calculating a differentially rotating system with hybrid code, we have investigated the heavily non-linear regime of collisionless MRI in this chapter. We believe our method introduced here gives a robust approach for the further calculation in the 3D system. For the extension to the 3D calculation, massive numerical resources are required.

In the following chapter, we will rather focus on microscopic activities which would take place in the MRI induced turbulence. In particular, we will focus on the evolution of magnetic reconnection. In the saturated state of turbulence in the differentially rotating system, stretching of the magnetic field by shear flow and the dissipation of the field by magnetic reconnection is balanced. By studying the behavior of magnetic reconnection in the shear flow, we will provide a microscopic picture of magnetic field dissipation in the disk turbulence.

## Chapter 3

# Magnetic Reconnection in the Meridional Plane of the Disk

In this chapter we introduce non-linear evolution of collisionless magnetic reconnection under the effect of differential rotation. We use a hybrid code including the effect of Keplerian rotation and the calculation is carried out on the meridional plane of the disk. The results and discussions introduced in this chapter is based on Shirakawa and Hoshino [2014]. As we described in the previous chapter, MRI is considered to play an important role on the transportation of the angular momentum by generating turbulence and strong turbulent viscosity in the disk. Magnetic reconnection, on the other hand also plays an important role on the evolution of the disk through dissipation of magnetic field enhanced by dynamo effect of MRI.

Using a hybrid code under the effect of differential rotation, we investigated behavior of a particular structure of a current sheet which would exist in the turbulence in the disk. Unlike the MRI evolution which we introduced in the previous chapter, magnetic reconnection basically releases magnetic energy. As a result, the CFL condition defined with R-Mode wave is relaxed as time goes on. So, in this chapter, we simply adopt a conventional hybrid model, that is, the stabilizing

technique using a finite electron mass is not used. As we did the previous chapter, we first tested our code with the “semi-1D” MRI evolution. The results also showed a good agreement with the linear analysis in MRI. Next we introduce non-linear evolution of magnetic reconnection in the meridional plane of the disk, with varying rotational parameters ( $\Omega_0/\Omega_{ci}$ ). From the calculation of the magnetic reconnection, we found an asymmetric structure in the out-of-plane magnetic field during the evolution of reconnection which can be understood by a coupling of the Hall effect and the differential rotation. We also found a migration of X-point whose direction is determined only by the initial sign of  $\mathbf{J}_0 \times \boldsymbol{\Omega}_0$  where  $\mathbf{J}_0$  is the initial current density in the neutral sheet and  $\boldsymbol{\Omega}_0$  is the rotational vector of the background Keplerian rotation. Associated with the migration of X-point we also found a significant enhancement of the perpendicular magnetic field compared to an ordinary MRI. MRI-Magnetic reconnection coupling and the resulting magnetic field enhancement can be an effective process to sustain a strong turbulence in the accretion disk and to a transport of angular momentum.

### 3.1 Introduction

Magnetic reconnection is known as an efficient mechanism to transform magnetic energy to kinetic energy of the plasma. The importance of reconnection is widely recognized in various environment in our universe such as in the earth’s magnetopause (e.g., Dungey [1961]), in the magnetotail (e.g., Asano et al. [2003]) and in the active region of the sun (e.g., Parker [1963]; Tsuneta [1996]). This plasma activity generates plasma heating, acceleration, and mixing in our universe.

Magnetic reconnection is also considered to play an essential role on the accretion disk activity. As we introduced in Chapter 2, magnetorotational instability (MRI) is considered to be an effective generator of the turbulence in the disk (e.g., Balbus and Hawley [1998]). The properties of saturated, quasi steady state of the MRI-induced turbulence is important since the effect of angular momentum

transport is determined via  $\alpha$  parameter (Shakura and Sunyaev [1973]), which is evaluated with averaged value of magnetic field and plasma velocity. Since the balance between magnetic field generation by MRI and the field dissipation by magnetic reconnection determines the saturation level of MRI-induced turbulence, non-linear evolution of magnetic reconnection in the differential rotation would be one of the fundamental but important problems in accretion disk evolution.

Evolution of magnetic reconnection in the differentially rotating system is well compared to those in the shear flow. There are several possible combinations of the configuration between the ambient magnetic field direction and the shear flow direction. In this chapter we first focus on the case such that the ambient magnetic field is aligned to the axis of rotation, and the reconnection takes place on the meridional plane of the disk. Evolution of magnetic reconnection with the existence of out of plane shear flow was studied by (Wang et al. [2008]; Wang et al. [2012]; Chen et al. [2013]) discussing a generation of out of plane magnetic field in the vicinity of the X-point due to the imposed shear flow. However, the evolution of the system considering the effect of gravity, and coupling with MRI has not been investigated. In addition, the previous studies were carried out with fluid based code which does not take kinetic effect of plasma into account. Since our interest is dragged to a collisionless accretion disk, kinetic effect of the plasma shall also be important in this study.

In this chapter by using a hybrid code, we investigate the evolution of magnetic reconnection in the meridional plane of a differentially rotating disk. By carrying out several runs with different rotational parameters, we investigate an effect of differential rotation on the evolution of magnetic reconnection. Since the calculation will be carried out in the meridional plane, MRI would take place during the evolution of magnetic reconnection. We will focus on the effect of differential rotation and MRI on the evolution of the magnetic field, and its implication on the saturation problem in the collisionless accretion disk.

The structure of this chapter is as follows. In Section 3.2, the basic equations and

setups are introduced. Next in Section 3.3, we introduce the results of the five consecutive runs varying the strength of differential rotation. At last in Section 3.4, we summarize our results and discuss their effects on the MRI.

## 3.2 Hybrid Simulation in a Differentially Rotating System

### 3.2.1 Basic Equations

In this chapter, we focus on the evolution of the magnetic reconnection. In contrast to the previous chapter, magnetic reconnection releases the magnetic field energy and density profile gradually shifts to a uniform distribution. Therefore, in contrast to the MRI simulation, neither severe CFL condition nor “division-by-density” operation would be a fatal problem here. So, in this chapter we simply use the conventional set of equations for hybrid simulation under the effect of Keplerian rotation.

$$\frac{d\mathbf{x}_i}{dt} = \mathbf{v}_i \quad (3.1)$$

$$n_i = \sum_{\text{particle}} S(\mathbf{x}_i) \quad (3.2)$$

$$n_e \simeq n_i \quad (3.3)$$

$$q_i = -q_e \quad (3.4)$$

$$m_i \frac{d\mathbf{v}_i}{dt} = q_i \left( \mathbf{E} + \frac{1}{c} \mathbf{v}_i \times \mathbf{B} \right) - 2m_i \boldsymbol{\Omega}_0 \times \mathbf{v}_i - 2m_i q \Omega_0^2 x \hat{\mathbf{e}}_x, \quad (3.5)$$

$$\frac{\partial \mathbf{B}}{\partial t} = -c \nabla \times \mathbf{E}. \quad (3.6)$$

$$\mathbf{E} = -\frac{1}{c} \mathbf{V}_e \times \mathbf{B} + \frac{\nabla P_e}{n_e q_e} + \eta \mathbf{J} \quad (3.7)$$

$$\mathbf{J} = n_e q_e \mathbf{V}_e + n_i q_i \mathbf{V}_i = \frac{c}{4\pi} \nabla \times \mathbf{B} \quad (3.8)$$

$$P_e \propto n_e^\gamma. \quad (3.9)$$

As introduced in the previous chapter,  $q$  is set to be  $-3/2$ . Derivation and details about the above equations are introduced in Chapter 2. Note that we do not calculate an elliptic equation in this series of simulations. Like we did in the previous chapter, we have carried semi-1D MRI evolution test. The results showed good agreement with the linear theory.

### 3.2.2 Initial Conditions and Simulation method

As described in the former section we investigate an evolution of the system in the 2.5 dimensional meridional  $(x, z)$  plane. Figure 3.1 shows a schematic illustration of the system we calculate in this chapter. The size of the domain is set to be  $L_x \times L_z = 160 \times 960$  cells whose grid interval  $(\Delta x)$  is set to be the half of the ion inertia length  $(\lambda_i)$ . As an initial condition we adopt double Harris sheets (Harris [1962]) along  $z$ -direction,

$$B_{z0}(x) = B_0 \left[ \tanh \left( \frac{x - x_c(t)}{l} \right) - \tanh \left( \frac{x - x'_c(t)}{l} \right) - 1 \right]. \quad (3.10)$$

Here  $l$  is the half width of the current sheet and is set to be  $1.8\lambda_i$  throughout this article.  $x_c(t), x'_c(t)$  is the center of each current sheet and as we shall describe in Appendix E, the center of current sheet is not fixed in our simulation model. Initially,  $x_c(0)$  and  $x'_c(0)$  are located on  $L_x/4, 3L_x/4$ , respectively. To satisfy the initial pressure equilibrium ( $B^2/8\pi = n_c(T_i + T_e)$ ), ions are assumed to have a spacial distribution of,

$$n_i(x) = n_c \left[ \cosh^{-2} \left( \frac{x - x_c(t)}{l} \right) + \cosh^{-2} \left( \frac{x - x'_c(t)}{l} \right) \right] + n_0, \quad (3.11)$$

where  $n_c$  is the number density at the center of the current sheet and  $n_0$  is the number density in the outside of the current sheet region. In the following calculations we use 55 superparticles per cell in the outside of the current sheet region. For the velocity distribution the ions are assumed to have a shifted-Maxwellian

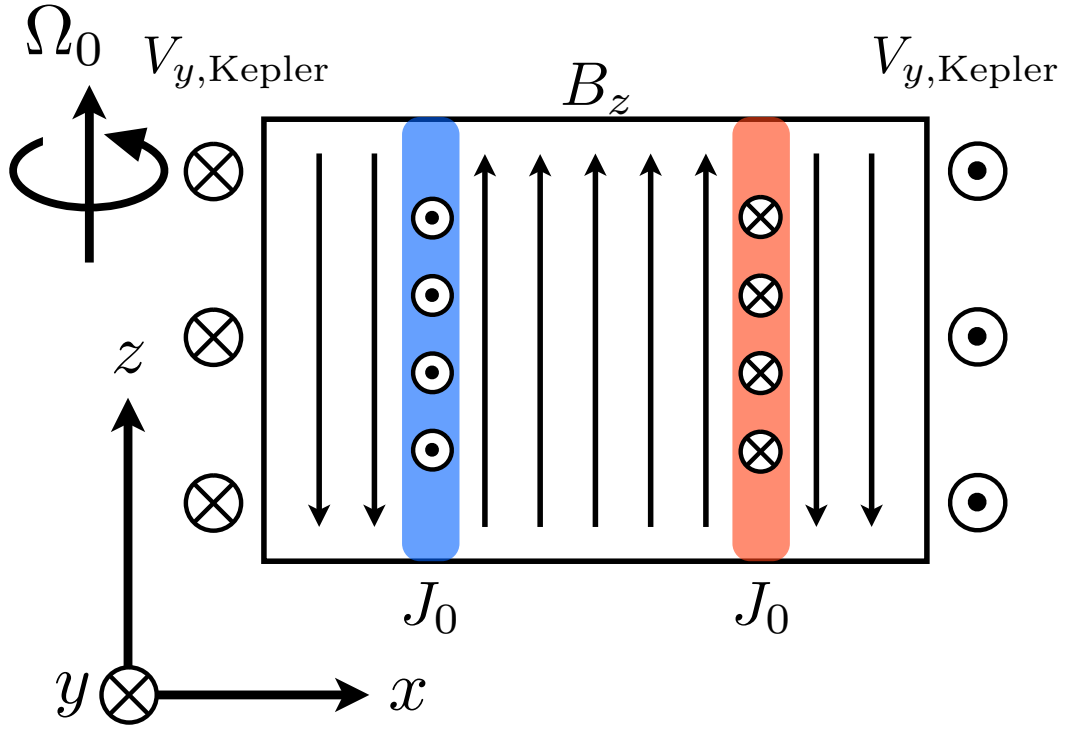


FIGURE 3.1: Schematic illustration of initial condition used in this chapter.

distribution with a background Keplerian rotation,

$$f_i(\mathbf{x}_i, \mathbf{v}_i) = n_i(x) \left( \frac{m_i}{2\pi T_i} \right)^{3/2} \exp \left[ -\frac{m_i}{2T_i} (v_x^2 + (v_y - v_{Ky}(x) - v_{d,i})^2 + v_z^2) \right] \quad (3.12)$$

where  $T_i$  is the initial temperature of the ion and  $v_{d,i}$  is the ion drift velocity which is defined as,

$$v_{d,i} = \frac{2cT_i}{q_i B_0 l}, \quad (3.13)$$

and set to be constant. It should be noted that the Harris solution is not an exact equilibrium in this system. Since the ion drift has  $y$ -component velocity, the balance between the centrifugal force and the tidal force is not satisfied for the drifting ions. However we have confirmed that the Harris solution is an approximate equilibrium in this system for sufficiently small rotational parameter.

Details are discussed in Appendix E.

In the following, all physical quantities are normalized with those of the parameters in the outside of the current sheet region. In the collisionless accretion disks such as disks around a black holes, the temperature of the electrons is considered to be much lower than that of the ions (Narayan et al. [1995]). Therefore we set the initial temperature of the electron as  $T_e = 5 \times 10^{-3} T_i$ . To save the integration time, we put localized perturbation in  $y$ -component of the vector potential following the form introduced in Zenitani et al. [2011],

$$\begin{aligned} \delta A_y = & 2lB_1 \exp \left[ -\frac{(x - x_c(t))^2 + (z - z_X)^2}{(2l)^2} \right] \\ & - 2lB_1 \exp \left[ -\frac{(x - x'_c(t))^2 + (z - z'_X)^2}{(2l)^2} \right], \end{aligned} \quad (3.14)$$

where  $z_X = L_z/4$ ,  $z'_X = 3L_z/4$  is the  $z$ -coordinate of the X-point and  $B_1$  is the strength parameter of the perturbation which is set to be  $0.12B_0$  in this calculation. In addition, we include a localized resistivity in the X-points,

$$\begin{aligned} \eta = \eta_0 & + \eta_c \cosh^{-2} \left[ \left( \frac{x - x_c(t)}{0.5\lambda_i} \right)^2 + \left( \frac{z - z_X}{\lambda_i} \right)^2 \right] \\ & + \eta_c \cosh^{-2} \left[ \left( \frac{x - x'_c(t)}{0.5\lambda_i} \right)^2 + \left( \frac{z - z'_X}{\lambda_i} \right)^2 \right], \end{aligned} \quad (3.15)$$

and the magnetic Reynolds numbers defined with  $\lambda_i V_{A0}/\eta_0$  and  $\lambda_i V_{A0}/\eta_c$  are set to be 2000 and 200, respectively. Here,  $V_{A0}$  is the Alfvén velocity defined with the outside the current sheet parameters. Here we impose the uniform resistivity since the magnetic reconnection does not occur in the ideal MHD limit. Therefore, we choose sufficiently small value of the resistivity for the uniform component and compare our results with the theory of the MRI under the ideal MHD approximation. The localized resistivity is imposed as anomalous resistivity due to the several instabilities generated in the vicinity of the X-point, such as lower hybrid instability (e.g., Higashimori and Hoshino [2012]). As we will discuss in Appendix

E, we have confirmed that the following results are not affected by the localized resistivity. With this initial condition we perform five runs varying the rotational parameter ( $\Omega_0/\Omega_{ci}$ ). Here  $\Omega_{ci}$  is the ion cyclotron frequency defined with the outside of the current sheet parameters. We choose RUN A which has no rotation as a fiducial run and gradually increase the rotational parameter. Several important parameters in the calculation are described in Table 3.1. In RUN B and C the rotational parameter does not exceed the instability criteria for the MRI defined with the parameters in the outside of the current sheet region,

$$\Omega_0^2 > \frac{k^2 V_{A0}^2}{3}. \quad (3.16)$$

On the other hand with the rotational parameter used in RUN D and E, the entire domain is unstable to the MRI. In RUN D resulting fastest growing wavelength of the MRI defined with the parameters in the outside of the current sheet region is the same as  $L_z$ , whereas in RUN E the fastest growing wavelength is the same as  $L_z/2$ . The other parameters used in the simulation are listed in Table 3.1.

TABLE 3.1: Simulation Parameters.

	RUN A	RUN B	RUN C	RUN D	RUN E
$L_x \times L_z$	$80\lambda_i \times 480\lambda_i$				
$\lambda_i$	$2\Delta x$				
$n_c/n_0$	4	4	4	4	4
$\beta_{i,Out}^1$	1.0	1.0	1.0	1.0	1.0
$p_e/p_i$	$5 \times 10^{-3}$				
$\Omega_0/\Omega_{ci}$	0	$2 \times 10^{-4}$	$5 \times 10^{-3}$	$1.35 \times 10^{-2}$	$2.70 \times 10^{-2}$

<sup>1</sup>Ion plasma beta defined with outside of the current sheet parameter.

## 3.3 Results

### 3.3.1 Overview

Let us go on to the results of the magnetic reconnection. We first overview our results. Figure 3.2 shows the structures of five runs at each stage of the reconnection. The most distinct feature is found in RUN E whose magnetic field line in the entire region of the simulation domain is remarkably bent. We consider that in this parameter the MRI is the dominant process for the evolution of the system. The relation between the magnetic reconnection and the MRI shall be discussed in the following section. In RUN B, C and D the effect of the Kepler rotation seems to be relatively moderate compared to RUN E. At the onset stage of the reconnection ( $\Omega_{ci}t \simeq 144$ ) there is no significant difference in the structure between each run. However, as the reconnection goes on, an asymmetric structure gradually becomes remarkable in RUN B, C and D. The asymmetry becomes clearer as the rotational parameter increases. In addition, a migration of X-point is observed in all run with the finite Kepler rotation (RUN B-E). A physical interpretation of this migration shall also be discussed in the following section. Another asymmetry is also found in the out-of-plane magnetic field. Figure 3.3 shows the structure of the out-of-plane magnetic field ( $B_y$ ) at the final stage of five runs. It is clear, especially in RUN C and D, the absolute value of  $B_y$  is, in average, larger in the right side of the X-point compared to that in the left side. This is understood by considering the coupling of the Hall effect and the differential rotation and shall be discussed in the next section as well.

### 3.3.2 Asymmetric evolution of out-of-plane magnetic field

It is well known that the quadrupole structure in the out-of-plane magnetic field is observed around the X-point in the numerical simulation under the framework which distinguishes the magnetization degree of the ions and the electrons. In the

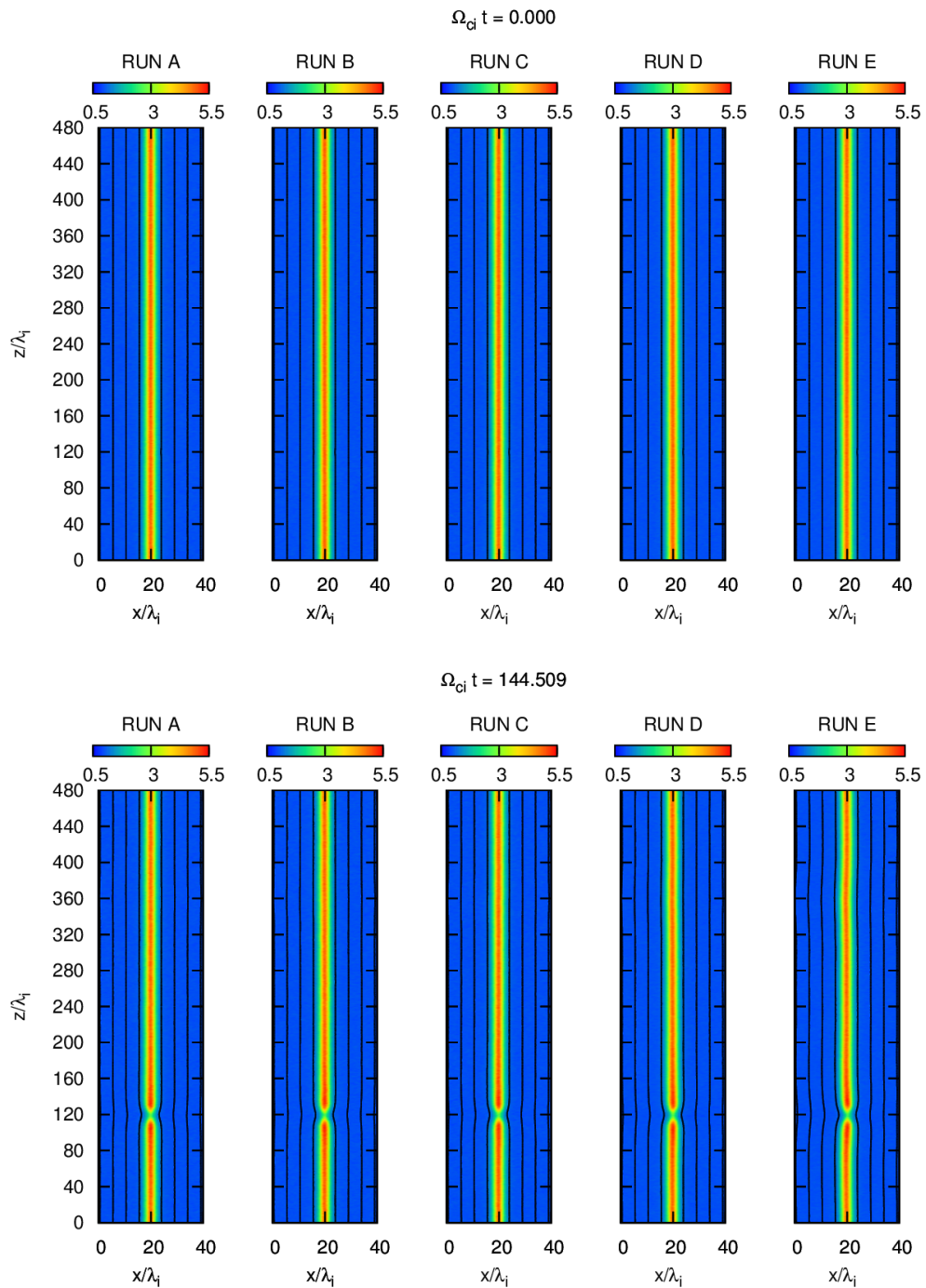


FIGURE 3.2: Time evolution of all runs. The color contour corresponds to ion density whereas the solid line corresponds to the magnetic field line. The figures are focused on the left half of the simulation domain.

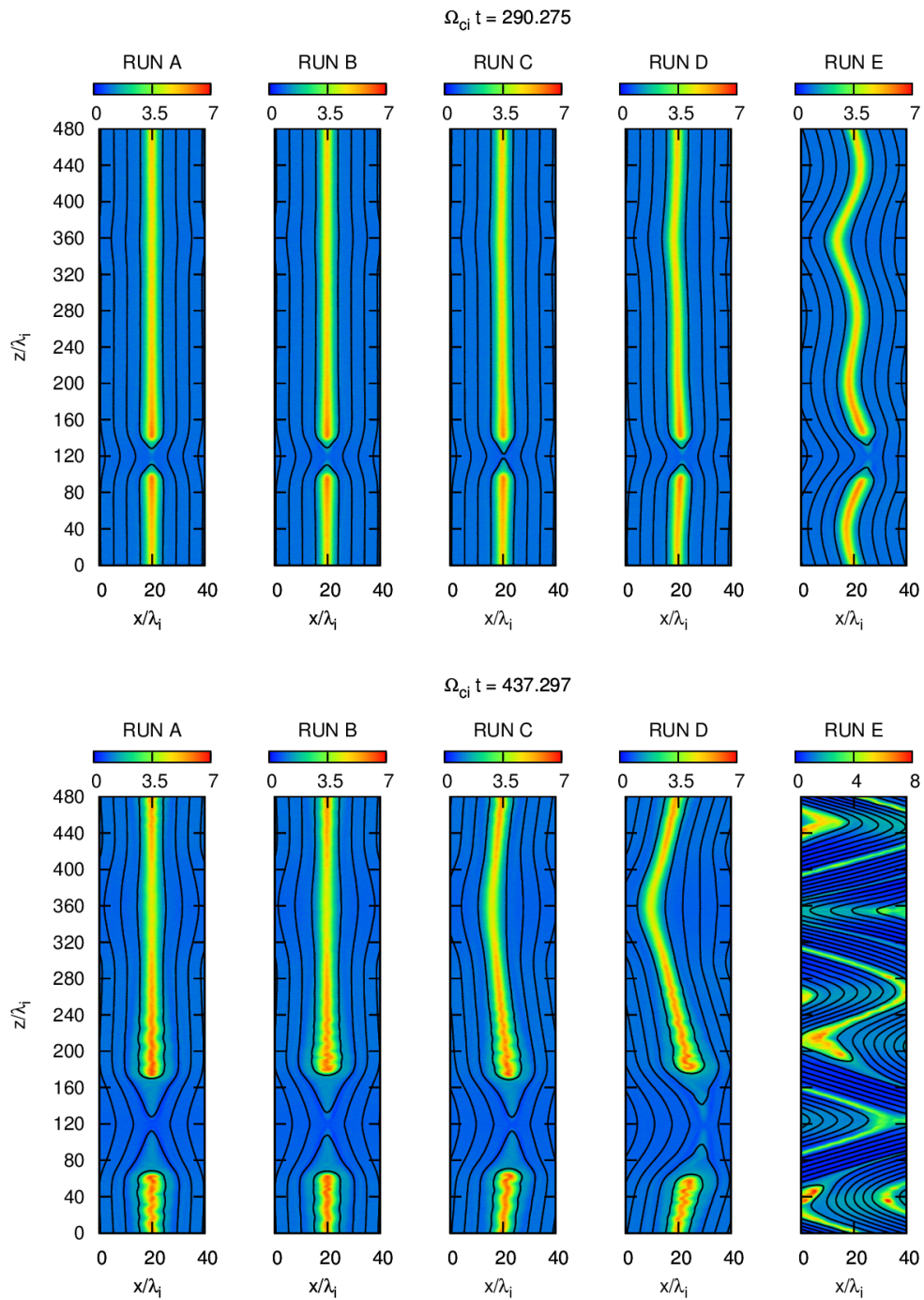


FIGURE 3.2: Continued.

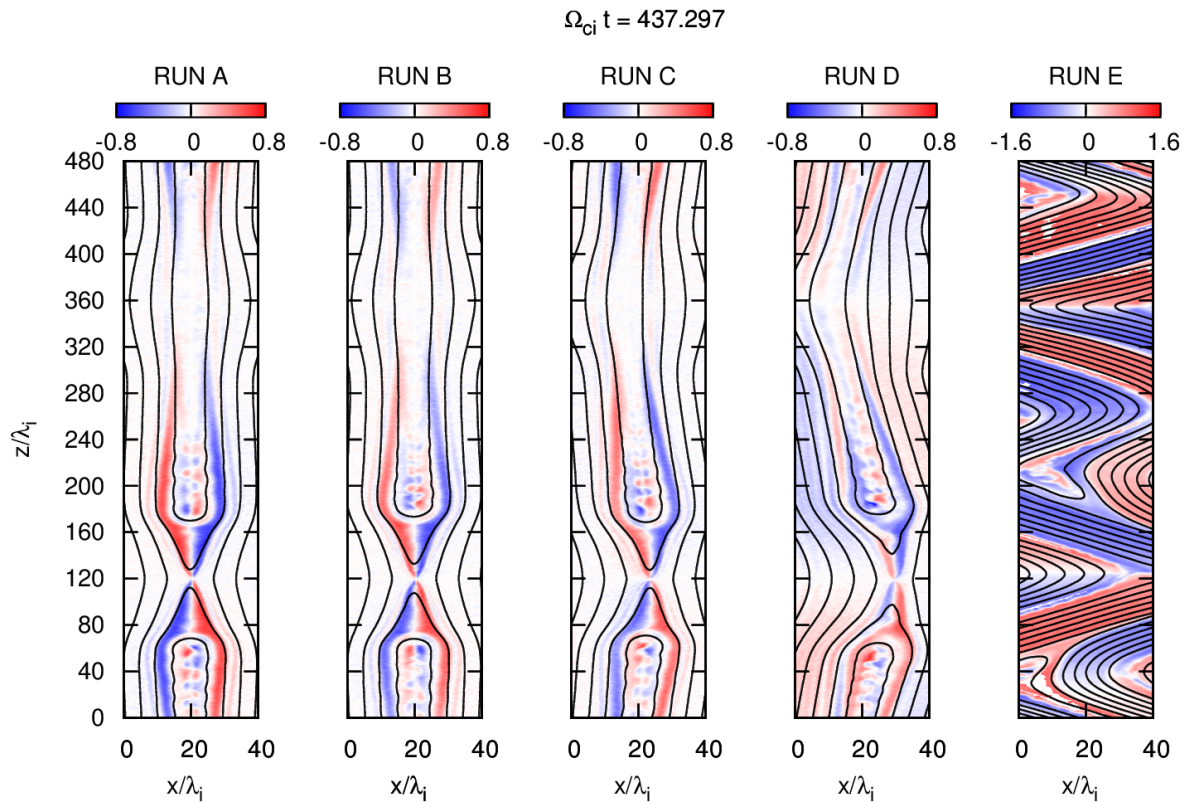


FIGURE 3.3: (Color) Out-of-plane magnetic field ( $B_y$ ) in the final stage of the simulation.  $B_y$  in RUN E is remarkably enhanced due to the dynamo effect of the MRI. The figures are focused on the left half of the simulation domain. (Solid line) Magnetic field.

hybrid framework which treats the ions as superparticles with finite mass and the electrons as massless charge neutralizing fluid, the magnetization feature of each component is also distinguished. This gives a significant difference in the motion of each component around the X-point resulting the in-plane Hall current and out-of-plane magnetic field (Sonnerup [1979]).

In our fiducial run (RUN A), a clear quadrupole structure is also found in a symmetric manner (Figure 3.3). As we pointed out in the previous section an asymmetric structure in the out-of-plane magnetic field ( $B_y$ ) is found in RUN B, C and D. The asymmetry becomes significant as the rotational parameter increases. Figure 3.4 shows a focused view of the out-of-plane magnetic field ( $B_y$ ) at  $\Omega_{ci} t \simeq 437$  of RUN D. The color contour in the right panel corresponds to  $B_y$ . In the left panel of Figure 3.4,  $B_y$  is also plotted along the dotted line denoted in the right

panel, and from the top to the bottom each panel corresponds to line A-D. The dashed red lines plotted vertically in the left panels correspond to the baseline which passes through the X-point. In cut C and D clear asymmetry with respect to the red line is observed and the absolute value of  $B_y$  is always found to be large in the right side of the X-point compared to the left side. These structures can be understood by a simple coupling between the Hall magnetic field produced by the reconnection and the effect of the differential rotation.

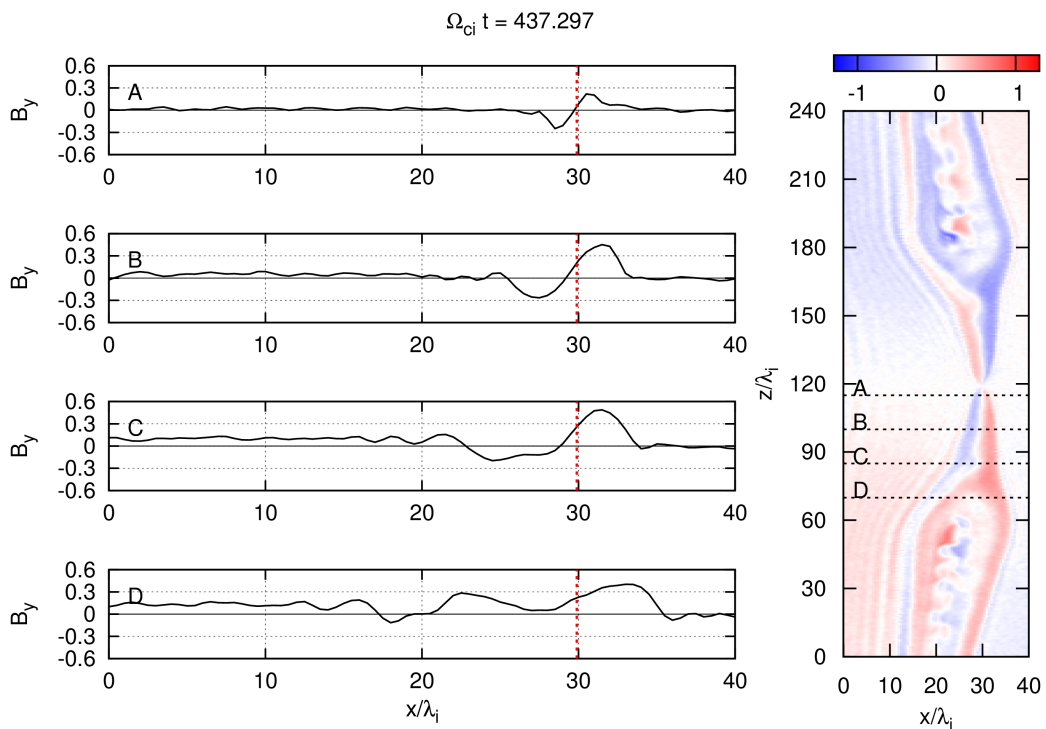


FIGURE 3.4: Focused view of out-of-plane magnetic field in RUN D.

Figure 3.5 shows the schematic view of the system. As the reconnection grows the quadrupole magnetic field parallel to the  $y$ -axis is generated due to the Hall effect. As the reconnection goes on and  $B_x$  is generated the dynamo effect of the differential rotation produces  $B_y$  following the  $y$ -component of the induction Equation (C.3). Since  $B_x$  generated by the reconnection has opposite sign on the different side of the X-point so as  $B_y$  generated by the shear motion. Superposing the quadrupole  $B_y$  due to the Hall current and the anti-symmetric  $B_y$  due to the shear motion, the asymmetric structure in the out-of-plane magnetic field is clearly

understood and in the case of Figure 3.5, for instance, the larger absolute value of  $B_y$  is observed in the right side of the X-point.

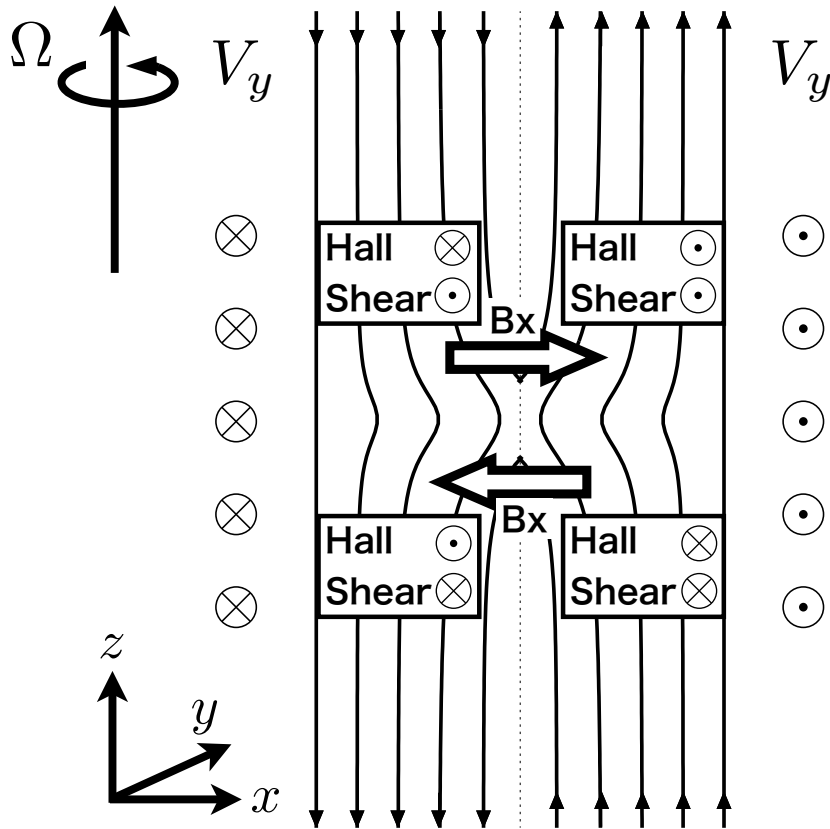


FIGURE 3.5: Schematic plot of the Hall Field and the sheared Field.

Paying attention to the fine structure, the “undulated” feature in the out-of-plane magnetic field is found in the non-linear stage of the reconnection. This structure is consistent with the one introduced in Arzner and Scholer [2001]. They have pointed out that the structure is a consequence of an instability driven by a shear flow along the magnetic field line and a parallel pressure dominance generated in the layer consisted with the outflow region and the outside of the current sheet region. We note that in our simulation setup with the finite rotational parameters, any scale of perturbation would be unstable to the MRI inside the current sheet following the conventional definition of the MRI criteria. This is because inside the current sheet the magnetic field gradually decreases whereas the density increases which leads to  $V_{A,Out} \rightarrow 0$  in the right hand side of the equation (3.16). However

as we can see from Figure 3.3, the characteristic scale of the “undulated” structure seems to be insensitive to the rotational parameter. Thus this structure can also be considered as the one introduced in Arzner and Scholer [2001] and the modulation by the MRI seems to be rather weak in this instability. In addition, a standing wave structure whose wave front is approximately parallel to the magnetic field line is found in the region where the transition takes place from the current sheet to the outside region ( $x/\lambda_i \lesssim 15$  in the right panel of Figure 3.4). Approximating the structure of current sheet as a slow shock, this wave structure is regarded as a standing wave train found in the dispersive shock when the ion inertia scale is much larger than the resistive scale (Hau and Sonnerup [1992]). These fine structures are found not only in RUN D but also in RUN A-C on which the effect of the Kepler rotation is relatively moderate.

### 3.3.3 Migration of the X-points

Another remarkable structure is found in the vicinity of the X-point. As described in the overview the asymmetry becomes significant as time goes by. At the same time, the X-point migrates in a certain direction. The direction of the X-point migration is determined by the sign of  $\mathbf{J}_0 \times \boldsymbol{\Omega}_0$ . The other X-point imposed in the other current sheet migrates to the different direction following the opposite sign of  $\mathbf{J}_0 \times \boldsymbol{\Omega}_0$ . The migration distance of the X-point is larger in the runs with the larger rotational parameter. Figure 3.6 shows a focused view of the X-point at  $\Omega_{ci}t \simeq 437$  in RUN D. Here, the color contour in the right panel corresponds to the ion density. In the left panels, we show several physical values along the dashed white line indicated in the right panel. From the top, the density (solid line) and the pressure (dashed line) of the ions, the moment averaged ion velocity ( $V_{x,\text{ions}}$ ), the  $y$ -component ion velocity deviation from the background Kepler rotation ( $V_{y,\text{ions}}$ ), and the magnetic energy normalized with the initial value in the outside of the current sheet region, are plotted. The horizontal red dashed line plotted in the

second row corresponds to the migration velocity of the X-point. In average, inflow speed of the ions from the both sides of the X-point are the same in the rest frame of the X-point.

The migration of the X-point itself is easily understood by the generation of the flow by the MRI. However the correlation between the sign of  $\mathbf{J}_0 \times \boldsymbol{\Omega}_0$  and the direction of the migration is not obvious. This correlation can be understood by considering the asymmetric growth of MRI with respect to the neutral sheet. Since the conventional criteria of the MRI is given by Equation (3.16), the MRI is always active inside the current sheet where the magnetic field strength and the ambient Alfvén velocity are infinitesimally small. However, since we have carried out the calculations under hybrid framework, the effect of the Hall term should also be taken into account. As reported in Balbus and Terquem [2001], the Hall term extends the unstable region of the MRI to a shorter wavelength when the orientation of the magnetic field and the background rotational vector is anti-parallel, and vice versa.

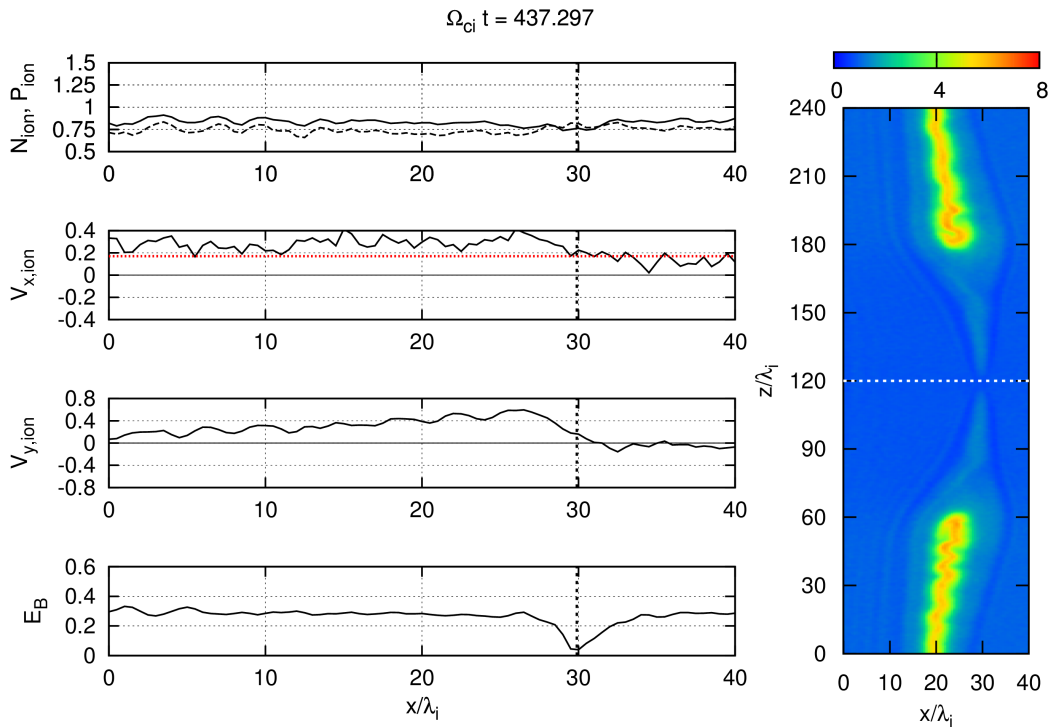


FIGURE 3.6: Focused view of the X-point in RUN D.

Figure 3.7 shows a growth rate of the MRI obtained from the linear analysis of Hall MHD equations. It is clear from the figure that the unstable region is extended when the ambient magnetic field is anti-parallel to the Keplerian rotation vector. With the Hall parameter defined in the outside of the current sheet region, the correction to the MRI growth rate is still minor. However, in the vicinity of the current sheet, the time scale of the cyclotron motion may reach that of the Kepler rotation, and as a result the Hall term would be effective in this region. In Figure 3.6, the ambient magnetic field is anti-parallel to the rotational vector in the left side of the current sheet and the instability criteria is reduced in this region. Therefore the small scale perturbation triggered by the magnetic reconnection would couple to the MRI and can be enhanced in this side of the current sheet resulting a migration of the X-point, whereas in the opposite side of the current sheet, the characteristic scale imposed by the magnetic reconnection does not satisfy the criteria of the MRI under the Hall effect. In addition, in the vicinity of the current sheet, Finite Larmor Radius (FLR) effect of the ions would also be important. Result of the linear analysis including the FLR effect suggests that the fastest growing scale of MRI under the opposite orientation of the magnetic field and rotational vector shifts to the smaller scale (Ferraro [2007]; Heinemann and Quataert [2014]) which even supports our understandings.

Looking on to the phase relation of the plasma velocity, we find  $V_{x,\text{ions}}/V_{y,\text{ions}} > 0$  in the left side of the X-point (the second and the third row of Figure 3.6). This phase relation is also satisfied during the growth stage of the MRI. We consider this phase relation also supports the explanation that MRI is active in the vicinity of the current sheet, and the difference on the growth rate depending on the direction of magnetic field and Keplerian rotation vector drives the X-point migration.

To confirm that the asymmetric evolution of the magnetic reconnection is driven by the Hall term, we have carried out another comparative run. In this run the grid interval was set to be twice as long as the ion inertia length defined with the parameter outside of the current sheet region. The ratio between the current sheet thickness and the grid interval was set to be the same as RUN A-E. Rotational

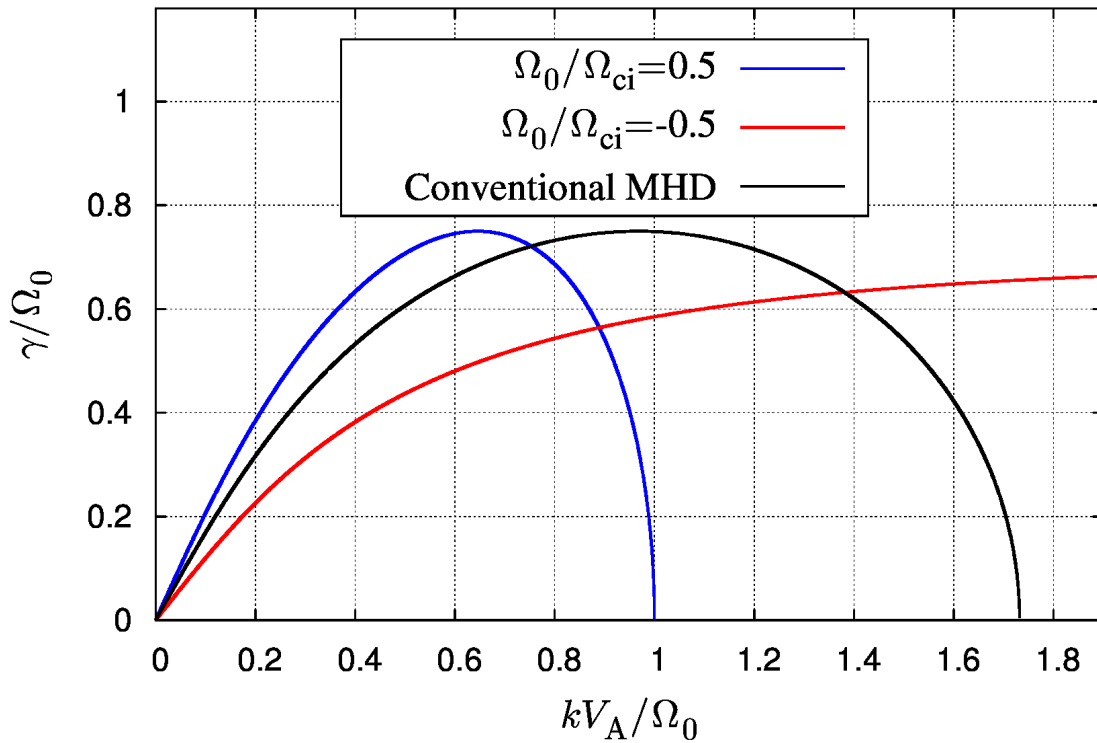


FIGURE 3.7: Growth rate of MRI with varying Hall parameter ( $\Omega_0/\Omega_{ci}$ ). The sign (+) corresponds to the case that the ambient magnetic field is parallel to the Keplerian rotational vector and vice versa. For the case  $\Omega_0/\Omega_{ci} = -0.5$ , the entire region is unstable to MRI.

parameter was set to be  $\Omega_0/\Omega_{ci} = 1.69 \times 10^{-3}$ . With this parameter, the fastest growing wavelength defined with the outside of the current sheet parameters is twice as long as the vertical size of the simulation domain.

Figure 3.8 shows a time evolution of the simulation with the reduced Hall effect. The plots are focused in the left half of the simulation domain. As we can see from the plot, there is no significant migration of the X-point even after the long term evolution. Therefore, we conclude that the migration of the X-point is caused by the Hall effect.

### 3.3.4 Magnetic reconnection as a trigger of the MRI

As we have described in the overview, in the outside of the current sheet region of RUN E, perpendicular magnetic field is remarkably enhanced which implies

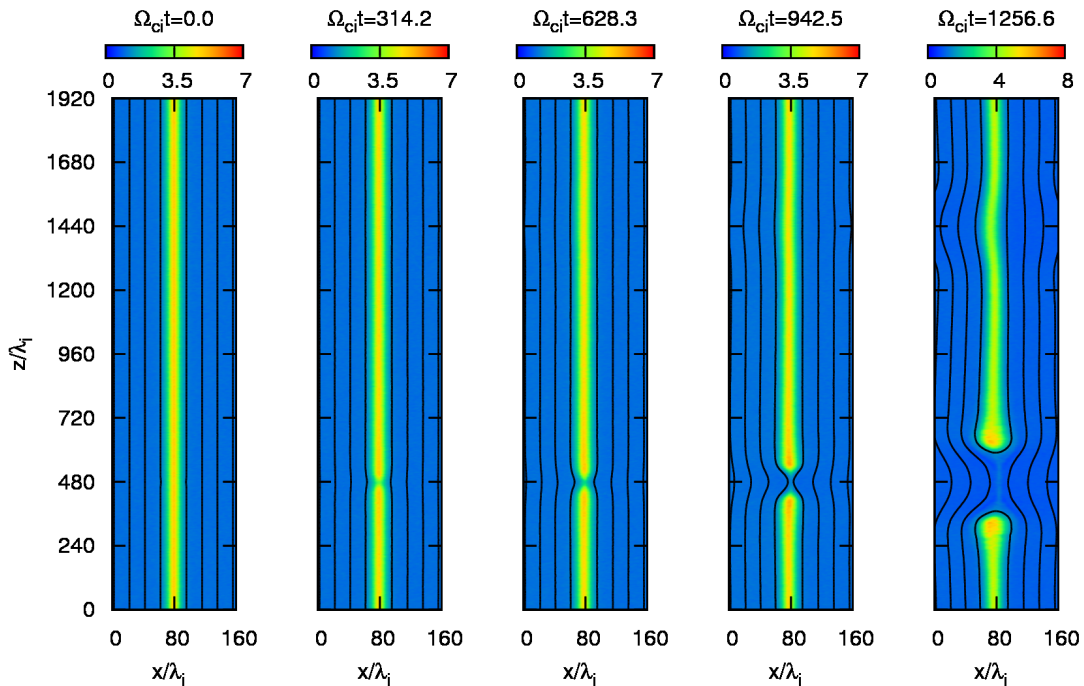


FIGURE 3.8: Time evolution of the density (color) and the magnetic field line (solid line) with reduced Hall effect.

the dominant process in this parameter regime is the MRI. During the evolution of the MRI, magnetic reconnection also takes place with the associating X-point migration giving additional growth of  $B_x$  together with the reconnection. In this section, we point out that the reconnection would also contribute to a relatively large initial perturbation on the growth of the MRI.

In order to evaluate the effect of the magnetic reconnection on the evolution of the MRI we perform another comparative calculation. Here we choose RUN E as a fiducial run and another run (RUN E2) is calculated without the initial trigger for the magnetic reconnection; by excluding the initial vector potential (3.14) and taking  $\eta_c = 0$  in the resistivity (3.15). Note that we have left the uniform component of the resistivity  $\eta_0$ . Therefore, under this initial condition, both a tearing mode instability and an MRI would take place. Here the fastest growth mode of the MRI in the outside of the current sheet region is  $0.75\Omega_0 \simeq 0.02\Omega_{ci}$  which is comparable to that of a tearing mode which can roughly be estimated as  $10^{-1}-10^{-2}\Omega_{ci}$  (e.g., Terasawa [1983]; Hesse and Winske [1993]).

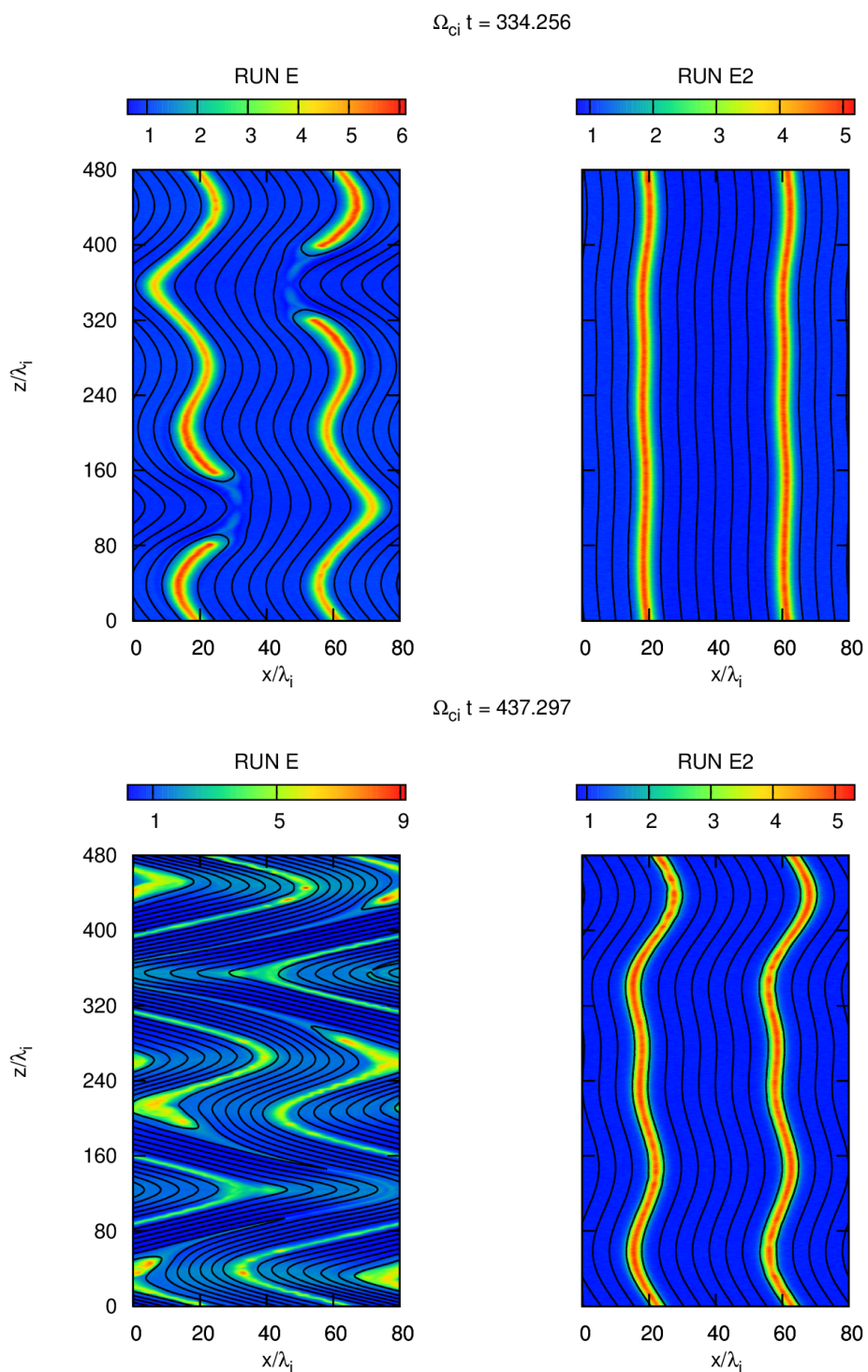


FIGURE 3.9: The density (color) and the magnetic field line (solid line) at the middle stage of RUN E and RUN E2 (top), and at the final stage (bottom).

Figure 3.9 shows the time evolution of the two comparative runs. Again the color contour corresponds to the ion density, and the solid line corresponds to the magnetic field line. From the top panel ( $\Omega_{ci}t \simeq 334$ ) we observe that the X-point in the different current sheet migrates in the opposite direction. From the bottom panel ( $\Omega_{ci}t \simeq 437$ ) it is clearly observed that the perpendicular component of the magnetic field is significantly enhanced in RUN E.

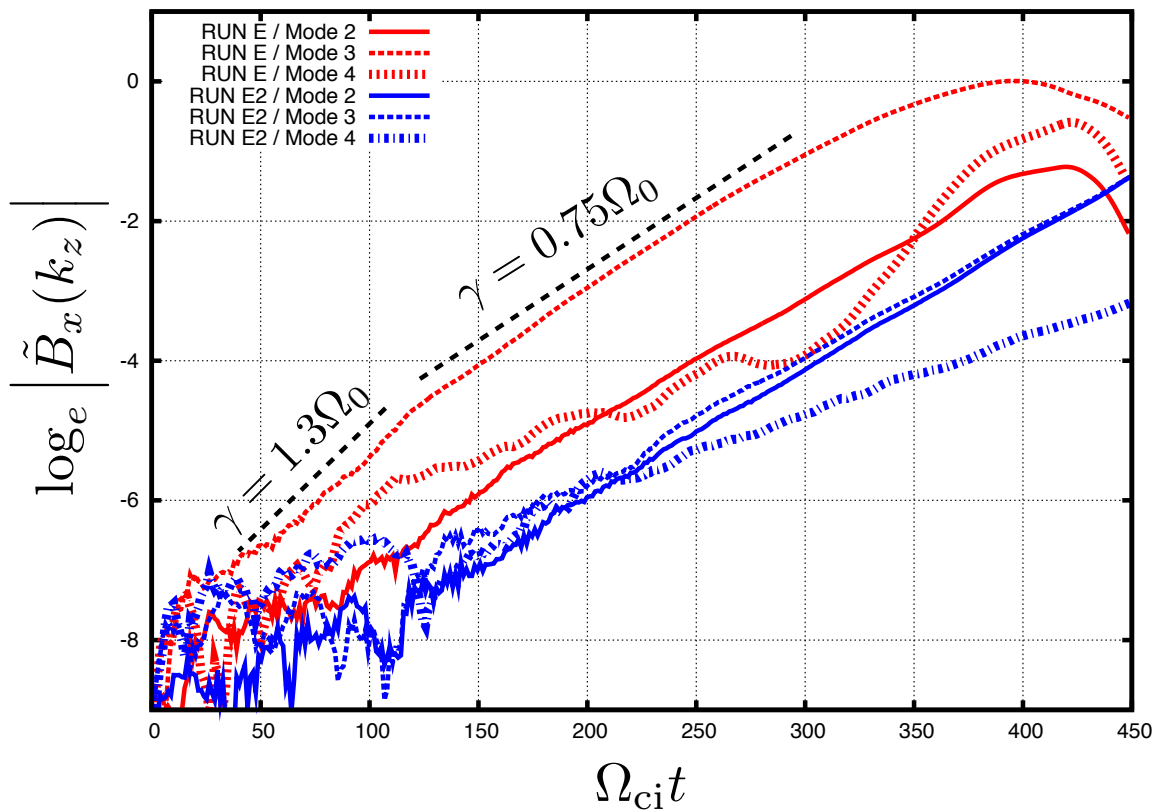


FIGURE 3.10: Time evolution of Magnetic Field Power from comparative runs (RUN E, RUN E2).

Another distinct feature is also found from the Fourier decomposition of  $|B_x|$  in each run. In Figure 3.10 we show the evolution curves of each mode in the both calculations. The Fourier transformation was applied on  $B_x$  along the  $z$ -axis in the outside of the current sheet region ( $10\lambda_i \leq x \leq 20\lambda_i$ ). In this region, we can approximate the uniform plasma background and can compare results with the theory of conventional MRI. Within the two runs we find no significant difference in the maximum growth rate and was the same as that of the conventional MRI

( $\gamma_{\max} = 0.75\Omega_0$ ) except for mode 3 in RUN E. During the initial growth stage of RUN E ( $0\Omega_{ci}t - 100\Omega_{ci}t$ ) the growth rate is roughly  $1.3\Omega_0$  which is about 1.8 times faster than that of the MRI. This implies that the magnetic reconnection and the associated X-point migration initially gives relatively large perturbation and act as an trigger for the MRI. During the middle stage of the evolution, the growth rates of all the modes do not exceed the maximum growth rate of the MRI. Triggered by the X-point migration, in this stage, the power of  $B_x$  in the outside of the current sheet region of RUN E is, in average,  $\sim 30$  times larger than that of RUN E2. It is worth noting that the fastest growing mode in RUN E is mode 3 even though the initial rotational parameter was set for mode 2 to be the most unstable. At the initial stage of reconnection, the reconnection rate corresponding to the separatrix angle determines the mode with the largest amplitude. At the same time, the X-point migration from the other current sheet gives perturbation towards opposite direction in  $z \simeq 3L_z/4$ . As a result at the initial growth stage a large amplitude perturbation corresponding to mode 3 is given by the magnetic reconnection and by the associating X-point migration. During the middle stage of the growth ( $\Omega_{ci}t \gtrsim 100$ ) the ambient magnetic field parallel to the rotational axis is weakened by magnetic reconnection leading shorter wavelength to be more unstable to the MRI. It is well known that the linear process of a 2.5D MRI also holds even the perturbed field amplitude is relatively large compared to the ambient field (Goodman and Xu [1994]). Therefore, in the middle stage of the evolution, mode 3 can be most unstable.

We have carried out another comparative run labeled RUN C2. In this run, all the parameter except for the rotational parameter was set to be the same as RUN C. For the rotational parameter, we have adopted  $\Omega_0/\Omega_{ci} = 6.75 \times 10^{-3}$ . In this case, the maximum growing wavelength defined with the parameter outside of the current sheet region will be twice as long as the vertical length of the simulation domain. Moreover, the critical wavelength of MRI defined with the same parameter is about 1.12 times longer than the vertical length of the simulation domain.

Therefore, the outside of the current sheet region is expected to be stable to the MRI. Figure 3.11 shows a time evolution RUN C2 focusing on the left half of the simulation domain.

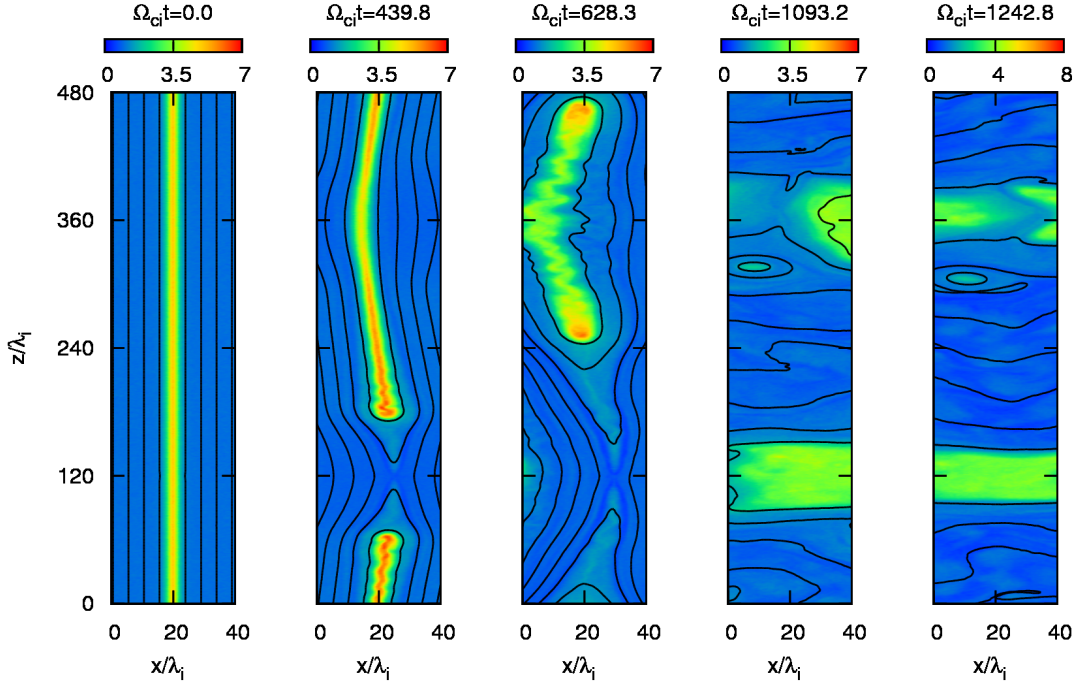


FIGURE 3.11: Long term evolution of RUN C2. The plots are focused on the left half of the simulation domain.

It is clearly observed that the asymmetric evolution of magnetic reconnection eventually grew to a set of channel flow, which is found in the non-linear stage of MRI. Figure 3.12 shows a time evolution of Fourier decomposition calculated with  $B_x$  outside of the current sheet region ( $10\lambda_i \leq x \leq 20\lambda_i$ ).

At the non-linear stage ( $\Omega_{ci}t \simeq 500-700$ ), Mode 1 of  $B_x$  grows with the maximum growth rate of MRI ( $\gamma = 0.75\Omega_0$ ) whereas in the linear to the quasi-linear stage ( $\Omega_{ci}t \simeq 0 - 500$ ) the growth rate is much larger, suggesting that the generation of  $B_x$  due to the magnetic reconnection is effective in this stage.

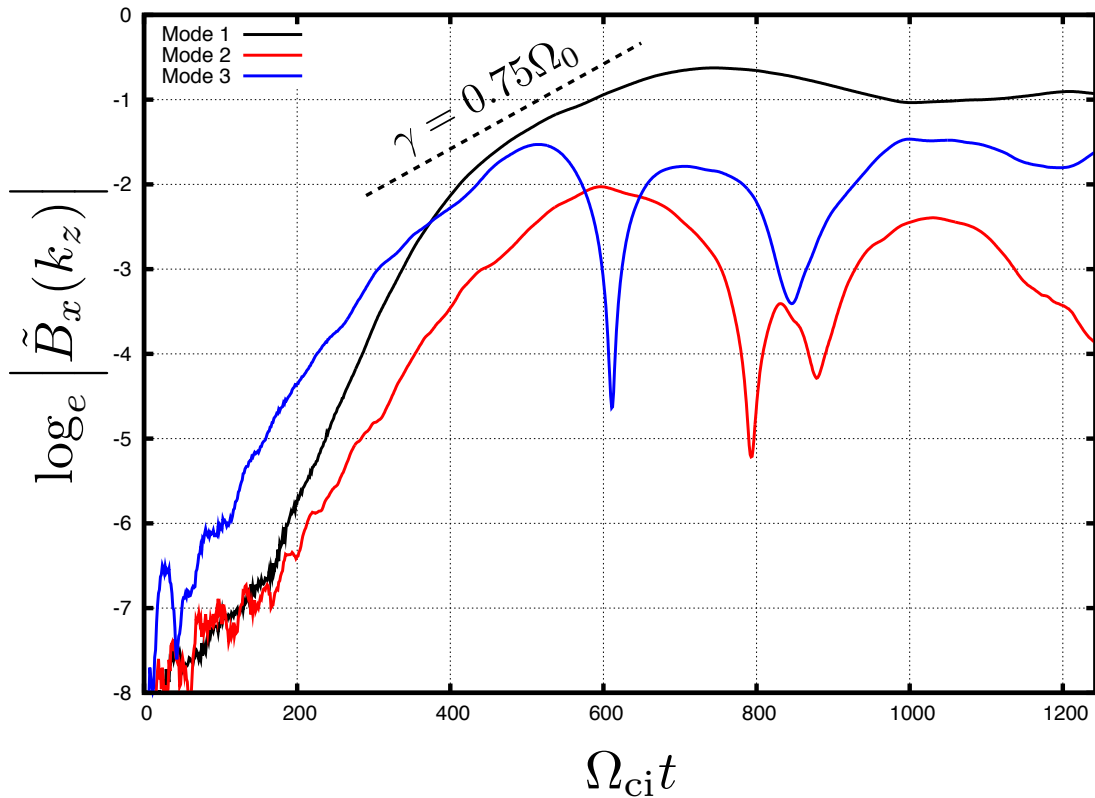


FIGURE 3.12: Time evolution of Magnetic field power calculated from RUN C2.

### 3.4 Summary and Discussions

In this chapter we investigated the effect of the differential rotation on the evolution of the magnetic reconnection with five consecutive runs. The initial magnetic field imposed here was parallel to the rotational axis, and the Keplerian shear flow was imposed in perpendicular direction.

Main results are summarized as follows: First we found an asymmetric structure in the out-of-plane magnetic field in the vicinity of the X-point. This can be understood by the coupling of the Hall term and the differential rotation. As the reconnection grows, Hall current around the X-point generates quadrupole magnetic field. At the same time, the perpendicular magnetic field generated by the magnetic reconnection is sheared by the differential rotation generating a dipole

structure in the out-of-plane magnetic field. The asymmetry is created as a superposition of these two processes. Furthermore, we also confirmed the “undulated” structure reported in Arzner and Scholer [2001]. Here, the differential rotation seems to have a minor effect on the generation of the “undulated” structure.

Next we found a migration of the X-point. This can be interpreted as a result of the MRI evolution coupled with the magnetic reconnection under the Hall effect. Since we have taken the Hall effect into account, the instability criteria of the MRI is different between the opposite sides of the neutral sheet. The particular side of the outside of the current sheet region has a reduced criteria of the MRI, whereas the other one has a severer criteria. Since a small scale perturbation given by the magnetic reconnection would couple with the MRI under the Hall effect in the particular side of the current sheet, the perturbation imposed by the magnetic reconnection would be enhanced in an asymmetric manner. This asymmetry in a growth of the MRI would result the migration of the X-point and its direction is determined only by the initial sign of  $\mathbf{J}_0 \times \boldsymbol{\Omega}_0$ . We consider this process is also effective in the presence of guide field since the growth rate of MRI differs with the opposite sign of Hall parameter even in the presence of a guide field (Balbus and Terquem [2001]).

Finally we found that the migration of the X-point can be a trigger of the MRI and can modify the characteristic scale of the perturbation. Since the magnetic field decreases inside the current sheet, MRI is active in this region. Due to the X-point migration, relatively large  $B_x$  is generated. This can effectively couple to MRI in the current sheet, and can be an effective trigger of MRI. It should be noted that this process is also effective even when the outside the current sheet region is stable to MRI. Once the magnetic reconnection is activated, annihilation of the axial magnetic field occurs and the critical wavelength of MRI will be shifted to shorter wavelength from the vicinity of the current sheet. As this process continues the entire system evolves to a MRI driven structure, such as a set of channel flow.

It is well known that during the quasi steady state of the MRI induced turbulence, the magnetic energy is enhanced intermittently and released within a short time scale. During this stage a disruption and a re-organization of the channel flow take place repeatedly and a magnetic reconnection plays an important role on the dissipation of the magnetic field and heating of plasma. This process generates spike structures in the time evolution of the Maxwell stress curve during the quasi steady state (Sano and Inutsuka [2001]). It has also been pointed out from 2.5D PIC simulations that during the “active” phase when the magnetic reconnection takes place repeatedly the efficiency of the angular momentum transport increases (Hoshino [2013]). As discussed in Chapter 2 the rapid growth of  $\alpha$  due to the strong dynamo effect of MRI and rapid decrease related to the magnetic reconnection was observed in our hybrid simulation as well. These results imply that the repeating process of magnetic energy enhancement by the MRI and dissipation by the magnetic reconnection is essential to an effective angular momentum transport. Though our initial setting is limited in the specific structure of the current sheet, we consider that the “triggering” effect of magnetic reconnection would be an effective seed of a re-organization of the current sheet accompanied to the channel flow and as a result, contributes to a strong angular momentum transport in the collisionless accretion disk. As we have looked in Chapter 2, the most effective stress component which contributes to the angular momentum transport was Maxwell stress (Figure 2.8). Therefore, large perturbation on the  $B_x$  given by the migration of X-point would act as an effective reproduction of Maxwell stress after the magnetic reconnection. Though several hundreds of ion inertia scale is still be smaller than the actual scale of the disk, we believe that the results of the this chapter would be non-negligible in the thick current sheet.

As we have seen in Chapter 2, the azimuthal component of the magnetic field ( $B_y$ ) is rather dominant in the non-linear state of MRI. Therefore, it should be noted that not only the 2.5D meridional plane analysis but also the equatorial ( $x, y$ ) plane analysis would be important for the understanding of the fundamental

physics of the magnetic reconnection in the differentially rotating system. In the next chapter, we will introduce an evolution of the magnetic reconnection in the equatorial plane of the disk.

## Chapter 4

# Magnetic Reconnection in the Equatorial Plane of the Disk

In the previous chapter we have investigated the evolution of magnetic reconnection in the meridional plane of a differentially rotating disk. We found that the coupling between MRI under the effect of Hall term and magnetic reconnection triggers asymmetric structure of X-point and as a result, the X-point migrates in the specific direction determined by the initial direction of the neutral sheet current and rotation vector.

As we have pointed out in Chapter 2, in non-linear stage of MRI, equatorial component of sheared magnetic field becomes significant. In this point of view magnetic reconnection in the equatorial plane of the rotating disk would also be important as a fundamental process to dissipate the magnetic energy. In addition, by transforming the magnetic energy to kinetic energy of the plasma, magnetic reconnection can also be important in the context of generation of turbulence in the disk.

Evolution of magnetic reconnection in the parallel shear flow is studied by several researchers for an application to the magnetic reconnection in the boundary of the earth's magnetosphere (e.g., La Belle-Hamer et al. [1994]). Major results of

the past studies were the formation of the asymmetric structure and the reduced reconnection rate (e.g., Chen et al. [1997]).

In the previous studies the background shear flow was relatively strong since in the magnetopause, the velocity of the shear across the current sheet reaches to sub-Alfvénic to super-Alfvénic. In addition since the past numerical studies adopted free boundary conditions, the evolution of the system was basically focused on the evolution of single X-point.

In this chapter we carry out another series of simulation studying the evolution of magnetic reconnection in the equatorial plane of the disk whose initial field is aligned to a background shear flow. The configurations of the setups are almost the same as those in the past studies. However, since we focus on the local behavior of differentially rotating disk, open shearing periodic boundary condition (Hawley et al. [1995]) is adopted. Moreover relatively small values of shear rate compared to the previous studies are assumed. Since we have adopted “periodic” boundary condition in the present study, the evolution of the magnetic reconnection in our study is no longer restricted in the single X-point evolution. We found that under the certain value of the shear rate, reconnection rate is enhanced. We consider this enhancement is a result of interaction with the multiple X-point and newly found as a result of the periodic boundary condition.

## 4.1 Introduction

In Chapter 3, we have investigated non-linear evolution of magnetic reconnection in the meridional plane of the disk. The initial direction of the magnetic field outside the current sheet region was set to be parallel (anti-parallel) to the rotational axis. However, as we have introduced in Chapter 1, azimuthal component of the magnetic field is dominant in the non-linear state of MRI. In the equatorial plane, background Keplerian shear flow itself is important on the evolution of the magnetic reconnection, because the direction of the shear flow given by the

Keplerian rotation and that of the vortexes generated by magnetic reconnection are in the same plane. With this configuration, inflow and outflow generated in the magnetic reconnection is expected to be affected by Coriolis force and tidal force. Based on these motivation we will investigate the evolution of magnetic reconnection in the equatorial plane of the disk in this chapter.

Evolution of magnetic reconnection with a shear flow along the ambient magnetic field has been studied in the context of magnetopause reconnection. Magnetic reconnection in the earth's magnetopause involves a strong flow shear between the magnetospheric plasma and magnetosheath plasma (Gosling et al. [1986]). In the past, evolution of the magnetic reconnection with the background parallel shear flow was studied using MHD code (La Belle-Hamer et al. [1994]; La Belle-Hamer et al. [1995]), and hybrid code (Xie and Lin [2000]). Related to the parallel shear flow, interaction between tearing mode (Furth et al. [1963]) and Kelvin-Helmholtz instability (Chandrasekhar [1961]) was also studied using MHD code (Chen et al. [1997]). Due to the background shear flow along the current sheet, the asymmetric structure with respect to the X-point was observed in the non-linear stage of the calculation. Theoretical background was later revealed by Cassak and Otto [2011] who derived the scaling law of the reconnection rate in the shear flow. Together with the numerical simulation Cassak [2011] reported that the reconnection rate is reduced with the increasing rate of flow shear. They have concluded that the background shear flow reduces the magnetic tension force of the reconnected field resulting a slower outflow velocity. In addition, since the outflow feels head-on wind at the certain side of the neutral sheet and following wind on the opposite side, the dynamic pressure which the outflow feels differs in the each side of the neutral sheet. As a result, both the structure near the X-point and the outflow becomes tilted (see Figure 1.8).

The past studies are mainly focused on the magnetopause, and interaction between tearing mode and Kelvin-Helmholtz instability was the central interest. Therefore

in the previous studies  $\tanh(x)$  types of the flow profile was imposed. In addition the rate of the flow shear was relatively strong compared to that of Kepler rotation, and the parameter range in the past studies lied around sub-Alfvénic to super-Alfvénic shear flow. In those studies the shear flow was found to stabilize the tearing mode. In the  $\tanh(x)$  type shear flow, the rate of the shear is concentrated in the current sheet region. Here as we aim to study the local evolution of the disk, we have to consider a uniform shear flow lying on the entire region of the simulation domain.

From the numerical point of view, one must take care the boundary condition for the inflow boundary, since in this setup periodicity does not hold due to the background shear flow. In the previous studies free boundary condition (La Belle-Hamer et al. [1994]; La Belle-Hamer et al. [1995]; Chen et al. [1997]; part of Cassak [2011]) or periodic boundary condition by putting two shear layer just as like double-Harris sheet (Cassak [2011]) are mainly used. These types of boundary condition appropriately describes an evolution of single X-point. However as we focus on the local evolution of the differentially rotating disk, simulation adopting periodic boundary condition would describe a local behavior of the disk in more appropriate manner.

Since in Chapter 2 and Chapter 3, we were carrying out the calculation in the meridional plane of the disk the boundary condition was degenerated to an ordinary periodic boundary condition for deviation from the Keplerian component. In this chapter instead, we have to consider a derivative aligned to the initial shear. And as the shear flow exists even in the boundary of the domain, we must take the effect of shear into account while taking the boundary condition of the radial direction. This type of boundary condition, which is so-called open shearing periodic boundary condition (Hawley et al. [1995]) has been widely used in a local simulation of the 3-dimensional evolution of MRI (e.g., Stone et al. [1996]) under the MHD framework. In the case of hybrid code, Kunz et al. [2014a] have adopted this boundary condition on the study of firehose and mirror instability which is driven by self generated pressure anisotropy due to the background shear flow. In

their study, relatively weak shear was adopted and also, Coriolis and tidal force were neglected.

In this chapter, by carrying out hybrid simulation in equatorial plane, we investigate the collisionless magnetic reconnection in differentially rotating system. Together with the result of Chapter 2 and 3 investigation of the basic structure of anti-parallel magnetic field in differentially rotating disk will be completed. Since the ambient field and the Keplerian shear flow is aligned in this chapter, the shear flow might be regarded as dominance of pressure parallel to the magnetic field, which would decrease the growth rate of tearing mode instability. At the same time, once the reconnection starts, the inflow/outflow generated by the reconnection will couple with Coriolis force and this might modify the feature of magnetic reconnection. By carrying out hybrid simulation in the equatorial plane these effects, especially the former effect can be taken into account. It should also be noted that numerically, this simulation will be an important step for the implementation of open shearing periodic boundary condition in gravitationally supported shear flow in the hybrid framework.

## 4.2 Basic Equations and Setup

### 4.2.1 Basic Equations

For the simulations carried out in this chapter, the basic equations are the same those introduced in Chapter 2. In contrast to the calculations in Chapter 3, finite electron mass was included mainly to reduce numerical noise seen in the boundary and keep a stability of the calculations. The mass ratio  $m_i/m_e$  was set to be 16, and we have neglected the advection term  $\propto \mathbf{V}_e \otimes \mathbf{V}_e$  in the calculation of electric field,

$$\frac{d\mathbf{x}_i}{dt} = \mathbf{v}_i \tag{4.1}$$

$$q_i = -q_e \quad (4.2)$$

$$n_i = \sum_{\text{particle}} S(\mathbf{x}_i). \quad (4.3)$$

$$n_e \simeq n_i \quad (4.4)$$

$$\mathbf{J}_i = q_i \sum_{\text{particle}} \mathbf{v}_i S(\mathbf{x}_i). \quad (4.5)$$

$$m_i \frac{d\mathbf{v}_i}{dt} = q_i \left( \mathbf{E} + \frac{1}{c} \mathbf{v}_i \times \mathbf{B} \right) - 2m_i \boldsymbol{\Omega}_0 \times \mathbf{v}_i - 2m_i q \Omega_0^2 x \mathbf{e}_x \quad (4.6)$$

$$\frac{\partial \mathbf{B}}{\partial t} = -c \nabla \times \mathbf{E}. \quad (4.7)$$

$$\hat{\mathbf{E}} = -\frac{1}{c} \mathbf{V}_e \times \mathbf{B} + \frac{\nabla P_e}{n_e q_e} \quad (4.8)$$

$$\frac{q_e^2 n_e}{m_e} \hat{\mathbf{E}} = \frac{1}{4\pi} (\omega_{pe}^2 - c^2 \nabla^2) \mathbf{E} \quad (4.9)$$

$$\mathbf{J} = q_e n_e \mathbf{V}_e + \mathbf{J}_i = \frac{c}{4\pi} \nabla \times \mathbf{B} \quad (4.10)$$

$$\nabla \cdot \mathbf{B} = 0 \quad (4.11)$$

$$P_e \propto n_e^\gamma. \quad (4.12)$$

As introduced in the previous chapters, we adopt  $q = -3/2$  and  $\gamma = 5/3$ .

## 4.2.2 Initial Condition

We first describe initial conditions imposed in the calculations. As an initial equilibrium, we put double Harris sheet (Harris [1962]) along the  $y$ -direction. In contrast to the equilibrium field we used in the previous chapter, we put a current sheet on the center of the simulation domain to calculate the evolution on the co-moving frame of the X-point of the reconnection

$$B_{y0}(x) = B_0 \left[ \tanh \left( \frac{x - x_c}{l} \right) - \tanh \left( \frac{x - x_1}{l'} \right) - \tanh \left( \frac{x - x_N}{l'} \right) \right]. \quad (4.13)$$

Here  $l' (= 2l)$  is the half width of the current sheet located in the boundary of the simulation domain. For  $l$ , we took a same value as we used in Chapter 3 ( $l = 1.8\lambda_i$ ).  $x_1, x_N$  represents the inner and outer boundary of the simulation box

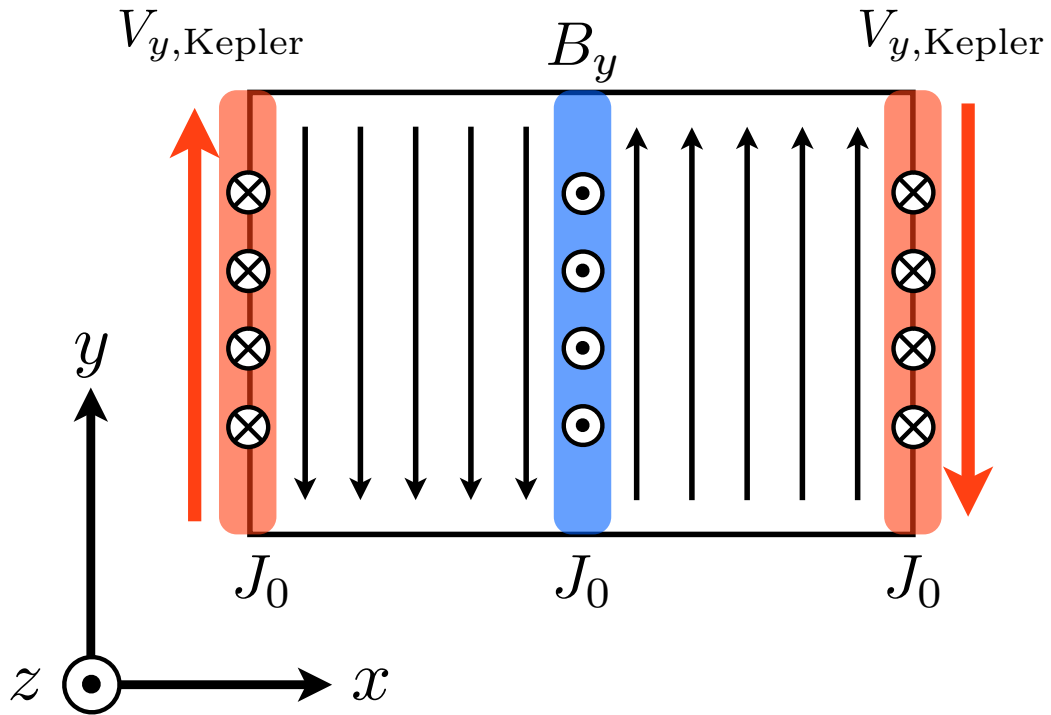


FIGURE 4.1: Schematic illustration of the simulation setup calculated in this chapter.

and  $x_c(= L_x/2)$  represents the center of the simulation box. We have located the current sheet in the center of the simulation domain for two reasons. One is to keep the X-point in the stationary point. Since we set the corotation point in the center of the simulation domain, the relative velocity of the shear flow is zero at this point and the X-point keeps its initial location. Another reason is related to the boundary condition which is introduced in Appendix B. We have paid a great attention to a boundary condition for  $x$ -direction but our simulation code is still unstable to large rotational parameter ( $\Omega_0/\Omega_{ci} \gtrsim 0.01$ ). The numerical noise generated in the boundary can be reduced by setting the field value to be small in the boundary. For stable calculation, we set an initial position of the current sheet on the boundary, and we also set the thickness of the current sheet on the boundary to be twice as thick as the one located on the center. We assumed uniform temperature ions and the number density of the ions are given so as to

satisfy the pressure balance,

$$n_i(x) = n_0 + n_c \left[ \cosh^{-2} \left( \frac{x - x_c}{l} \right) + \cosh^{-2} \left( \frac{x - x_1}{l'} \right) + \cosh^{-2} \left( \frac{x - x_N}{l'} \right) \right]. \quad (4.14)$$

As we will introduce in the following sections, no migration of the X-point was observed. Therefore, in contrast to Chapter 3 we assume that the  $x$ -coordinate of the current sheets and the center of the anomalous resistivity is fixed in their initial position. For velocity distribution of the ions, we adopt a shifted Maxwellian distribution with constant ion temperature,

$$f_i(\mathbf{x}_i, \mathbf{v}_i) = n_i \left( \frac{m_i}{2\pi T_i} \right)^{3/2} \exp \left[ -\frac{m_i}{2T_i} \{v_x^2 + (v_y - v_{Ky}(x))^2 + (v_z - v_{d,i})^2\} \right]. \quad (4.15)$$

The definition of  $v_{d,i}$  is given in 3.13. Like we did in Chap.3, we adopt localized perturbation and localized resistivity to save the integration time on the central current sheet, using the form introduced in Zenitani et al. [2011],

$$\delta A_y = -2lB_1 \exp \left[ -\frac{(x - x_c)^2 + (y - y_c)^2}{(2l)^2} \right] \quad (4.16)$$

$$\eta = \eta_0 + \eta_c \cosh^{-2} \left[ \left( \frac{x - x_c}{0.5\lambda_i} \right)^2 + \left( \frac{y - y_c}{\lambda_i} \right)^2 \right], \quad (4.17)$$

Here  $B_1$  was set to be  $0.15B_0$  and the magnetic Reynolds numbers defined with  $\lambda_i V_{A0}/\eta_0$  and  $\lambda_i V_{A0}/\eta_c$  are set to be 2000 and 100, respectively.  $y_c (= L_y/2)$  is the  $y$ -position of the initial perturbation. In contrast to the simulations in Chapter 3 we trigger reconnection only in the center of the domain. The other important parameters are shown in Table 4.1.

### 4.2.3 Boundary Condition

In this calculation, so-called open shearing periodic boundary condition (Hawley et al. [1995]) is used to take the effect of the background shear flow into account.

TABLE 4.1: Simulation Parameters for magnetic reconnection in the equatorial plane of the disk.

	RUN A	RUN B	RUN C	RUN D	RUN E
$L_x \times L_y$	$180 \times 480$	$180 \times 480$	$180 \times 480$	$180 \times 480$	$180 \times 480$
$\lambda_i$	$2\Delta x$	$2\Delta x$	$2\Delta x$	$2\Delta x$	$2\Delta x$
$N_{\text{ppc}}^1$	135	135	135	135	135
$n_c/n_0$	4	4	4	4	4
$\beta_{i,\text{Out}}$	1.0	1.0	1.0	1.0	1.0
$p_e/p_i$	$5 \times 10^{-3}$	$5 \times 10^{-3}$	$5 \times 10^{-3}$	$5 \times 10^{-3}$	$5 \times 10^{-3}$
$\Omega_0/\Omega_{\text{ci}}$	0	$3.33 \times 10^{-4}$	$1.25 \times 10^{-3}$	$2.00 \times 10^{-3}$	$2.00 \times 10^{-2}$
$m_i/m_e$	16.0	16.0	16.0	16.0	16.0

This boundary condition is commonly used in the MHD calculation of the differentially rotating disk. For the particle based code, simulation using this boundary condition with simple shear flow (i.e., without Coriolis and tidal force) is reported by Kunz et al. [2014a] who investigated the spontaneous growth of mirror and firehose instability in the shear flow using hybrid code. In the ordinary periodic boundary condition, one would only assume that completely same structures (let us call this “ghost domain”) exist in the outside of the each boundary. In contrast, when the shear flow exists, these structures outside the boundary are convected due to this flow with the absolute velocity of  $|q\Omega_0 L_x|$ . Resulting boundary condition for physical value  $f$  at  $t = t_1$  becomes,

$$f(x, 0) = f(x, L_y) \quad (4.18)$$

$$f(0, y) = f(L_x, y - q\Omega_0 L_x t_1) \quad (4.19)$$

$$f(L_x, y) = f(0, y + q\Omega_0 L_x t_1). \quad (4.20)$$

Details about this boundary condition, and implementation to the hybrid code is introduced in Appendix B.

---

<sup>1</sup>At the outside of the current sheet region.

## 4.3 Results

### 4.3.1 Asymmetric Evolution of Magnetic Reconnection

Due to the Keplerian shear flow, evolution of magnetic reconnection in the equatorial plane shows different features compared to those on the meridional plane. Figure 4.2 shows the time evolution of the magnetic field line and the density profile. From the fourth panel of the figure, the asymmetry in the vicinity of the X-point is clearly observed in all runs with shear flow. The break of symmetry itself is also observed in the meridional plane case (see Chapter3). In the meridional plane, the asymmetry was found with respect to the current sheet. In contrast, the break of symmetry is found with respect to the X-point here but no migration of the X-point in the equatorial plane was seen.

Related to the break of asymmetry in the vicinity of the X-point, the structure around the X-point becomes tilted. Comparing RUN B,C and E, the tilt seems to grow counter-clockwise in the smaller rotational parameter (RUN B, C) and clockwise in the larger rotational parameter (RUN E). Let us first discuss the source of the tilt for the larger rotational parameter (RUN E) case.

#### **Asymmetry in Large Rotational parameter (RUN E)**

For RUN E case, the relation between the direction of the shear flow and the direction of the tilt is consistent with those of the past studies (e.g., La Belle-Hamer et al. [1994]; La Belle-Hamer et al. [1995]). The source of the tilt proposed in the past studies are understood as a difference between the dynamic pressure which the outflow feels, and outflow is tilted to the side where the direction of shear flow and outflow is anti-parallel.

In addition to this process reported in the past, there is another mechanism to enhance the tilted structure. In our calculation we also took Coriolis and tidal forces into account. The resulting difference appears in the radial ( $x$ -direction)

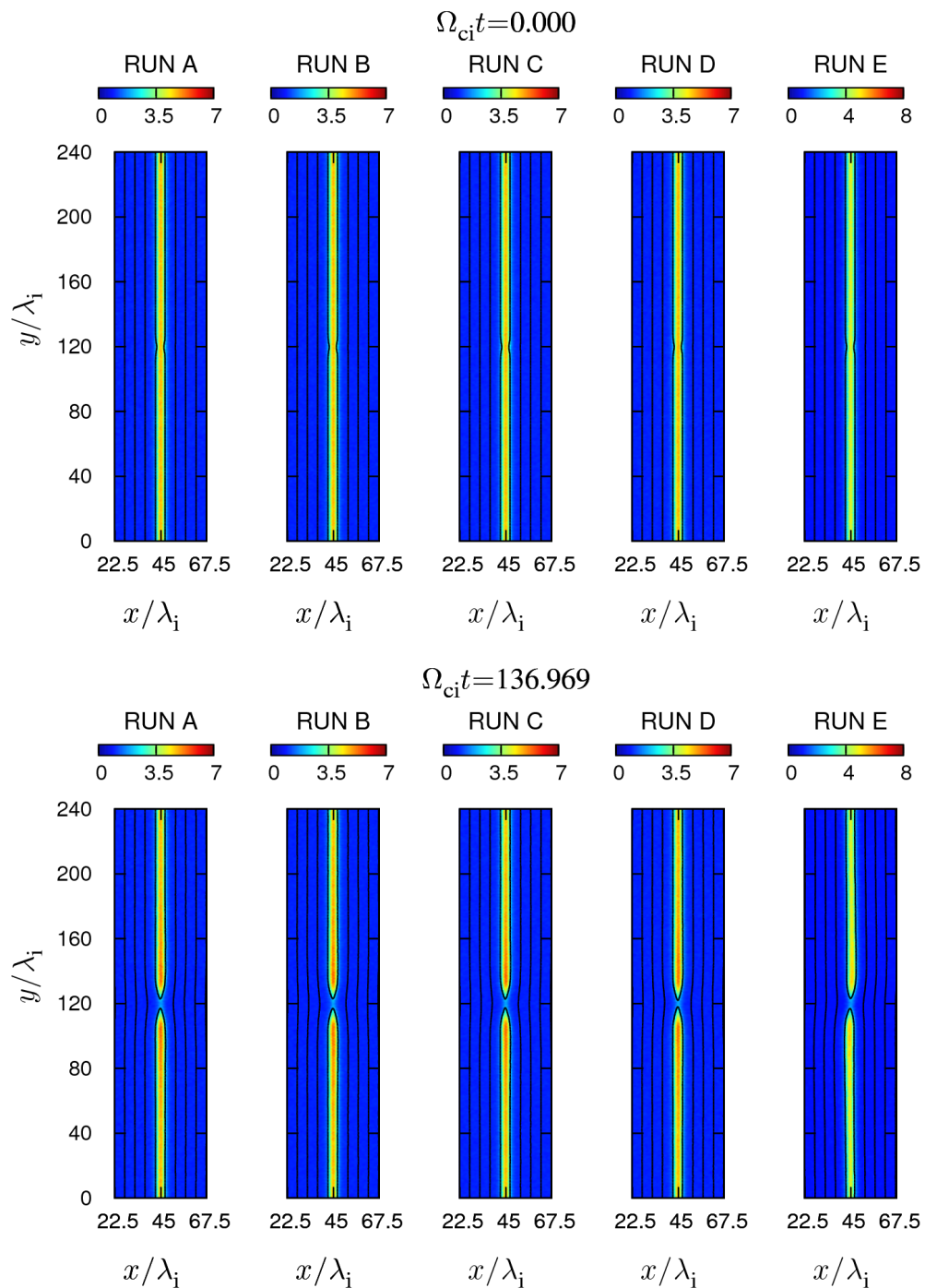
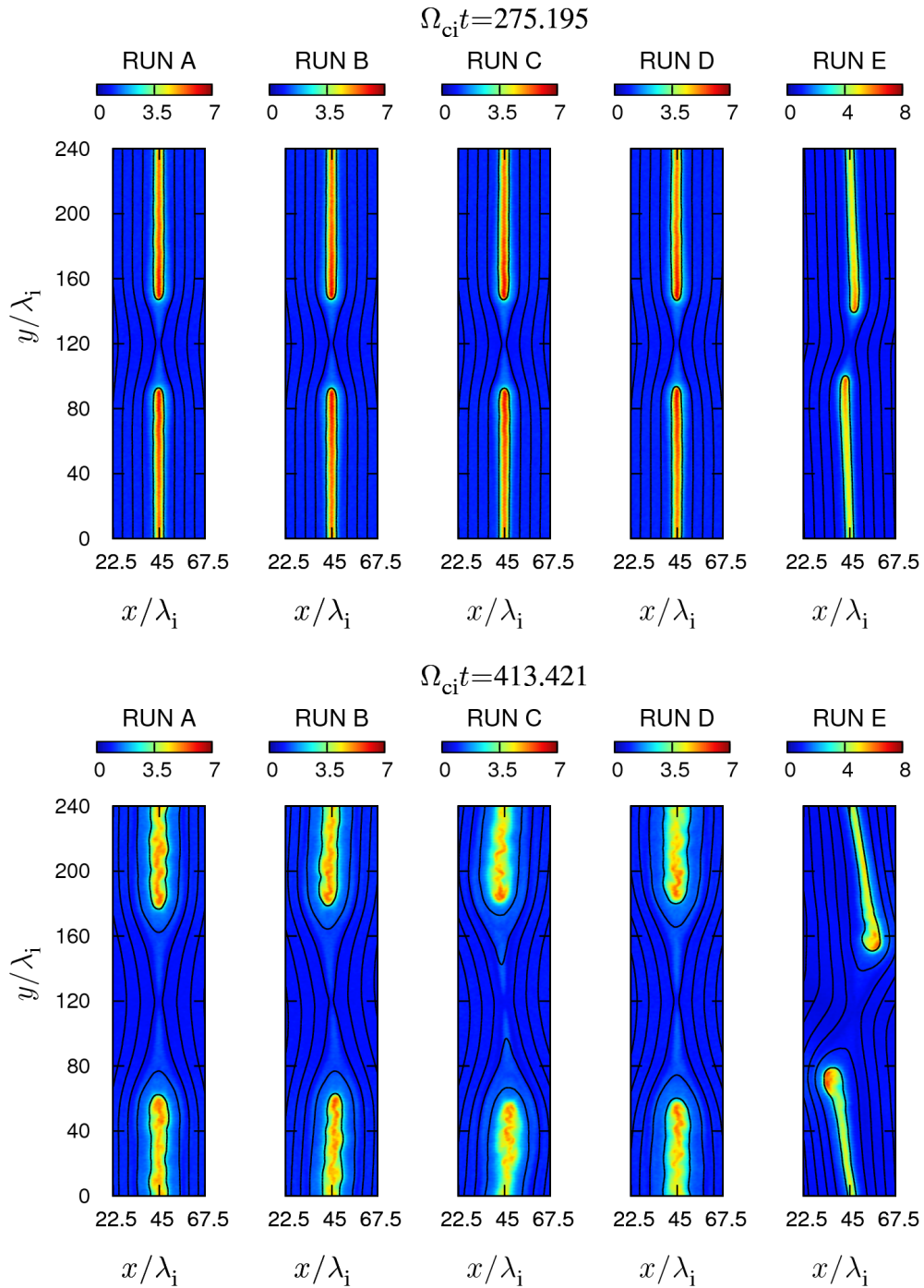


FIGURE 4.2: Time evolution of runs on the equatorial plane. Color contour corresponds to ion density whereas the solid line corresponds to the magnetic field line. The figures are focused on the central current sheet in which the localized resistivity and the initial perturbation are imposed.



velocity. Figure 4.3 shows radial bulk velocity profiles of ions at the  $\Omega_{\text{ci}}t \simeq 275$  in all runs. As we can see from the figure, significant radial velocity comparable

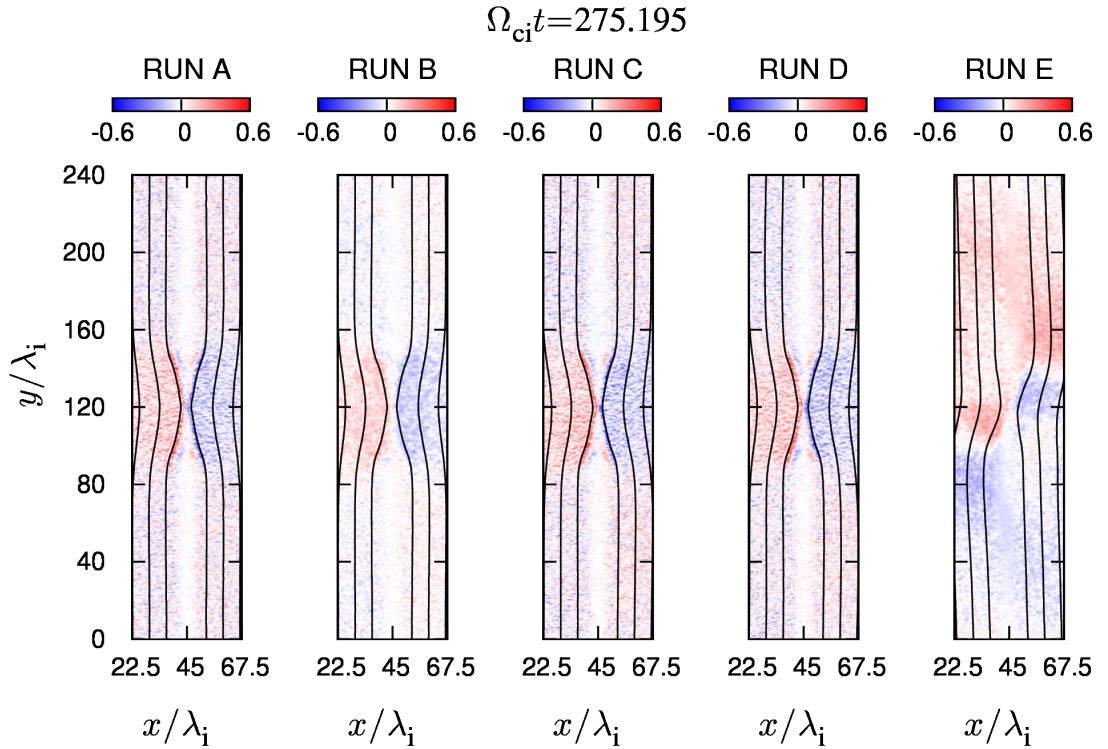


FIGURE 4.3: (Color) Radial ( $x$ -direction) component of the ion bulk velocity in the unit of Alfvén velocity defined in the initial parameter in the out of the current sheet region.

to the Alfvén velocity is observed in the outflow region in RUN E. In our setup, the reconnection jet is initially ejected to  $\pm y$ -direction which is aligned to the azimuthal direction. As a result, Coriolis force  $-2\boldsymbol{\Omega}_0 \times \mathbf{V}_{y,\text{jet}}$  produces  $\pm x$ -direction velocity in the outflow region. Since the magnetic reconnection continuously drives  $y$ -direction jet with the order of Alfvén velocity, the magnitude of the radial velocity in the outflow region will reach to sub-Alfvénic velocity. The direction and the magnitude of the velocity is also confirmed from Figure 4.3.

Comparing our results to those of the past studies, the effect of Coriolis force on the tilted structure seems to be significant in this parameter. Though our background shear profile has linear profile and is different from the profile used in the past studies, we can roughly compare the magnitude of the shear from the change in

the azimuthal velocity across the current sheet. In RUN E of our simulation this difference ( $\Delta V_y$ ) is estimated as,

$$\Delta V_y = |q|\Omega_0 (2l) = 0.216V_A. \quad (4.21)$$

This value is approximately half the magnitude compared to the smallest shear parameter adopted in Cassak [2011]. Comparing the tilt angle, the angle obtained in Cassak [2011] was less than  $2^\circ$ . By detecting the  $x$ -position of the neutral sheet at  $y = 80\lambda_i, 160\lambda_i$ , we have also estimated the tilt angle in our simulation. The estimated tilt angle at  $\Omega_{ci}t \simeq 413$  was roughly  $10^\circ$  which is remarkably larger than the past studies, implying the significance of the Coriolis force on the evolution of the X-point structure.

### **Asymmetry in Small Rotational parameter (RUN B,C)**

Now let us look on to the smaller rotational parameter case (RUN B, C). These two cases have the opposite tilt angle compared to RUN E implying another process is driving the generation of the tilt. We consider this is a result of the periodic boundary condition which we have newly adopted in our simulation. Figure 4.4 and Figure 4.5 show schematic illustrations using the density profile from RUN A and C calculations at  $\Omega_{ci}t \simeq 413$ . Since we are adopting the periodic boundary condition, the flow patterns take the form as if the X-point also exists in the inner and outer side of the actual simulation domain. In RUN A, which has no background shear motion, the inflow generated by the reconnection takes symmetric structure with respect to the current sheet we have imposed in the initial condition, and the total pressure is balanced in the both sides of the current sheet imposed in the boundary of the actual simulation domain. As a result, O-point is formed in the neutral sheet which is imposed in the boundary. When the background differential rotation exists, this “ghost” X-point travels along the  $\pm y$ -direction. In the case of  $\Omega_{ci}t \simeq 413$  of RUN C, the ghost X-points travels roughly  $70\lambda_i$  due

to the background shear motion. As a result, at the outflow region of the actual simulation domain, pressure gradient due to the rarefaction grows with an asymmetric manner, and the direction of the pressure gradient is opposite between the X-point. As a result, the O-points in the actual simulation domain move due to this pressure gradient and the tilt of the X-point is generated.

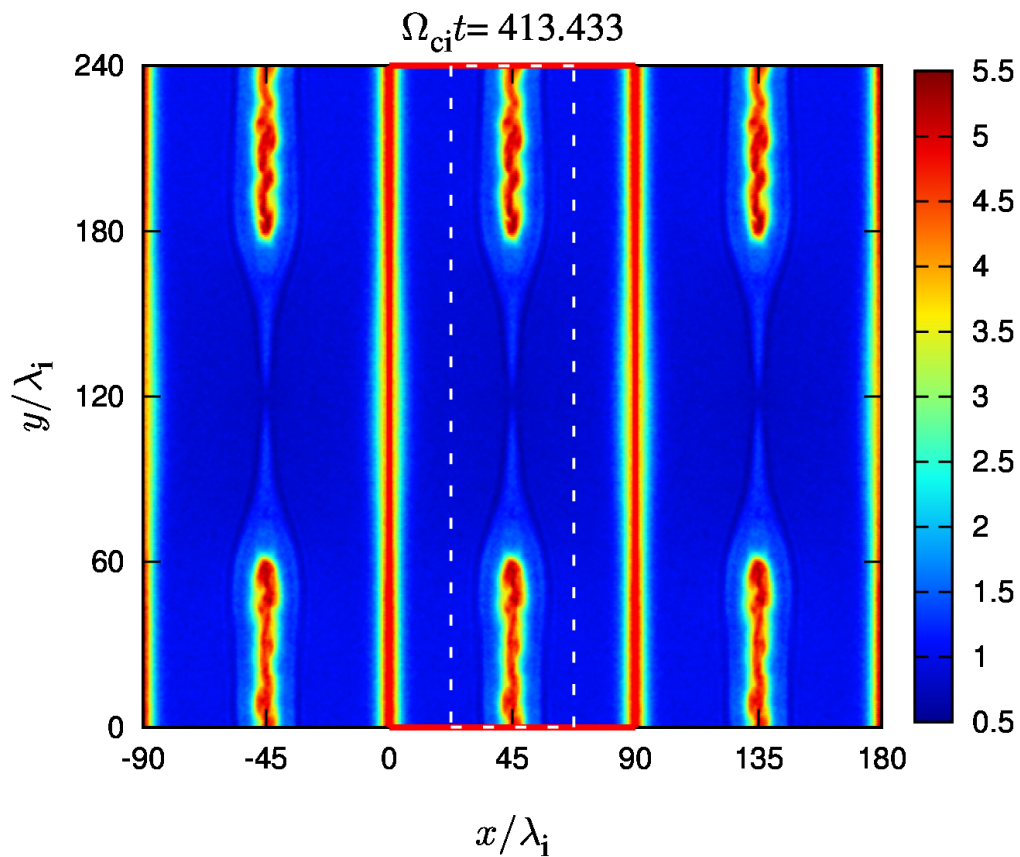


FIGURE 4.4: Schematic plot of RUN A including the “inner” and “outer” side of the actual simulation domain. The red box with solid line indicates the actual simulation domain we are calculating, whereas the white box with dashed line indicates the region we are showing in Figure 4.2

On the other hand, in the case of RUN E with the faster rotation, the displacement of the ghost X-point by the shear is roughly  $1.12 \times 10^3$  and the ghost X-point passes around the actual simulation domain for four times and the effect from the

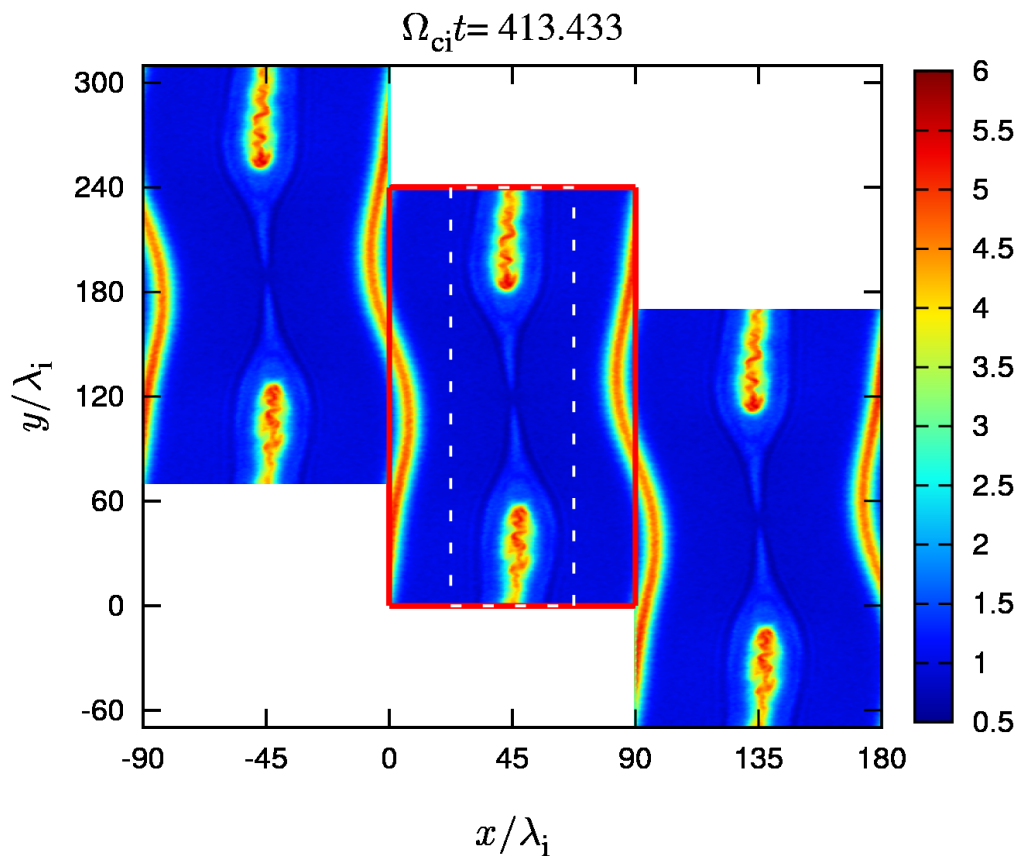


FIGURE 4.5: Schematic plot of RUN C taking the “shearing of the simulation domain” effect into account. The ghost domain in the inner boundary is sheared forward, whereas the ghost domain in the outer boundary is sheared backward. The red solid line indicates the actual simulation domain which we have calculated, and the white dashed line indicates the region shown in Figure 4.2.

background shear flow is somewhat averaged. In this case, the effect of the flow shear around the actual X-point and the effect of Coriolis force would be dominant. For RUN D, we consider these two competing process of the tilt is balanced and as a result, no significant tilt was observed.

### 4.3.2 Effect of the differential rotation on the reconnection rate

Another characteristic feature is also found from the reconnection rate. Figure 4.6 shows time evolution of reconnected flux ( $\Lambda$ ) for all runs. Unlike the ordinary, symmetric reconnection, neutral sheet is remarkably bent, and therefore, the length of the neutral sheet is not exactly the same with  $L_y$ . To take the curve of the neutral sheet into account, we define  $\Lambda$  by

$$\Lambda \equiv \frac{\int_C |B_n| dy}{B_{0y} \int_C dy} \quad (4.22)$$

where  $C$  is the path of the neutral point at given value of  $y$  and  $B_n$  is the local normal component of magnetic field with respect to the given path  $C$ . From Figure 4.6 we find that  $\Lambda$  increases as the rotational parameter increases.  $\Lambda$  takes the maximum value at  $\Omega_0/\Omega_{ci} = 1.25 \times 10^{-3}$  (RUN C) and turns to a decrease with larger rotational parameter.

#### Decrease of $\Lambda$ . Large rotational Parameter Case (RUN E)

Let us first discuss the decrease of  $\Lambda$  in RUN E. This is readily understood as a consequence of the background Keplerian rotation. In the corotating frame of Keplerian rotation Coriolis force drives the epicyclic motion in the plane. Therefore the radial flow initially driven by the reconnection acquire  $y$ -component velocity with  $\pi/2$  phase delay. This mechanism prevents a continuous motion of the plasma towards the X-point and decreases the efficiency of the reconnection. This feature is also confirmed from the left panel of Figure 4.3, whose inflow pattern is also titled in the clockwise direction. This feature is also understood as a result of the angular momentum conservation which disturbs the continuous radial transport of the plasma.

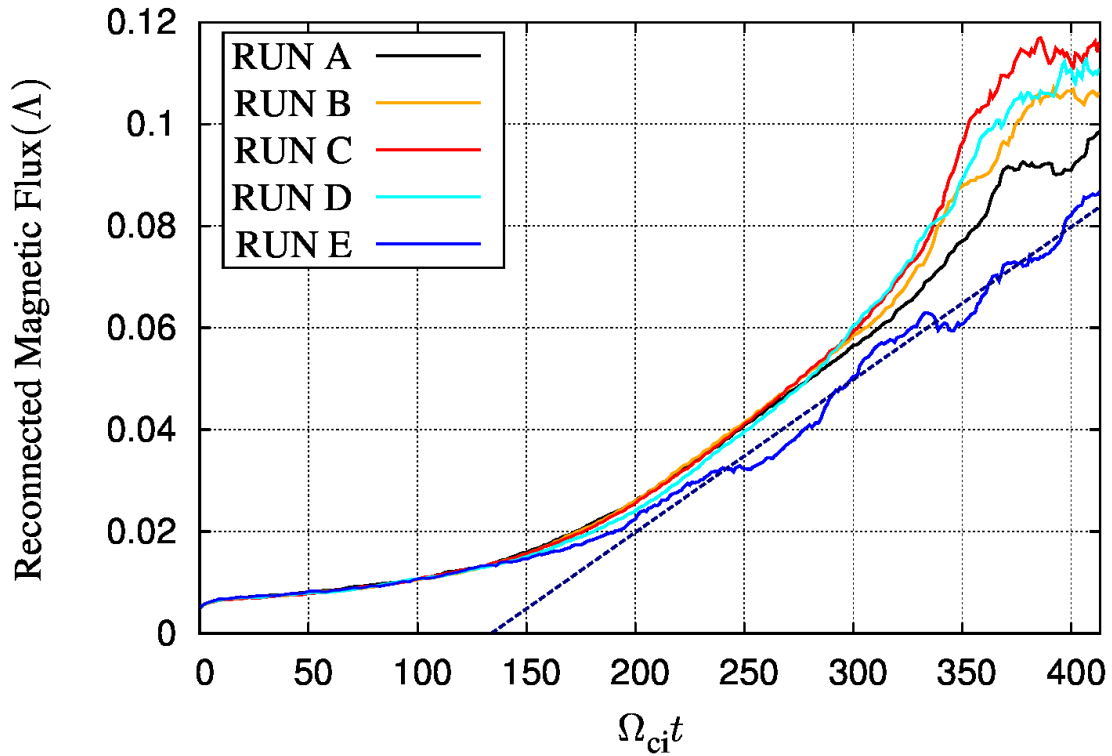


FIGURE 4.6: Time evolution of reconnected magnetic flux of five runs. The maximum reconnected flux is observed around  $\Omega_0/\Omega_{ci} \simeq 1.25 \times 10^{-3}$ . The dashed navy line corresponds to a fitting line obtained with least square method using flux data of RUN E from  $\Omega_{ci}t = 200 - 413$ .

#### Increase of $\Lambda$ . Small rotational Parameter Case (RUN B,C)

In contrast, increase of  $\Lambda$  in the smaller rotational parameter (RUN B,C) is not understood as a consequence of the differential rotation. This is understood by interaction between the multiple X-points. As we are now adopting a periodic condition for all boundaries, the flow pattern takes the form as if another X-point exists in the outside region of the actual simulation domain. Figures 4.4 and 4.5 show schematic illustrations of this feature. Without a shear flow, the X-point in the actual simulation domain and the X-points in the ghost domain remains in the same  $y$ -position. Once the shear is imposed, the X-point in the ghost domain is convected due to the shear and as a result, flow pattern is modified. In the case of RUN C, the X-point and the O-point in the neighboring domain is located alternately. With such a structure expansion of the O-points give a

driving flow of the reconnection to the X-point. At the same time, the rarefaction due to the inflow enhances the expansion of the O-point. This type of flow is well approximated by a driven reconnection (e.g., Horton and Tajima [1988]; Hoshino [1991]), and thus  $\Lambda$  is increased.

Looking on to the case of RUN E, the “sheared length” of the simulation domain at  $\Omega_{ci}t \simeq 413$  is approximately  $4.7L_y$ . In this case, the X-point in the neighboring domain passes its initial point repeatedly, and the effect of the convection by the shear on the neighboring reconnection site is averaged. As a result, Coriolis force effect became dominant in this run. However “driving effect” from the neighboring reconnection site is also seen in this run. Assuming that RUN E is at steady reconnection state at  $\Omega_{ci}t \gtrsim 200$ , we plot a fitting line obtained with least square method using reconnected flux data from  $\Omega_{ci}t = 200 - 413$  in RUN E (the dashed navy line in Figure 4.6). It is found that the reconnected flux is oscillating around the fitting line. The period of the oscillation is roughly  $90\Omega_{ci}^{-1}$ . Since the X-point in the ghost domain is sheared for  $4.7L_y$  in  $413\Omega_{ci}t$ , the estimated period is  $413/4.7 = 87.9\Omega_{ci}^{-1}$  which is consistent with the period of oscillation which is seen in the reconnected flux data of RUN E.

To confirm the above explanation, we carried comparative runs using RUN C as a fiducial parameter. In run labeled “C2”, we excluded Coriolis and tidal force term in the equation of motion (2.32). In this case, there is still a uniform shear flow parallel to the ambient magnetic field. In run labeled “C3” we have extended the  $x$ -direction box size to  $2L_x$  to make the effect from the neighboring current sheet smaller. Figure 4.7 shows a focused plot of the X-point at  $\Omega_{ci}t \simeq 413$  of comparative runs. As we can see from the figure, direction of the tilt in RUN C2 is the same with that in RUN C. In contrast, in RUN C3 which has larger box size, the direction of the tilt is the same as RUN E, on which the effect of the Coriolis force was dominant. These results are consistent with the understanding that the sheared X-point and modified flow pattern contributed to a asymmetric evolution of the X-point.

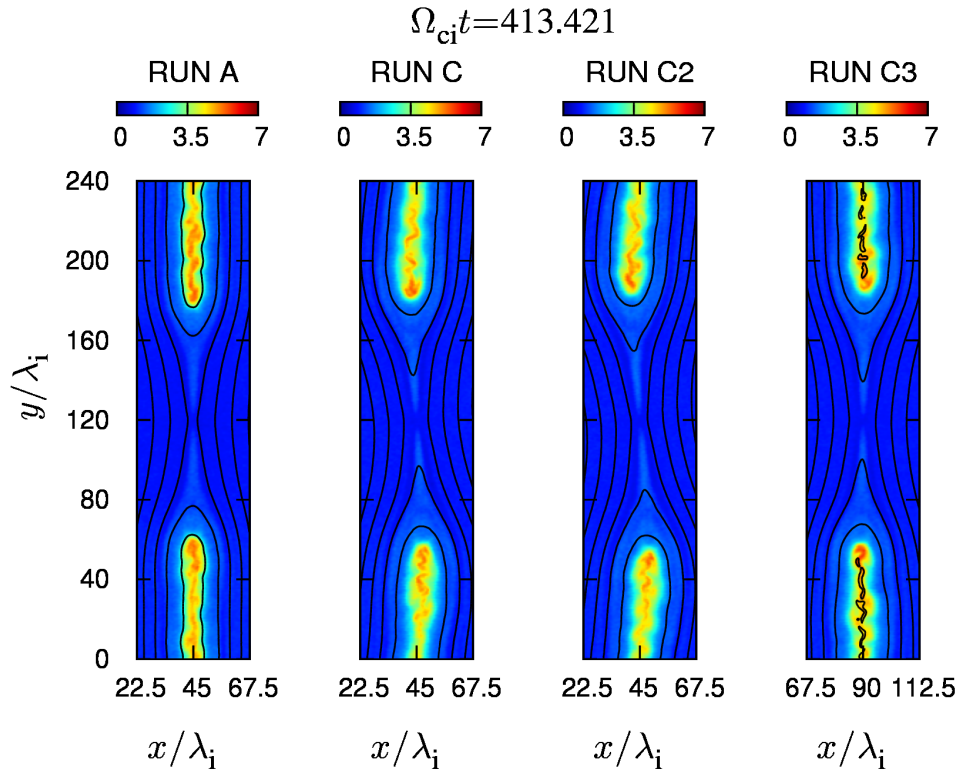


FIGURE 4.7: Ion density profile (color) at  $\Omega_{ci}t \simeq 413$  in comparative simulations. Solid line corresponds to magnetic field line.

Another evidence is found from the comparison of the reconnected magnetic flux. Figure 4.8 shows a time evolution of reconnected flux in RUN A, C, C2 and C3. Clearly, RUN C2 which has no Coriolis force shows a fastest reconnection rate. Since the Coriolis and tidal force are excluded, the conservation of angular momentum no longer disturbs inflow, and faster reconnection rate compared to RUN C is attained. On the other hand, in RUN C3, the reconnection rate was smaller compared to that of RUN C. Since we have set a wider interval between each current sheets, the effect from the ghost X-point is weakened. As a result, the conservation of angular momentum becomes more effective in this run, and the rate was decreased.

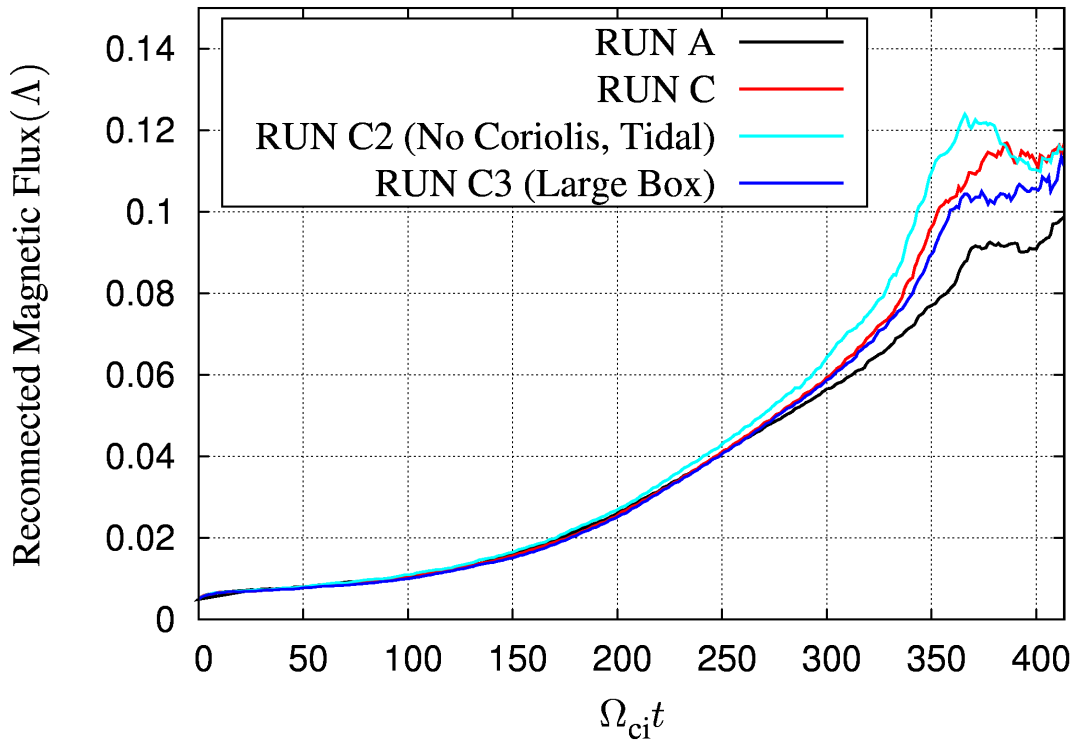


FIGURE 4.8: Time evolution of reconnected magnetic flux of comparative runs. The case with no Coriolis and tidal force has the maximum growth rate.

## 4.4 Summary and Discussion

In this chapter, we have investigated evolution of magnetic reconnection in the equatorial plane of differentially rotating disk. In this plane, shear flow parallel to the ambient magnetic field was important on the evolution of the reconnection. The setup putting the parallel shear flow itself was investigated by several researchers who focused on the reconnection in the magnetopause (e.g., La Belle-Hamer et al. [1994]; La Belle-Hamer et al. [1995]; Chen et al. [1997]).

In contrast to the previous studies, our simulation focused on the local behavior of the disk. Therefore, the shear rate we have used in our calculations were much smaller than those used in the previous studies. In addition, we have implemented the open shearing boundary condition (Hawley et al. [1995]). Therefore the reconnection site in the actual domain interacts with neighboring reconnection site

in the “ghost domain”. In addition, since we have aimed to study the evolution of rotational system supported by a central massive star, we have included the Coriolis and tidal force.

With the large rotational parameter, major results was consistent with those from the previous studies. The X-point evolved asymmetrically due to the shear motion and the relation between the direction of the shear and the tilt angle was the same as those observed in La Belle-Hamer et al. [1994]. Compared to the previous studies, Coriolis force was found to be more effective for the evolution of asymmetric structure. Reduced value of reconnection rate due to the strong shear was also consistent with the results from Cassak [2011] in this parameter. Since we have applied the different shear profile and boundary condition compared to the previous studies, we conclude that the tilt of the X-point and reduced reconnection rate is a general feature found in magnetic reconnection with strong parallel shear. In addition, we have confirmed that the conservation of the angular momentum about the central star will disturb the inflow and reduces reconnection rate.

The most distinguishable feature was found in the results with smaller rotational parameters. In this case, the background shear convects the X-points on the “ghost” domain and the resulting structure takes the form such that the X-point and O-point of the neighboring current sheet to be located alternately. In this case, resulting reconnection rate is enhanced. We would note that this process is still active even if we assume another X-point in the current sheet initially located in the boundary.

This feature is newly observed by assuming periodicity on the inflow direction. By assuming periodicity, the effect from neighboring reconnection site was taken into account in the small simulation domain case. It should be noted that these features are expected to be found also in the MHD simulation, since the main source of the tilt is the Coriolis force and the shearing periodic boundary condition. Though we have carried out hybrid simulation, kinetic effect was found to be minor in

this configuration. Considering the application to the actual turbulence in the rotational system, the size of our simulation domain may correspond to the typical distance between the neighboring reconnection site. Whether this process takes place in the actual disk or not is determined by the relations between the rate of shear and a typical distance between the neighboring current sheet which strongly depends on the size of the vortices generated in the disk turbulence. This could be investigated by carrying a 3D hybrid simulation of the collisionless differentially rotating system and which would be one of the important problems in the future. Nevertheless, since very small rotational parameter is realized in the actual disk and the resulting effect of Coriolis force is weak, the interaction between multiple X-point due to the shear flow would be more important in the actual system.

# Chapter 5

## Summary and Future Inspections

### 5.1 Summary of this Thesis

Throughout this thesis, we have investigated the non-linear evolution of collisionless accretion disks such as Sgr A\* in the center of our galaxy. Particularly, we have focused on the interactions between magnetorotational instability (MRI) and magnetic reconnection. To take the effects of low collisionality into account we have developed a hybrid code instead of using the “collisionless MHD” approach. There were several difficulties in the hybrid simulation especially on the application to the problem involving a drastic change of density and magnetic field such as MRI. We have overcome this problem applying the finite electron mass method proposed by Amano et al. [2014]. We extended their method to 2.5D differentially rotating system, including Coriolis and tidal force. As a linear test problem for newly developed code, we have carried out “semi-1D” simulation of MRI. The results showed a good agreement with varying parameter of electron mass we used in the simulation. We consider that this result guarantees the validity of our new code.

From the simulation of 2.5D MRI in the meridional plane of the disk (Chapter 2) we observed a corruption of channel flows and formation of magnetic islands.

This result was consistent with the full particle results (Hoshino [2013]) rather than the MHD results whose final state is found to be a set of channel flow. The pressure anisotropy at this moment was evaluated and the result was consistent with the understanding that the growth rate of tearing mode is enhanced when the perpendicular pressure dominates in the current sheet (Chen and Palmadesso [1984]). Unlike the full particle result, the system did not reach the saturation. However the efficiency of the angular momentum ( $\alpha$ ) is evaluated and the value lied on  $O(0.1-1)$ . Investigating the stress component contributing to  $\alpha$ , we found that anisotropic stress has minor effect on  $\alpha$  parameter which is also consistent with Hoshino [2013]. Comparing the result with Sharma et al. [2006] this result would have an astrophysical implication that the pitch angle scattering by the kinetic instabilities are effective in the actual disks. Detailed investigation of the isotropization process and evaluation of the efficiency of the pitch angle scattering can be one of the important problem to be solved in the future. This can be done with the precise study of the kinetic instabilities, such as mirror and ion cyclotron instabilities in the rotational system.

In addition we observed an onset of the generation of the ion acceleration accompanied with the magnetic reconnection in the MRI driven current sheet. Since our calculation terminated at this moment, further evaluation of rate of the non-thermal ion generation or, power law index was not attained. However, our result would imply that the collisionless accretion disk is one of the agent of the ion acceleration. Our simulation is limited in the 2.5D system and the we did not obtain MRI induced turbulence. However we believe that our result is important as the first step for the further 3D calculation.

To investigate the microscopic activities which would take place in the MRI induced turbulence, we carried out simulation of magnetic reconnection in the meridional (Chapter 3) and equatorial (Chapter 4) plane of the disk.

In the calculation of magnetic reconnection on the meridional plane, the interplay between magnetic reconnection and MRI under the Hall effect generated an

asymmetric evolution of magnetic reconnection in each side of the current sheet and as a result, migration of the X-point was observed. Accompanied with this migration, significant radial magnetic field was generated during the evolution of magnetic reconnection. Resulting growth of the in-plane field ( $B_x$  and  $B_y$ ) was faster compared to the ordinary growth of MRI. Since, as we have seen in Chapter 2, the angular momentum transport due to the Maxwell stress is mainly sustained by the in-plane magnetic field, this process which effectively enhances the in-plane field during the magnetic reconnection would be an efficient mechanism to support a large value of  $\alpha$  in the collisionless accretion disk.

Since at the non-linear state of MRI, the azimuthal component of the magnetic field is dominant, the magnetic reconnection on the equatorial plane should be investigated as well. For the calculation on the equatorial plane of the disk, we have implemented open shearing periodic boundary condition (Hawley et al. [1995]). From the calculation, the asymmetric structure in the vicinity of the X-point was found as well. In contrast to the meridional calculation, there was no migration of the X-point. Here we have confirmed that due to the conservation of the angular momentum about the central star, the reconnection inflow is disturbed and the reconnection rate was reduced. However this was the case in the relatively large value of rotational parameter ( $\Omega_0/\Omega_{ci}$ ). Unlike the previous studies focusing on the single X-point evolution in the strong shear (e.g., Chen et al. [1997]), our calculation involves the effect of multiple X-points since our boundary condition assumes periodicity. Together with the background Keplerian shear, at the certain moment of the simulation, an X-point and an O-point in the neighboring current sheet is located alternately. In this case, the reconnection rate was enhanced compared to the case without shear motion. In both calculations, kinetic effects of the plasma such as generation/relaxation of pressure anisotropy was rather a minor effect on the evolution of the system. Instead, coupling with the differential rotation was found out to be essential. This can be realistic in the actual collisionless accretion disk. Since the magnetic reconnection takes place much faster than the Keplerian

time scale, generation of perpendicular pressure anisotropy by the differential rotation is expected to be a minor effect. Instead, “remaining pressure anisotropy” resulting from competing process of MRI and kinetic instabilities can be important on the evolution of magnetic reconnection in the MRI induced turbulence.

In the realistic disk, the rotational parameter ( $\Omega_0/\Omega_{ci}$ ) would be much smaller than the value we have used in our simulation. However, as we have discussed in Chapter 3, the thickness of the realistic current sheet would be larger compared to our simulations and the migration of the X-point which we proposed in Chapter 3 would still be important in the actual disk. In addition, the enhancement of the reconnection rate due to the Keplerian shear which we have pointed out is primarily determined by the typical distance of the neighboring current sheet. This can be evaluated by carrying 3D simulation of MRI-induced turbulence.

It is worth noting by using the hybrid code, we have bridged the scale gap between the MHD scale and the PIC scale. In addition open shearing periodic boundary condition which is essential for the future 3D calculation of MRI turbulence is implemented in our study. For the full understanding of the evolution of the MRI, the associated generation and relaxation of pressure anisotropy, the dissipation by magnetic reconnection, and the resulting efficient angular momentum transport, a massive 3D simulation would be required. In the next section, we will point out several important problems which should be studied in the future.

## 5.2 Future inspections

As a closing section for this thesis, we would like to point out a future application of our study.

First of all, extension to the 3D calculation with massive parallelization would be the most important problem to be investigated. Since the hybrid code has an advantage to full particle code in terms of the computational resource, long

term evolution of 3D MRI turbulence with particle based code is realistic using the hybrid code. In the present study the system did not reach a quasi steady state. By applying long term 3D calculations, we would investigate not only the efficiency of angular momentum transport, but also a particle acceleration processes in turbulence in a differentially rotating system.

It should be noted that the attainable spacial/temporal scale is still limited even with the hybrid code. In the realistic disk, generation of the pressure anisotropy would take place in the Keplerian time scale, which is far longer than the kinetic time scale. Therefore, as a direct speculation, one would expect that the evolution of the collisionless accretion disk can be well studied with MHD, or collisionless MHD framework. However, as we have seen in Chapter 2 the evolution of magnetic reconnection is greatly modified depending on the pressure anisotropy condition. With higher initial plasma  $\beta_i$ , we obtained a continuous magnetic reconnection until the termination of the calculation. Since the effect of magnetic reconnection on the generation/relaxation process of pressure anisotropy was not considered in the collisionless MHD framework, the ion scale activities still have a possibility to affect the disk scale physics through magnetic reconnection. We expect that this can be studied with the 3D calculation varying the rotational parameter and investigating the convergence of the bulk values such as  $\alpha$ .

It would also be worth noting that the code developed in this thesis is a first one to investigate non-linear evolution of MRI with a hybrid framework. We believe that this code can be extended to various problems in the accretion disk, not only a collisionless system, but also a system whose scale gap between each plasma component is significant. A most typical example of such system is dusty plasma (Verheest [2001]). Non-linear evolution of dusty plasma in the Keplerian rotating system is one of the fundamental problem in the context of planet (planetesimal) formation. Protoplanetary system is one of the most typical dusty plasma system. Though the ionization degree of the disk is extremely low, several ionization mechanism is suggested and the disk is considered to be “active” to the MRI. Evolution

of MRI including dust particles has been carried out by numbers of researchers (e.g., Johansen et al. [2007]), but in the past dust has been treated as neutral particles which interact with fluid components via drag force (Johansen et al. [2007]). In the dusty plasma system, the charge-to-mass ratio of the dust is much smaller than those of the electrons and ions. Therefore, it is rather natural to approximate electrons and ions as fluid components and dusts as charged-up particles. Moreover, the charge which the dust particles carry varies in time by capturing ions and electrons, or releasing them through, for example, photo-emissions. These effects can directly be included by using methods which explicitly solve the motion of the dust components as particles. Since we have developed a numerical technique to investigate a non-linear state of Keplerian rotating system with the mixture of fluid and particle components, we consider that evolution of MRI in dusty plasma can also be investigated basically with a same manner.

From this point of view we believe our new code has a possibility for the extension not only to collisionless accretion disks but also other much more wider class of plasmas.

# Appendix A

## Inclusion of Finite Electron Mass

Here we introduce a derivation of Equation (2.26) which takes effect of finite electron mass into account. The method is originally reported in Amano et al. [2014] calculating various types of 1D plasma problems. In this thesis we have extended the method to a 2.5D differentially rotating system.

We start from Ampère's law and Faraday's law

$$\mathbf{J} = \frac{c}{4\pi} \nabla \times \mathbf{B} \quad (\text{A.1})$$

$$\frac{\partial \mathbf{B}}{\partial t} = -c \nabla \times \mathbf{E}. \quad (\text{A.2})$$

Taking time derivative of Equation (A.1) and substituting Equation (A.2) to Equation (A.1), we obtain

$$\frac{\partial \mathbf{J}}{\partial t} = -\frac{c^2}{4\pi} \nabla \times \nabla \times \mathbf{E}. \quad (\text{A.3})$$

Using a distribution function of component "s" ( $f_s(\mathbf{v})$ ), total current is expressed as

$$\mathbf{J} = \sum_s q_s \int \mathbf{v} f_s(\mathbf{v}) d\mathbf{v}. \quad (\text{A.4})$$

Taking time derivative of Equation (A.4), we find

$$\frac{\partial \mathbf{J}}{\partial t} = \sum_s q_s \int \mathbf{v} \frac{\partial f_s}{\partial t} d\mathbf{v}. \quad (\text{A.5})$$

Time derivative of the distribution function is estimated with a Vlasov equation,

$$\frac{\partial f_s}{\partial t} + \mathbf{v} \cdot \frac{\partial f_s}{\partial \mathbf{x}} + \mathbf{a}_s \cdot \frac{\partial f_s}{\partial \mathbf{v}} = 0. \quad (\text{A.6})$$

Using Esq. (A.3), Equation (A.4), and Equation (A.6), we get

$$\begin{aligned} -\frac{c^2}{4\pi} \nabla \times \nabla \times \mathbf{E} &= \sum_s q_s \int \mathbf{v} \frac{\partial f_s}{\partial t} d\mathbf{v} \\ &= -\sum_s q_s \int \mathbf{v} \left[ \mathbf{v} \cdot \frac{\partial f_s}{\partial \mathbf{x}} + \mathbf{a}_s \cdot \frac{\partial f_s}{\partial \mathbf{v}} \right] d\mathbf{v} \\ &= -\sum_s q_s \int \mathbf{v} \otimes \mathbf{v} \cdot \frac{\partial f_s}{\partial \mathbf{x}} d\mathbf{v} - \sum_s q_s \int (-\mathbf{a}_s f_s) d\mathbf{v} \\ &= -\sum_s q_s \nabla \cdot \int \mathbf{v} \otimes \mathbf{v} f_s d\mathbf{v} + \sum_s q_s \int \mathbf{a}_s f_s d\mathbf{v}. \end{aligned} \quad (\text{A.7})$$

Here we used Gauss's theorem in the third to the fourth row. From the first term of the fourth row, we obtain a advection term and pressure tensor,

$$-\sum_s q_s \nabla \cdot \int \mathbf{v} \otimes \mathbf{v} f_s d\mathbf{v} = -\sum_s q_s \left( n_s \mathbf{V}_s \otimes \mathbf{V}_s + \frac{1}{m_s} \mathbf{P}_s \right), \quad (\text{A.8})$$

where  $\mathbf{V}_s$  is the bulk velocity,  $\mathbf{P}_s$  is the pressure tensor, and  $m_s$  is the mass.

Applying Lorentz force

$$\mathbf{a}_s = \frac{q_s}{m_s} \left( \mathbf{E} + \frac{1}{c} \mathbf{v} \times \mathbf{B} \right) \quad (\text{A.9})$$

for the second term in the fourth row of Equation (A.7), we get

$$\sum_s q_s \int \mathbf{a}_s f_s d\mathbf{v} = \sum_s \frac{q_s^2 n_s}{m_s} \mathbf{E} + \sum_s \frac{q_s^2 n_s}{m_s c} \mathbf{V}_s \times \mathbf{B}. \quad (\text{A.10})$$

As we find the term inversely proportional to the mass ( $\propto 1/m_s$ ), we may neglect the contribution from the ions for these terms because the ions are much heavier than the electrons. Advection term ( $\propto \mathbf{V}_s \otimes \mathbf{V}_s$ ) is usually small and negligible, except for the case when the electron bulk velocity reaches to the electron Alfvén velocity. Here to keep relatively general form, we retain this term for the electrons. Now all the terms in the right hand side of the Equation (A.7) are written in terms of electron bulk component. This physically corresponds to the fact that the temporal change of the total current is well approximated by that of the electron current in the hybrid framework. Introducing the electron plasma frequency  $\omega_{pe}^2 \equiv q_s^2 n_s / 4\pi m_s$  Equation (A.7) is written as

$$\begin{aligned} & \frac{1}{4\pi} (\omega_{pe}^2 \mathbf{E} + c^2 \nabla \times \nabla \times \mathbf{E}) \\ & = -\frac{q_e}{m_e} \left( \frac{\mathbf{J}_e}{c} \times \mathbf{B} - \nabla \cdot \mathbf{P}_e \right) + q_e n_e \nabla \cdot (\mathbf{V}_e \otimes \mathbf{V}_e) \end{aligned} \quad (\text{A.11})$$

since we assume the quasi neutral condition ( $n_e \simeq n_i$ ),  $\nabla \cdot \mathbf{E} \simeq 0$  holds, we obtain

$$\begin{aligned} \frac{1}{4\pi} (\omega_{pe}^2 - c^2 \nabla^2) \mathbf{E} & = -\frac{q_e}{m_e} \left( \frac{\mathbf{J}_e}{c} \times \mathbf{B} - \nabla \cdot \mathbf{P}_e \right) + q_e n_e \nabla \cdot (\mathbf{V}_e \otimes \mathbf{V}_e) \\ & = \frac{\omega_{pe}^2}{4\pi} \hat{\mathbf{E}}, \end{aligned} \quad (\text{A.12})$$

where  $\hat{\mathbf{E}}$  is the electric field which is obtained with ordinary hybrid code procedure.

Since this method only requires a post process to obtain  $\mathbf{E}$  from  $\hat{\mathbf{E}}$ , this it is easy to implement after the conventional hybrid coding. Moreover, division-by-density, one of the most critical operation to generate numerical noise in the hybrid simulation is almost eliminated by using the form Equation (A.12). Density division appears only in the advection term, which usually gives a minor effect on the simulation. For the calculation of Equation (A.12) we have to solve a elliptic equation for  $\mathbf{E}$  with the source term of  $n_e \hat{\mathbf{E}}$  and in this study, we simply use Gauss-Seidel method.

# Appendix B

## Open Shearing Periodic Boundary condition

Here we introduce open shearing periodic boundary condition, and its implementation to our hybrid Code. As we described in Chapter 2, we use staggered mesh to guarantee the solenoidal condition of the magnetic field ( $\nabla \cdot \mathbf{B} = 0$ ). Figure B.1 shows a schematic illustration of the real simulation domain and the “ghost” domains. At the initial state, the real simulation domain and the ghost domain is located in the same  $y$ -position. As time goes on, background shear convects the ghost domain and one should take this convection into account while taking periodicity. As described in Chapter 4 sheared length of the ghost domain is exactly calculated from the elapsed physical time from the initial state and the resulting periodic boundary condition at  $t = t_1$  becomes,

$$f(x, 0) = f(x, L_y) \tag{B.1}$$

$$f(0, y) = f(L_x, y - q\Omega_0 L_x t_1) \tag{B.2}$$

$$f(L_x, y) = f(0, y + q\Omega_0 L_x t_1). \tag{B.3}$$

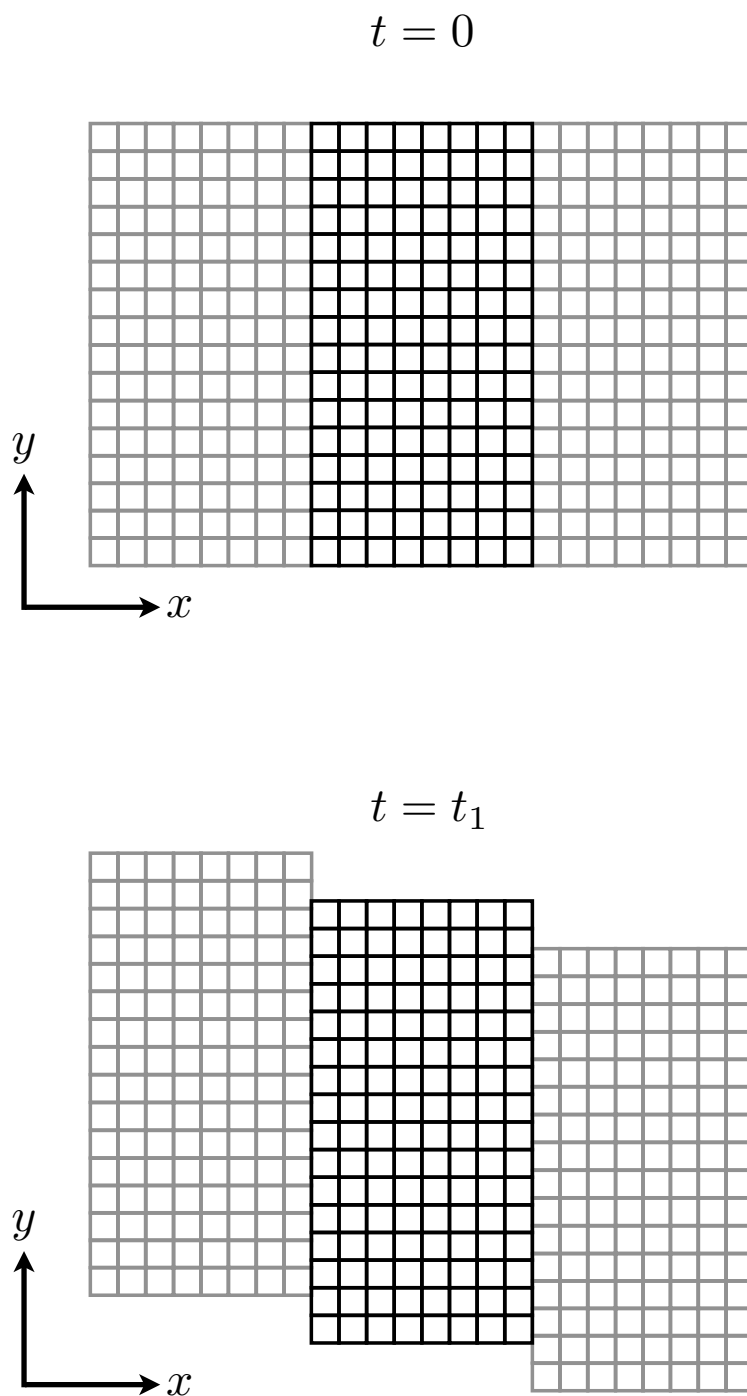


FIGURE B.1: Schematic illustration of open shearing periodic boundary condition. The simulation domain is described with black grids whereas the ghost domain is described with gray grids. As the simulation goes on the ghost domain in the inner and outer side is convected due to the background shear motion.

Since the sheared length  $|q\Omega_0 L_x t_1|$  does not necessarily take the integral multiple of grid interval, one must interpolate the values on the boundary of ghost domain to on-grid of the real domain.

Figure B.2 shows a schematic illustration of the left side boundary condition of the simulation domain. The black mesh corresponds to the actual domain we calculate, whereas the gray mesh corresponds to the “sheared” grid at the certain moment of the simulation. Magnetic field  $(B_x, B_y, B_z)$  and electric field  $(E_x, E_y, E_z)$  is located so as to be in the Constrained Transport (CT) location. The sheared mesh does not necessarily located on the integer grid, so at each time step, all physical values in the ghost domain are remapped to the grid which is colored with red in FigureB.2. In this thesis we simply used linear interpolation by using two nearest grids for remapping.

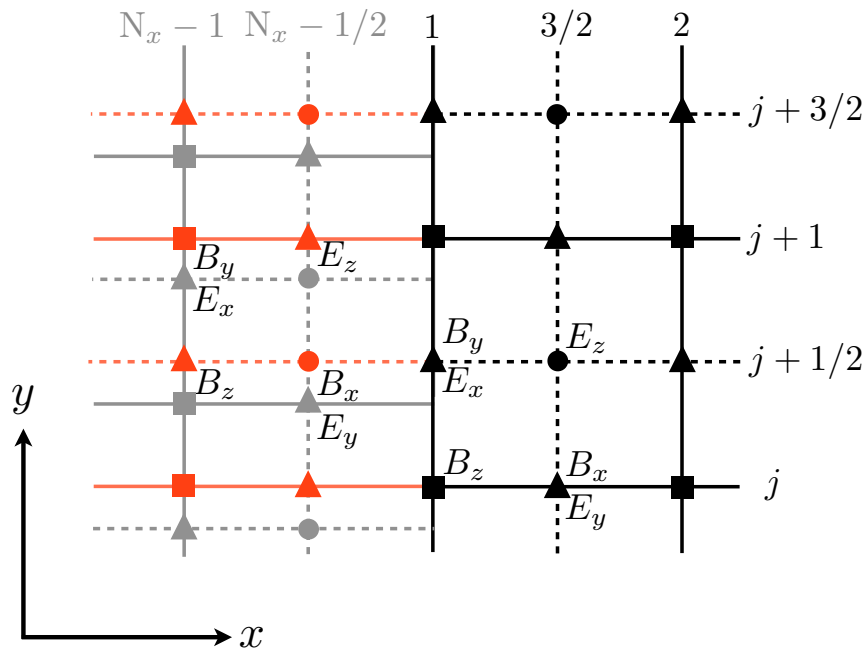


FIGURE B.2: Schematic illustration of a staggered mesh and open shearing boundary condition in the left side of the simulation domain.

Since we have used CT method, solenoidal condition is guaranteed within the machine epsilon. However, the CT method guarantees the divergence free condition only for  $\nabla \times$  operation, and once the “shearing” and remapping operation on the magnetic field is applied,  $\nabla \cdot \mathbf{B} = 0$  is disturbed. Break in this condition generates

the unphysical acceleration of the particles parallel to the magnetic field and one must take care for this error.

Here in our mesh,  $B_y$  and  $B_z$  on the boundary is calculated by taking rotation of  $\mathbf{E}$ . For the calculation of  $B_x^{i=1/2,j}$ , we used  $\nabla \cdot \mathbf{B} = 0$  condition itself, instead of using the Faraday's law (Equation (1.51)),

$$B_x^{i=1/2,j} = B_x^{i=3/2,j} - \frac{\Delta_x}{\Delta_y} (B_y^{i,j+1/2} - B_y^{i,j-1/2}). \quad (\text{B.4})$$

This  $B_x^{i=1/2,j}$  obtained from Equation (B.4), is used for the digital filtering operation (Birdsall and Langdon [1991]), and the calculation of local magnetic field which particles near the boundary feels. We have confirmed that the  $\nabla \cdot \mathbf{B} = 0$  is satisfied within the machine epsilon throughout our calculation.

Using this boundary condition, our simulation code provides stable calculation in the relatively small value of rotational parameter. However runs with the larger rotational parameter ( $\Omega_0/\Omega_{ci} \gtrsim 0.01$ ), the numerical noise generated at the non-linear state could not be neglected. This numerical noise was, in practice, reduced by setting infinitesimally small field value in the boundary. We have applied this condition by setting double-Harris sheet with one sheet located in the domain center and the other on the domain boundary. In addition, for larger value of rotational parameter ( $\Omega_0/\Omega_{ci} \gtrsim 0.01$ ), we also imposed a localized resistivity along the  $y$ -direction of the boundary with the following form to reduce numerical noise

$$\eta_{\text{Boundary}} = \eta_c \cosh^{-2} \left[ \left( \frac{x - x_1}{2\lambda_i} \right)^2 + \left( \frac{x - x_N}{2\lambda_i} \right)^2 \right]. \quad (\text{B.5})$$

# Appendix C

## Methods for calculating differentially rotating system using hybrid code.

Here we briefly describe about the modification applied in our hybrid code due to the differential rotation.

As we explained in Section 3.2, we assume that the background Kepler rotation always exists. Therefore one must pay attention to the boundary condition since the out-of-plane flow velocity differs between the inner and outer boundary of the domain. However, as a Keplerian velocity can be exactly calculated from equation (2.13) we simply focus on the deviation from the Keplerian profile. Since we assume the azimuthal symmetry ( $\partial/\partial y = 0$ ) the open shearing periodic boundary condition proposed by Hawley et al. [1995] degenerates to a standard periodic boundary condition for the deviation components.

For updating of the particles, we use the Buneman-Boris method. Here we use the particle velocity observed in the corotating frame; that is, all the particle velocity includes the Keplerian component in the time integration of the particle. At each

time step we subtract the Keplerian velocity component of the particles using updated position information ( $\mathbf{x}_i^{n+1/2}$ ). Then we apply a moment calculation to obtain the deviation component of the current density using an appropriate shape function,

$$\mathbf{J}_{i,\text{dev}}^{n+1/2} = q_i \sum_{\text{particle}} \mathbf{v}_{i,\text{dev}}^{n+1/2} S(\mathbf{x}_i^{n+1/2}). \quad (\text{C.1})$$

From  $\mathbf{J}_{i,\text{dev}}^{n+1/2}$  we calculate the deviation component of the electric field ( $\mathbf{E}_{\text{dev}}^{n+1/2}$ ) by using the Ohm's law (2.23), and the Ampère's law (2.21). Note that since the simulation is performed under nonrelativistic limit, the magnetic field is Lorentz invariant. The electric field observed in the corotating frame is obtained by applying a Lorentz transformation on this electric field. This is applied by adding the induction term due to the Keplerian flow to the deviation component,

$$\mathbf{E}^{n+1/2} = \mathbf{E}_{\text{dev}}^{n+1/2} - \frac{1}{c} \mathbf{v}_K \times \mathbf{B}^{n+1/2}. \quad (\text{C.2})$$

For the update of the magnetic field, we separate the  $\nabla \times$  calculation of the electric field to the deviation component and the Keplerian component. As we assume the azimuthal symmetry ( $\partial/\partial y = 0$ ), together with the solenoidal condition (2.6), the Keplerian component of the induction term is calculated as follows,

$$\frac{1}{c} \nabla \times (\mathbf{v}_K \times \mathbf{B}^{n+1/2}) = -\frac{1}{c} q \Omega_0 B_x^{n+1/2} \mathbf{e}_y. \quad (\text{C.3})$$

This equation physically describes the shearing effect of the differential rotation generating the  $y$ -component magnetic field from the  $x$ -component.  $\mathbf{B}^{n+1/2}$  and  $\mathbf{E}^{n+1/2}$  are iteratively calculated in the update of the field. Since the periodicity is guaranteed for the deviation components and for the magnetic field, this separation of the  $\nabla \times$  calculation greatly reduces the complication in taking the boundary condition with the shear flow.

# Appendix D

## Resistivity Used in MRI Calculation

In the MRI calculation of Chapter 2, we have imposed anomalous resistivity (e.g., Sato and Hayashi [1979]) with the form,

$$\eta = \eta_0 + \begin{cases} \eta_A (J^2 - J_0^2) / J_0^2 & (J^2 > J_0^2) \\ 0 & (\text{otherwise}) \end{cases} \quad (\text{D.1})$$

where  $\eta_0$  is the uniform component of the resistivity and  $\eta_A$  is the anomalous component. The magnetic Reynolds number defined by  $\lambda_i V_A / \eta_0$  and  $\lambda_i V_A / \eta_A$  was 120 and 60 respectively, and the critical current density  $J_0$  is chosen to be  $4\pi\lambda_{i0}J_0/cB_0 = 10$ . The anomalous resistivity was imposed primarily, to trigger magnetic reconnection in the channel flow. However the results we obtained had no significant difference between the calculations using uniform resistivity.

In the non-linear stage of our simulation, the channel flow generated in the non-linear stage of MRI is corrupted due to the magnetic reconnection. As reported in Shay et al. [1998], in the hybrid simulation of magnetic reconnection, the density depletion region near the separatrix is generated. Though the numerical instability related to the hybrid code has improved using the method proposed in Amano

et al. [2014], our code is still unstable when the system encounters a continuous formation of low density region. Using the resistivity in the form of Equation (D.1), the numerical instability was slightly improved though the system did not reach to the quasi steady state.

# Appendix E

## Harris solution in differentially rotating system

Here we discuss the behavior of a Harris solution in the rotating system. A conventional Harris solution cannot be an exact kinetic equilibrium solution in a differentially rotating disk because the solution introduced in Harris [1962] is based on the conservation of the canonical angular momentum for each particle. In a differentially rotating disk the angular momentum due to the central massive object must be taken into account together with the angular momentum due to the cyclotron motion.

Considering the differential rotation under the Hill coordinate (Hill [1878]) we obtain a second order ordinary differential equation which degenerates to the one introduced in the equation (16) of Harris [1962] in the limit of  $\Omega_0 \rightarrow 0$ . The solution cannot be expressed with a superposition of simple functions. Therefore we have simply adopted a superposition of a conventional Harris solution and a Keplerian differential rotation as an initial asymptotic solution. Here we investigate whether this approximation is valid or not in the case of  $\Omega_0/\Omega_{ci} \ll 1$ . We carry out five comparative runs with no initial trigger for the magnetic reconnection, i.e.,  $B_1 = 0$  in Equation (3.14) and  $\eta_c = 0$  in Equation (3.15), with the rotational parameter

used in the main runs. We also restrict the vertical size of the simulation domain ( $L_z$ ) to guarantee the outside of the current sheet region to be stable to the MRI. From the results, it is confirmed that the initial structure of the current sheet is conserved in time. However, we also find that the neutral point of the current sheet moves in time.

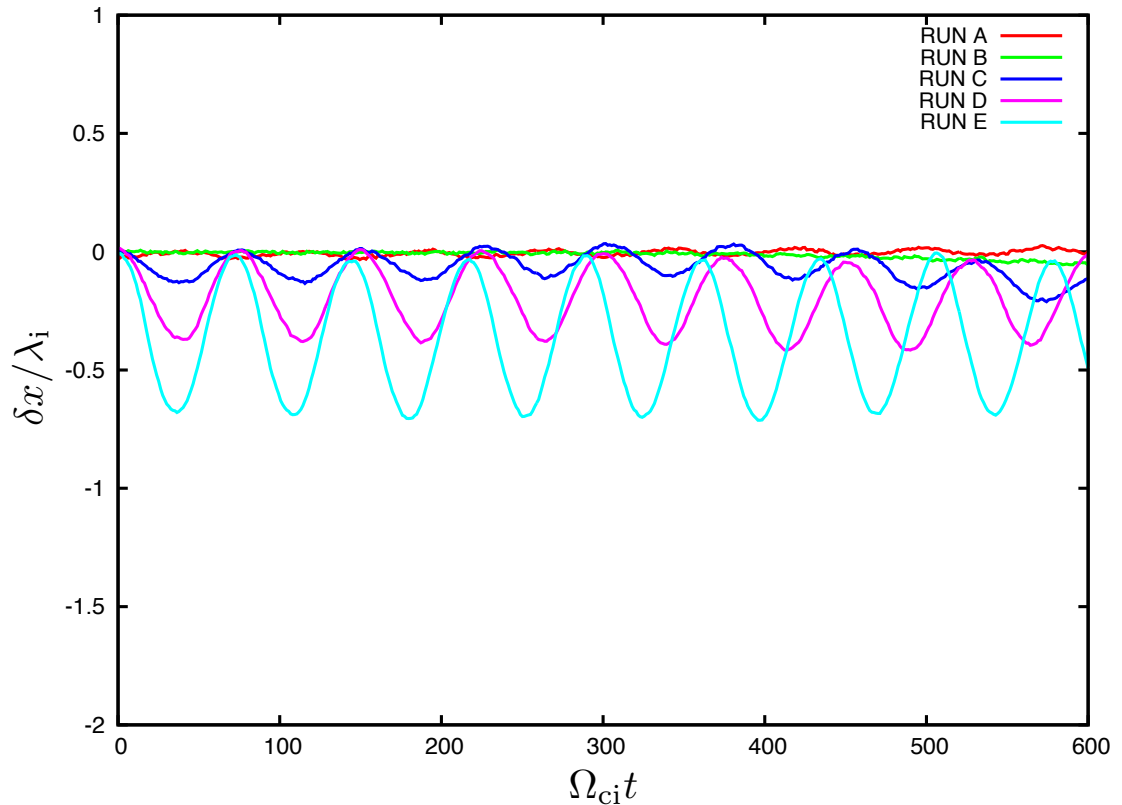


FIGURE E.1: The oscillation of the neutral point. The deviation from the initial neutral point ( $\delta x$ ) in the unit of inertia length is plotted in the vertical direction.

Figure E.1 shows the position of the neutral point observed in each calculation. As the rotational parameter increases the amplitude of oscillation becomes significant though its amplitude is smaller than the initial width of the current sheet. This is due to the initial current in the neutral sheet. Since in this calculation, the ions are hotter than the electrons, the dominant component with subject to an out-of-plane initial current is the ions. As the ions have finite mass in the hybrid framework, any initial motion inside the equatorial plane will couple to the differential rotation

through the Coriolis force. In this case the initial out of plane drift  $\pm V_y$  creates  $\mp V_x$  with  $\pi/2$  phase delays due to the Coriolis force. Once  $V_x$  has created the compression and the expansion of the plasma and the magnetic field take place. Therefore, the oscillation can roughly be regarded as a perpendicular mode of the fast mode magnetosonic wave. The estimated frequency of perpendicular fast mode wave in this system is approximately  $0.1\Omega_{ci}$ , which roughly explains the results.

As the amplitude of this oscillation is relatively small throughout all the parameters used in this calculation we find it is valid to use a Harris solution as an approximate equilibrium solution in this system provided that the rotational parameter  $\Omega_0/\Omega_{ci}$  is sufficiently small. However, since the anomalous resistivity is imposed locally in the current sheet center, and since the current sheet oscillates in time, one must pay attention to the detection of the current sheet center. At each time step the current sheet centers ( $x_c(t)$  and  $x'_c(t)$ ) are detected by calculating a local maximum of  $|(\nabla \times \mathbf{B})_y|$  in the vicinity of the current sheet centers which has also been detected in the previous time step.

It is worth noting that the initial direction of  $V_x$  generated by the neutral sheet current and the direction of the X-point migration introduced in Section 3.3 is opposite. In addition, we have also confirmed, by setting  $\eta_c = 0$  in equation (3.15), that the way of detecting the current sheet center does not affect the direction of the X-point migration. Therefore, we conclude that the X-point migration is independent to initial plasma sheet oscillation and purely a result of coupling with the structure of the reconnection and the differential rotation.

# Bibliography

- T. Amano, K. Higashimori, and K. Shirakawa. A robust method for handling low density regions in hybrid simulations for collisionless plasmas. *Journal of Computational Physics*, 275:197–212, October 2014. doi: 10.1016/j.jcp.2014.06.048.
- K. Arzner and M. Scholer. Kinetic structure of the post plasmoid plasma sheet during magnetotail reconnection. *Journal of Geophysical Research*, 106:3827–3844, March 2001. doi: 10.1029/2000JA000179.
- Y. Asano, T. Mukai, M. Hoshino, Y. Saito, H. Hayakawa, and T. Nagai. Evolution of the thin current sheet in a substorm observed by Geotail. *Journal of Geophysical Research*, 108:1189, May 2003. doi: 10.1029/2002JA009785.
- S. A. Balbus and J. F. Hawley. Instability, turbulence, and enhanced transport in accretion disks. *Reviews of Modern Physics*, 70:1–53, January 1998. doi: 10.1103/RevModPhys.70.1.
- S. A. Balbus and J. F. Hawley. A powerful local shear instability in weakly magnetized disks. I - Linear analysis. II - Nonlinear evolution. *Astrophysical Journal*, 376:214–233, July 1991. doi: 10.1086/170270.
- S. A. Balbus and C. Terquem. Linear Analysis of the Hall Effect in Protostellar Disks. *Astrophysical Journal*, 552:235–247, May 2001. doi: 10.1086/320452.
- C. K. Birdsall and A. B. Langdon. *Plasma Physics via Computer Simulation*. IOP Publishing Ltd., Bristol, 1991.

- J. Birn, J. F. Drake, M. A. Shay, B. N. Rogers, R. E. Denton, M. Hesse, M. Kuznetsova, Z. W. Ma, A. Bhattacharjee, A. Otto, and P. L. Pritchett. Geospace Environmental Modeling (GEM) magnetic reconnection challenge. *Journal of Geophysical Research*, 106:3715–3720, March 2001. doi: 10.1029/1999JA900449.
- H. Bondi. On spherically symmetrical accretion. *Monthly Notices of the Royal Astrophysical Society*, 112:195, 1952.
- F. Cao and J. R. Kan. Oblique tearing of a thin current sheet - Implications for patchy magnetopause reconnection. *Journal of Geophysical Research*, 96: 5859–5867, April 1991. doi: 10.1029/90JA02746.
- P. A. Cassak. Theory and simulations of the scaling of magnetic reconnection with symmetric shear flow. *Physics of Plasmas*, 18(7):072106, July 2011. doi: 10.1063/1.3602859.
- P. A. Cassak and A. Otto. Scaling of the magnetic reconnection rate with symmetric shear flow. *Physics of Plasmas*, 18(7):074501, July 2011. doi: 10.1063/1.3609771.
- S. Chandrasekhar. The Stability of Non-Dissipative Couette Flow in Hydromagnetics. *Proceedings of the National Academy of Science*, 46:253–257, February 1960. doi: 10.1073/pnas.46.2.253.
- S. Chandrasekhar. *Hydrodynamic and hydromagnetic stability*. Courier Dover Publications, 1961.
- J. Chen and P. Palmadesso. Tearing instability in an anisotropic neutral sheet. *Physics of Fluids*, 27:1198–1206, May 1984. doi: 10.1063/1.864727.
- J. Chen, J. G. Lyon, P. J. Palmadesso, and J. A. Fedder. Fast collisionless tearing in an anisotropic neutral sheet. *Geophysical Research Letters*, 11:12–15, January 1984. doi: 10.1029/GL011i001p00012.

- Q. Chen, A. Otto, and L. C. Lee. Tearing instability, Kelvin-Helmholtz instability, and magnetic reconnection. *Journal of Geophysical Research*, 102:151–162, January 1997. doi: 10.1029/96JA03144.
- Y. Chen, C. Xiao, X. Wang, J. Wang, H. Zhang, Z. Pu, Z. Ma, and Z. Guo. The influence of out-of-plane shear flow on Hall magnetic reconnection and FTE generation. *Journal of Geophysical Research (Space Physics)*, 118:4279–4288, July 2013. doi: 10.1002/jgra.50417.
- G. F. Chew, M. L. Goldberger, and F. E. Low. The Boltzmann Equation and the One-Fluid Hydromagnetic Equations in the Absence of Particle Collisions. *Royal Society of London Proceedings Series A*, 236:112–118, July 1956. doi: 10.1098/rspa.1956.0116.
- J. W. Dungey. Interplanetary Magnetic Field and the Auroral Zones. *Physical Review Letters*, 6:47–48, January 1961. doi: 10.1103/PhysRevLett.6.47.
- N. M. Ferraro. Finite Larmor Radius Effects on the Magnetorotational Instability. *Astrophysical Journal*, 662:512–516, June 2007. doi: 10.1086/517877.
- J. Frank, A. King, and D. J. Raine. *Accretion Power in Astrophysics: Third Edition*. Cambridge University Press, January 2002.
- H. P. Furth, J. Killeen, and M. N. Rosenbluth. Finite-Resistivity Instabilities of a Sheet Pinch. *Physics of Fluids*, 6:459–484, April 1963. doi: 10.1063/1.1706761.
- S. P. Gary, J. Wang, D. Winske, and S. A. Fuselier. Proton temperature anisotropy upper bound. *Journal of Geophysical Research*, 102:27159–27170, December 1997. doi: 10.1029/97JA01726.
- A. M. Ghez, G. Duchêne, K. Matthews, S. D. Hornstein, A. Tanner, J. Larkin, M. Morris, E. E. Becklin, S. Salim, T. Kremenek, D. Thompson, B. T. Soifer, G. Neugebauer, and I. McLean. The First Measurement of Spectral Lines in a Short-Period Star Bound to the Galaxy’s Central Black Hole: A Paradox of Youth. *Astrophysical Journal*, 586:L127–L131, April 2003. doi: 10.1086/374804.

- J. Goodman and G. Xu. Parasitic instabilities in magnetized, differentially rotating disks. *Astrophysical Journal*, 432:213–223, September 1994. doi: 10.1086/174562.
- J. T. Gosling, M. F. Thomsen, S. J. Bame, and C. T. Russell. Accelerated plasma flows at the near-tail magnetopause. *Journal of Geophysical Research*, 91:3029–3041, March 1986. doi: 10.1029/JA091iA03p03029.
- E.G. Harris. On a plasma sheath separating regions of oppositely directed magnetic field. *Il Nuovo Cimento Series 10*, 23(1):115–121, 1962. ISSN 0029-6341. doi: 10.1007/BF02733547. URL <http://dx.doi.org/10.1007/BF02733547>.
- A. Hasegawa. Drift mirror instability of the magnetosphere. *Physics of Fluids*, 12: 2642–2650, 1969. doi: 10.1063/1.1692407.
- L.-N. Hau and B. U. Ö. Sonnerup. The thickness of resistive-dispersive shocks. *Journal of Geophysical Research*, 97:8269–8275, June 1992. doi: 10.1029/92JA00138.
- J. F. Hawley and S. A. Balbus. A Powerful Local Shear Instability in Weakly Magnetized Disks. II. Nonlinear Evolution. *Astrophysical Journal*, 376:223, July 1991. doi: 10.1086/170271.
- J. F. Hawley and S. A. Balbus. A powerful local shear instability in weakly magnetized disks. III - Long-term evolution in a shearing sheet. *Astrophysical Journal*, 400:595–609, December 1992. doi: 10.1086/172021.
- J. F. Hawley and J. M. Stone. MOCCT: A numerical technique for astrophysical MHD. *Computer Physics Communications*, 89:127–148, August 1995. doi: 10.1016/0010-4655(95)00190-Q.
- J. F. Hawley, C. F. Gammie, and S. A. Balbus. Local Three-dimensional Magnetohydrodynamic Simulations of Accretion Disks. *Astrophysical Journal*, 440: 742, February 1995. doi: 10.1086/175311.

- T. Heinemann and E. Quataert. Linear Vlasov Theory in the Shearing Sheet Approximation with Application to the Magneto-rotational Instability. *Astrophysical Journal*, 792:70, September 2014. doi: 10.1088/0004-637X/792/1/70.
- M. Hesse and D. Winske. Hybrid simulations of collisionless ion tearing. *Geophysical Research Letters*, 20:1207–1210, June 1993. doi: 10.1029/93GL01250.
- M. Hesse and D. Winske. Hybrid simulations of collisionless reconnection in current sheets. *Journal of Geophysical Research*, 99:11177–11192, June 1994. doi: 10.1029/94JA00676.
- K. Higashimori and M. Hoshino. The relation between ion temperature anisotropy and formation of slow shocks in collisionless magnetic reconnection. *Journal of Geophysical Research (Space Physics)*, 117:A01220, January 2012. doi: 10.1029/2011JA016817.
- G. W. Hill. Researches in the lunar theory. *American Journal of Mathematics*, 1(1):pp. 5–26, 1878. ISSN 00029327. URL <http://www.jstor.org/stable/2369430>.
- E. J. Horowitz, D. E. Shumaker, and D. V. Anderson. QN3D: A Three-Dimensional Quasi-neutral Hybrid Particle-in-Cell Code with Applications to the Tilt Mode Instability in Field Reserved Configurations. *Journal of Computational Physics*, 84:279–310, October 1989. doi: 10.1016/0021-9991(89)90234-9.
- W. Horton and T. Tajima. Linear theory of driven reconnection. *Journal of Geophysical Research*, 93:2741–2748, April 1988. doi: 10.1029/JA093iA04p02741.
- M. Hoshino. Forced magnetic reconnection in a plasma sheet with localized resistivity profile excited by lower hybrid drift type instability. *Journal of Geophysical Research*, 96:11555, July 1991. doi: 10.1029/91JA00984.
- M. Hoshino. Particle Acceleration during Magnetorotational Instability in a Collisionless Accretion Disk. *Astrophysical Journal*, 773:118, August 2013. doi: 10.1088/0004-637X/773/2/118.

- A. Johansen, J. S. Oishi, M.-M. Mac Low, H. Klahr, T. Henning, and A. Youdin. Rapid planetesimal formation in turbulent circumstellar disks. *Nature*, 448: 1022–1025, August 2007. doi: 10.1038/nature06086.
- C. F. Kennel and R. Z. Sagdeev. Collisionless shock waves in high  $\beta$  plasmas: 1. *Journal of Geophysical Research*, 72:3303–3326, July 1967. doi: 10.1029/JZ072i013p03303.
- A. Krabbe, R. Genzel, S. Drapatz, and V. Rotaciuc. A cluster of He I emission-line stars in the Galactic center. *Astrophysical Journal Letters*, 382:L19–L22, November 1991. doi: 10.1086/186204.
- R. M. Kulsrud. MHD description of plasma. In A. A. Galeev and R. N. Sudan, editors, *Basic Plasma Physics: Selected Chapters, Handbook of Plasma Physics, Volume 1*, page 1. North Holland, New York, 1983.
- M. W. Kunz, A. A. Schekochihin, and J. M. Stone. Firehose and Mirror Instabilities in a Collisionless Shearing Plasma. *Physical Review Letters*, 112(20): 205003, May 2014a. doi: 10.1103/PhysRevLett.112.205003.
- M. W. Kunz, J. M. Stone, and X.-N. Bai. Pegasus: A new hybrid-kinetic particle-in-cell code for astrophysical plasma dynamics. *Journal of Computational Physics*, 259:154–174, February 2014b. doi: 10.1016/j.jcp.2013.11.035.
- M. M. Kuznetsova, M. Hesse, and D. Winske. Kinetic quasi-viscous and bulk flow inertia effects in collisionless magnetotail reconnection. *Journal of Geophysical Research*, 103:199–214, January 1998. doi: 10.1029/97JA02699.
- A. L. La Belle-Hamer, A. Otto, and L. C. Lee. Magnetic reconnection in the presence of sheared plasma flow: Intermediate shock formation. *Physics of Plasmas*, 1:706–713, March 1994. doi: 10.1063/1.870816.
- A. L. La Belle-Hamer, A. Otto, and L. C. Lee. Magnetic reconnection in the presence of sheared flow and density asymmetry: Applications to the Earth’s

- magnetopause. *Journal of Geophysical Research*, 100:11875, July 1995. doi: 10.1029/94JA00969.
- A. S. Lipatov. *The hybrid multiscale simulation technology: an introduction with application to astrophysical and laboratory plasmas*. Springer, 2002.
- D. Lynden-Bell and J. E. Pringle. The evolution of viscous discs and the origin of the nebular variables. *Monthly Notices of the Royal Astrophysical Society*, 168: 603–637, September 1974.
- R. Matsumoto and T. Tajima. Magnetic viscosity by localized shear flow instability in magnetized accretion disks. *Astrophysical Journal*, 445:767–779, June 1995. doi: 10.1086/175739.
- R. Narayan and I. Yi. Advection-dominated accretion: A self-similar solution. *Astrophysical Journal*, 428:L13–L16, June 1994. doi: 10.1086/187381.
- R. Narayan and I. Yi. Advection-dominated accretion: Self-similarity and bipolar outflows. *Astrophysical Journal*, 444:231–243, May 1995. doi: 10.1086/175599.
- R. Narayan, I. Yi, and R. Mahadevan. Explaining the spectrum of Sagittarius A\* with a model of an accreting black hole. *Nature*, 374:623–625, April 1995. doi: 10.1038/374623a0.
- E. N. Parker. Sweet’s Mechanism for Merging Magnetic Fields in Conducting Fluids. *Journal of Geophysical Research*, 62:509–520, December 1957. doi: 10.1029/JZ062i004p00509.
- E. N. Parker. The Solar-Flare Phenomenon and the Theory of Reconnection and Annihilation of Magnetic Fields. *Astrophysical Journals*, 8:177, July 1963. doi: 10.1086/190087.
- H. E. Petschek. Magnetic Field Annihilation. *NASA Special Publication*, 50:425, 1964.

- J. E. Pringle. Accretion discs in astrophysics. *Annual Review of Astron and Astrophys.*, 19:137–162, 1981. doi: 10.1146/annurev.aa.19.090181.001033.
- P. L. Pritchett. Geospace Environment Modeling magnetic reconnection challenge: Simulations with a full particle electromagnetic code. *Journal of Geophysical Research*, 106:3783–3798, March 2001. doi: 10.1029/1999JA001006.
- E. Quataert. Radiatively Inefficient Accretion Flow Models of Sgr A\*. *Astronomische Nachrichten Supplement*, 324:435–443, September 2003. doi: 10.1002/asna.200385043.
- E. Quataert, W. Dorland, and G. W. Hammett. The Magnetorotational Instability in a Collisionless Plasma. *Astrophysical Journal*, 577:524–533, September 2002. doi: 10.1086/342174.
- M. A. Riquelme, E. Quataert, P. Sharma, and A. Spitkovsky. Local Two-dimensional Particle-in-cell Simulations of the Collisionless Magnetorotational Instability. *Astrophysical Journal*, 755:50, August 2012. doi: 10.1088/0004-637X/755/1/50.
- T. Sano and S.-i. Inutsuka. Saturation and Thermalization of the Magnetorotational Instability: Recurrent Channel Flows and Reconnections. *Astrophysical Journal*, 561:L179–L182, November 2001. doi: 10.1086/324763.
- T. Sano and J. M. Stone. The Effect of the Hall Term on the Nonlinear Evolution of the Magnetorotational Instability. I. Local Axisymmetric Simulations. *Astrophysical Journal*, 570:314–328, May 2002a. doi: 10.1086/339504.
- T. Sano and J. M. Stone. The Effect of the Hall Term on the Nonlinear Evolution of the Magnetorotational Instability. II. Saturation Level and Critical Magnetic Reynolds Number. *Astrophysical Journal*, 577:534–553, September 2002b. doi: 10.1086/342172.

- T. Sato and T. Hayashi. Externally driven magnetic reconnection and a powerful magnetic energy converter. *Physics of Fluids*, 22:1189–1202, June 1979. doi: 10.1063/1.862721.
- R. Schödel, T. Ott, R. Genzel, R. Hofmann, M. Lehnert, A. Eckart, N. Mouawad, T. Alexander, M. J. Reid, R. Lenzen, M. Hartung, F. Lacombe, D. Rouan, E. Gendron, G. Rousset, A.-M. Lagrange, W. Brandner, N. Ageorges, C. Lidman, A. F. M. Moorwood, J. Spyromilio, N. Hubin, and K. M. Menten. A star in a 15.2-year orbit around the supermassive black hole at the centre of the Milky Way. *Nature*, 419:694–696, October 2002. doi: 10.1038/nature01121.
- N. I. Shakura and R. A. Sunyaev. Black holes in binary systems. Observational appearance. *Astronomy and Astrophysics*, 24:337–355, 1973.
- P. Sharma, G. W. Hammett, E. Quataert, and J. M. Stone. Shearing Box Simulations of the MRI in a Collisionless Plasma. *Astrophysical Journal*, 637:952–967, February 2006. doi: 10.1086/498405.
- M. A. Shay, J. F. Drake, R. E. Denton, and D. Biskamp. Structure of the dissipation region during collisionless magnetic reconnection. *Journal of Geophysical Research*, 103:9165–9176, May 1998. doi: 10.1029/97JA03528.
- K. Shirakawa and M. Hoshino. Asymmetric evolution of magnetic reconnection in collisionless accretion disk. *Physics of Plasmas*, 21(5):052903, May 2014. doi: 10.1063/1.4875739.
- P. B. Snyder, G. W. Hammett, and W. Dorland. Landau fluid models of collisionless magnetohydrodynamics. *Physics of Plasmas*, 4:3974–3985, November 1997. doi: 10.1063/1.872517.
- B. U. Ö. Sonnerup. *Magnetic field reconnection*, pages 45–108. Amsterdam, North-Holland Publishing Co., 1979.

- J. M. Stone, J. F. Hawley, C. F. Gammie, and S. A. Balbus. Three-dimensional Magnetohydrodynamical Simulations of Vertically Stratified Accretion Disks. *Astrophysical Journal*, 463:656, June 1996. doi: 10.1086/177280.
- P. A. Sweet. The Neutral Point Theory of Solar Flares. In B. Lehnert, editor, *Electromagnetic Phenomena in Cosmical Physics*, volume 6 of *IAU Symposium*, page 123, 1958.
- T. Terasawa. Hall current effect on tearing mode instability. *Geophysical Research Letters*, 10:475–478, June 1983. doi: 10.1029/GL010i006p00475.
- S. Tsuneta. Structure and Dynamics of Magnetic Reconnection in a Solar Flare. *Astrophysical Journal*, 456:840, January 1996. doi: 10.1086/176701.
- E.P. Velikhov. Stability of an ideally conducting liquid flowing between rotating cylinder in a magnetic field. *Zhur. Eksptl'. i Teoret. Fiz.*, 36, May 1959.
- F. Verheest. *Waves in dusty space plasmas*, volume 245. Springer, 2001.
- J. Wang, X. Wang, and C. Xiao. Out-of-plane bipolar and quadrupolar magnetic fields generated by shear flows in two-dimensional resistive reconnection. *Physics Letters A*, 372:4614–4617, June 2008. doi: 10.1016/j.physleta.2008.04.048.
- J. Wang, C. Xiao, and X. Wang. Effects of out-of-plane shear flows on fast reconnection in a two-dimensional Hall magnetohydrodynamics model. *Physics of Plasmas*, 19(3):032905, March 2012. doi: 10.1063/1.3697561.
- H. Xie and Y. Lin. Two-dimensional hybrid simulation of the dayside reconnection layer and associated ion transport. *Journal of Geophysical Research*, 105:25171–25184, November 2000. doi: 10.1029/2000JA000143.
- S. Zenitani, M. Hesse, A. Klimas, C. Black, and M. Kuznetsova. The inner structure of collisionless magnetic reconnection: The electron-frame dissipation measure and Hall fields. *Physics of Plasmas*, 18(12):122108, December 2011. doi: 10.1063/1.3662430.